BAYESIAN PHYSICAL-STATISTICAL RETRIEVAL OF SWE AND SNOW DEPTH FROM X AND KU-BAND SAR - DEMONSTRATION USING AIRBORNE SNOWSAR IN SNOWEX'17

Siddharth Singh[1], Michael Durand,[2] Edward Kim[3], Ana P. Barros[1]

[1]Department of Civil and Environmental Engineering, University of Illinois at Urbana-Champaign, Urbana, Illinois, USA
[2]School of Earth Sciences, Ohio State University, Columbus, Ohio, USA
[3]NASA Goddard Space Flight Center, Greenbelt, Maryland, USA

Correspondence to: Ana P. Barros (barros@illinois.edu)

Abstract

A physical-statistical framework to estimate Snow Water Equivalent (SWE) and snow depth from SAR measurements is presented and applied to four SnowSAR flight-line data sets collected during the SnowEx'2017 field campaign in Grand Mesa, Colorado, USA. The physical (radar) model is used to describe the relationship between snowpack conditions and volume backscatter. The statistical model is a Bayesian inference model that seeks to estimate the joint probability distribution of volume backscatter measurements, snow density and snow depth, and physical model parameters. Prior distributions are derived from multilayer snow hydrology predictions driven by downscaled numerical weather prediction (NWP) forecasts. To reduce noise to signal ratio, SnowSAR measurements at 1 m resolution were upscaled by simple averaging to 30 and 90 m resolution. To reduce the number of physical parameters, the multilayer snowpack is transformed for Bayesian inference into an equivalent single- or two-layer snowpack with the same snow mass and volume backscatter. ~~–~~Successful retrievals meeting NASEM (2018) science requirements are defined by absolute convergence backscatter errors ≤ 1.2 dB and local SnowSAR incidence angles between 30º and 45º for X- and Ku-band VV-pol backscatter measurements and were achieved for 75% to 87% for all grassland pixels with SWE up to 0.7m and snow depth up to 2 m~~, defined by absolute convergence backscatter errors ≤ 1.2 dB and local SnowSAR incidence angles between 30º and 45º for X- and Ku-band VV-pol backscatter measurements, were achieved for 75% to 87% for all grassland pixels with SWE up to 0.7m and snow depth up to 2 m~~. SWE retrievals compare well with snow pit observations showing strong skill in deep snow with average absolute SWE residuals of 5-7% (15-18%) for the two-layer (single-layer) retrieval algorithm. Furthermore, the spatial distributions of snow depth retrievals vis-à-vis LIDAR estimates have Bhattacharya Coefficients above 94% (90%) for homogeneous grassland pixels at 30 m (90 m resolution), and values up to 76% in mixed forest and grassland areas indicating that the retrievals closely capture snowpack spatial variability. Because NWP forecasts are available everywhere, the proposed approach could be applied to SWE and snow depth retrievals from a dedicated global snow mission.

1. Introduction

The seasonal snowpack plays a critical role in climate and weather variability due to its role in the surface energy budget on account of its high albedo, and in the surface water budget as ~~providing~~ temporary storage of frozen precipitation in the cold season until it melts in the warm season and becomes available as runoff. The water stored in the snowpack is measured by the Snow Water Equivalent (SWE), the depth of liquid water per unit area that would be released if the snowpack were to melt completely. It is the product of the specific gravity of snow with respect to water (ρ_{snow}/ρ_{w}) and the depth of the snowpack (SD). To map SWE in the cold season is to map snow water resources. To map onset of melt and snow wetness is to map the timing and geography of snow water resources availability. Climate variability and change with increasing air temperature, shifts in atmospheric moisture convergence patterns, and increases in the frequency of extreme events is already causing significant changes in frequency and patterns and timing of seasonal snow accumulation and melt with severe implications for water and food security in addition to cascading economic and ecosystem impacts (Huang and Swain, 2022; Musselman et al., 2021; Sturm et al., 2010).

The need to capture snowpack heterogeneity and dynamics tied to weather, climate, landcover and landform variability remains a chief challenge to developing a snow observing system at the spatial and temporal scales required to answer water cycle science questions and for societal decision-making. The potential for systematic snowpack monitoring in remote regions has long been investigated, including the integration of remote sensing measurements and physical models (e.g. (Martinec et al. 1991; Mote et al. 2003; Bateni et al. 2015; Li et al. 2017; Kim et al. 2019; Cao and Barros, 2023a). Assimilation of radiance or backscatter is most powerful with a time series of observations. Time-series observations are available presently from tower measurements, albeit at the point scale of the tower footprint (see summary by Tsang et al. 2022), and do not capture the large joint spatial and temporal variability of snowpacks from local to regional scales depending on weather and climate, landform, land use and landcover. Frequent spatial observations are required for this purpose. Airborne observations can be used for mapping but typically occur once or twice during a winter season and over limited areas. A dedicated satellite mission is necessary to acquire time-series of measurements globally.

Presently, advances in radar technology and retrieval algorithms (Tsang et al., 2022), and especially the demonstrated capabilities of NewSpace satellite missions (Villano et al. 2020) make high spatial resolution of Synthetic Aperture Radar (SAR; 10's m) Earth observations from space feasible in contrast to the challenges faced in the past (Rott et al. 2012). During the SnowEx'17 field campaign (Kim et al., 2017), a comprehensive data set consisting of airborne dual-frequency SAR (X- and Ku-band Synthetic Aperture Radar) backscatter measurements using the SnowSAR instrument (Macedo et al. 2020), the Airborne Snow Observatory (ASO, Painter et al. 2018) and a plethora of high-quality ground-validation measurements of snowpack properties and ancillary data (Table 1) offer an unprecedented opportunity to investigate the full potential of SAR toward developing the next generation of retrieval algorithms.

Due to the highly nonlinear snow physics and the time-varying stratigraphy of snowpacks, radiance or backscatter measurements depend on the vertical structure of snowpack physical properties such as snow density, snow temperature, and snow grain size in addition to SWE and snow depth. Because the number of observations is smaller than the number of parameters required to solve the inverse-problem, retrieval of SWE and snow depth is an underdetermined estimation problem. This challenge can be addressed using a physical-statistical approach for retrieval. Physical-statistical approaches combine physical process models with a Bayesian statistical framework to inform how geophysical states and parameters relate to measurements by obeying fundamental physical constraints (Berliner, 2003; Lowman and Barros, 2014).~~. Thus, SWE and snow depth retrieval is an underdetermined problem. Physical-statistical approaches enable physically-based constraints to relate measurements to geophysical states and parameters and more directly solving Bayes' law (Berliner, 2003).~~ In this manuscript, we propose~~, implement, demonstrate~~, and evaluate a general physical-statistical framework to retrieve SWE from SnowSAR measurements across a heterogeneous landscape during SnowEx'17.

2. Previous Work

2.1 Forward Simulation - From SWE to Backscatter

The advantage of SAR technology is the high-spatial resolution of its measurements, which is necessary to capture the spatial heterogeneity ~~and temporal variability~~ of snowpack physical processes (e.g. Deems et al. 2016; Mendoza et al., 2020; Manickam and Barros, 2020) as demonstrated in forward simulations. Cao and Barros (2020, 2023a~~2~~; hereafter CB20 and CB23~~2~~) demonstrated the utility of a ~~coupled~~ multi-layer snow hydrology (MSHM) coupled with a radiative transfer model (RTM) forced by high-resolution operational numerical weather prediction (NWP) model forecasts to capture the seasonal hysteresis behavior of the seasonal snowpack at Grand Mesa and Senator Beck in Colorado against Sentinel-1 C-band measurements.

The MSHM is a physically driven snow hydrology model that simulates the evolution of snowpack physical properties including detailed stratigraphy (Kang and Barros, 2012a-b; CB20). During snowfall events, fresh snow is added to the top layer of the snowpack until a threshold accumulation is met, and a new layer forms. The RTM used here is MEMLS3a (Microwave Emission Model of Layered Snowpacks adapted to include backscattering by Proksch et al., 2015). MEMLS is a physically driven radiative transfer model which takes snowpack characteristics as inputs and simulates its microwave emission for a frequency band with four polarizations – HH, VV, HV and VH (originally proposed by Wiesmann and Mätzler, 1999). To estimate total scattering, ground backscatter σ_{bkg} must be modeled as well, as described below. .

Figure 1 illustrates the various backscatter mechanisms contributing to total backscatter (σ_{total}) in active microwave measurements represented in MEMLS3&a, the RTM: volume backscatter (σ_{vol}) from the multiple interactions of the incoming radar signal within the snowpack, the backscatter at the snowpack-air interface (σ_{surf}) and at the snowpack-ground interface including interactions with submerged vegetation and litter (σ_{bkg}). In forested areas, additional backscatter mechanisms are associated with the multiple bounce pathways among tree canopy, intercepted snow, tree trunks, and snowpack. Depending on viewing geometry (flight path and incidence angle), σ_{total} measurements from areas without trees in regions of mixed landcover can include significant contribution from trees along the grassland-forest transitions.

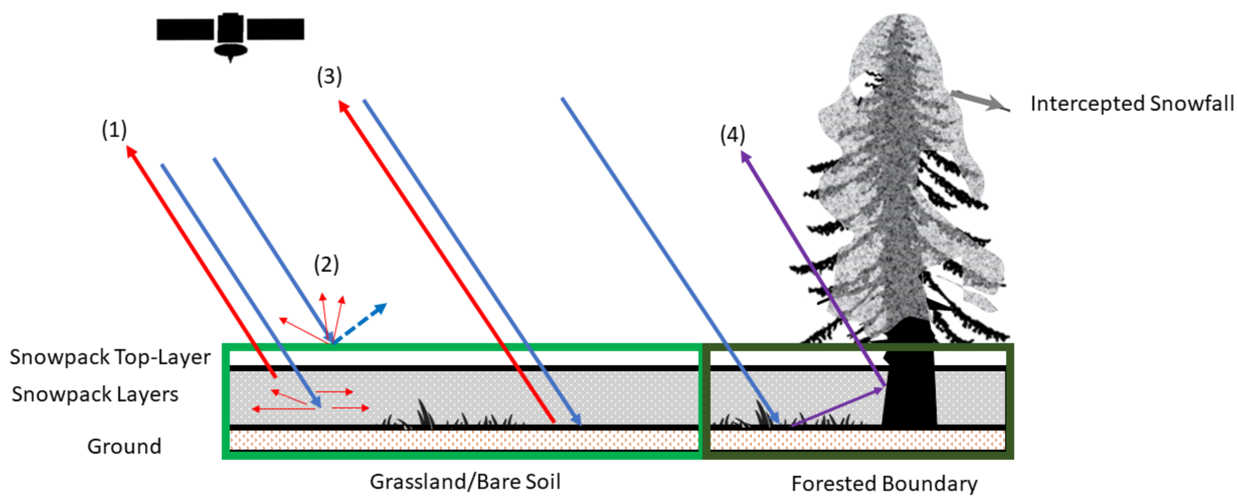

Figure 1: Scattering mechanisms for grassland submerged by snow and snowpack over bare soil or rock: (1) Volume Backscatter σ_{vol}; (2) surface backscatter σ_{surf}; (3) background backscatter at the snow-ground interface σ_{bkg}; (4) snowpack-ground-canopy-tree trunk interactions at forested boundaries. Red arrows (1), (2) and (3) are resolved in the retrieval applications demonstrated here.

CB23~~2~~ used the coupled MSHM-MEMLS in forward mode to predict Sentinel-1 C-band volume backscatter σ_{vol} without calibration or nudging of ground observations without bias and within ± 2.5 dB at 90 m resolution across terrain slopes in the [10°-52°] range for barren land, ~~and~~ alpine grass and shrubs and in forested areas with snow-free canopy at the beginning of spring in the Senator Beck Basin in Colorado. They estimated σ_{bkg} as the average of Sentinel-1 measurements for snow-free conditions. Cao and Barros (2023b) modified MEMLS3&a to include double-bounce effects among snowpack and vegetation (MEMLS-V) and retrieved σ_{bkg} from total backscatter σ_{total} measurements in mixed landcover using simulated annealing. Their estimates are consistent with CB23~~2~~, suggesting potential to simplify the inverse-problem of estimating snowpack physical properties from total backscatter measurements in mixed landcover and further simplify the physical-statistical retrieval framework proposed here, although further evaluation is necessary.

2.2 Physical-Statistical Retrieval

For retrieval in a Bayesian framework, the probability of the retrieved geophysical variable *x* (the inferred posterior distribution) is conditional on the *a priori* knowledge of the variable *x* (the prior distribution), indirect measurements D, and a physical model *M(η)* (e.g., the snow radiative transfer algorithm in this case) with physical parameters η (including *x*) and statistical error parameters ζ. The joint probability distribution of *M*, *D*~~*y*~~, *η*, and *ζ* can be written as:

$$P(M, D, \eta, \zeta) = P(D|M, \eta, \zeta) \times P(M|\eta, \zeta) \times P(\eta, \zeta) \quad (1)$$

The first term to the right-hand side of Eq. (1) is the backscatter data model, the second term is the prior of the backscatter, and the third term is the prior of the snowpack physical parameters (including snow depth and snow density, etc)~~-~~ with statistical error parameters. Assuming the measurements do not depend on the physical parameters, the model does not depend on the statistical error parameters, and that the physical parameters and the statistical parameters are independent, Eq. (1) can be revised to read

$$P(M, D, \eta, \zeta) = P(D|M, \eta) \times P(M|\eta) \times P(\eta) \times P(\zeta) \tag{2}$$

And finally in the context of specific measurements y with known uncertainty described by P(y)

$$P(M, \eta, \zeta |\, y) = P(y|M, \eta) \times P(M|\eta) \times \frac{P(\eta) \times P(\zeta)}{P(y)} \tag{3}$$

The physical model M and P(y) are invariant and assuming that we have a good understanding of the statistical errors, then Eq. (3) can be further simplified as follows

$$P(\eta|y) \propto P(y|\eta) \times P(\eta) \tag{4}$$

In the context of Bayesian inference the goal is to maximize P(η|y), the posterior probability of physical parameters conditional on measurements informed by the a priori parameter probabilities P(η). ~~-~~This implies maximizing the second term in Eq.(4), ~~To maximize P(y|η),~~ the posterior of the backscatter conditional on physical parameters η, implies minimizing the difference between measurements y with known error covariance matrix Σ_y and model predictions *M(η)*. For multiple concurrent measurements, $P(y|\eta)$ can be described by a multivariate normal distribution, ~~-For a multivariate normal distribution, Durand and Liu (2012) proposed~~

$$P(y|\eta) = (2\pi)^{\left(-\frac{N}{2}\right)} \mid \Sigma_y \mid^{-\frac{1}{2}} exp\left[-\frac{1}{2}(y - M(\eta))^T \Sigma_y^{-1}(y - M(\eta))\right] \tag{5}$$

where N is the number of measurements at a given location and time (e.g. backscatter at different frequencies as in Durand and Liu, (2012).

Pan et al. (2023, hereafter P23) adapted a Bayesian retrieval algorithm previously developed to estimate SWE from passive microwave measurements (Pan et al. 2017, hereafter P17) to active microwave, hereafter referred to as Base-AM. The snow radiative transfer algorithm in Base-AM is MEMLS, and the semi-empirical Dobson model is used to estimate the soil dielectric constant as a function of soil moisture and soil texture (Dobson et al. 1985; Hallikainen et al. 1985). A Monte Carlo Markov Chain (MCMC) iterative algorithm (Metropolis et al. 1953) is used to sample from P(η|y) starting from initial values and using the likelihood ratio criteria to achieve convergence. In this work, realistic snowpack predictions from MSHM-MEMLS are used to define the prior distributions of parameters and constrain the Bayesian retrievals: y represents the SnowSAR backscatter measurements and η represents to all model parameters and geophysical variables including SWE, SD, snow density.

~~where η are the snowpack and ground parameters whereas y are the backscatter observations .~~ ~~Here, the realistic snowpack predictions from MSHM-MEMLS are used to define the prior distributions of parameters and constrain the Bayesian retrievals.~~

3. Study Area and Data

3.1 Study Area and Ancillary Data

The study region is Grand Mesa, Colorado, a plateau that is 2,000 m above adjacent low-lying areas and is surrounded by ridges up to 500m in elevation (as depicted in Fig. 2). Grand Mesa has an alpine climate, experiencing snowfall throughout the year except during the months of July and August. Landcover is heterogeneous with grasslands in the west and a mix of evergreen and deciduous forest to the east. Numerous wetlands are widespread across the Mesa, especially in the transition from grassland to forest. The land cover data were obtained from the National Land Data Assimilation System (NLDAS)~~ and the National American Land Change Monitoring System (NALCMS), both at 30 m resolution~~. The datasets were upscaled to 90 m using nearest neighbor interpolation to support retrievals at 90 m resolution (see Section 4).~~The datasets were upscaled to 90m using nearest neighbor interpolation.~~ NLDAS is used to determine landcover type in the snow hydrology model. NALCMS is used to upscale the evaluation data. Hourly albedo is derived from NLDAS at 12.5 km resolution. A summary of all the datasets used in this study is available in Table 1.

Table 1: Summary list of datasets used in the study.

Data	Source	Spatial Resolution		Temporal Resolution		Date Range	Relevant Link
		Initial	Final	Initial	Final		
Rainfall Temperature Air Pressure Incoming SW radiation Incoming Longwave radiation Wind speed Humidity	HRRR	3 km	30 m, 90 m	1 hr	30 min	9/1/2016 - 2/25/2017	https://rapidrefresh.noaa.gov/hrrr/
Albedo	NLDAS	12.5 km	30 m	1 hr	30 min	9/1/2016- 2/25/2017	https://ldas.gsfc.nasa.gov/
Backscatter	SnowSAR – SnowEx'17	1 m	30 m, 90 m	-	-	2/21/2017	https://nsidc.org/data/snex17_snowsar/versions/1
Landcover	NLCD, NALCMS	30 m	30 m, 90 m	-	-	-	https://www.usgs.gov/centers/eros/science/national-land-cover-database http://www.cec.org/north-american-land-change-monitoring-system/
Snow Depth	LIDAR – SnowEx'17	3 m	30 m, 90 m	-	-	2/25/2017	https://nsidc.org/data/aso_3m_sd/versions/1

SWE	Snowpit – SnowEx’17	-	-	-	-	2/20/2017-2/24/2017	https://nsidc.org/data/snex17_snowpits/versions/1

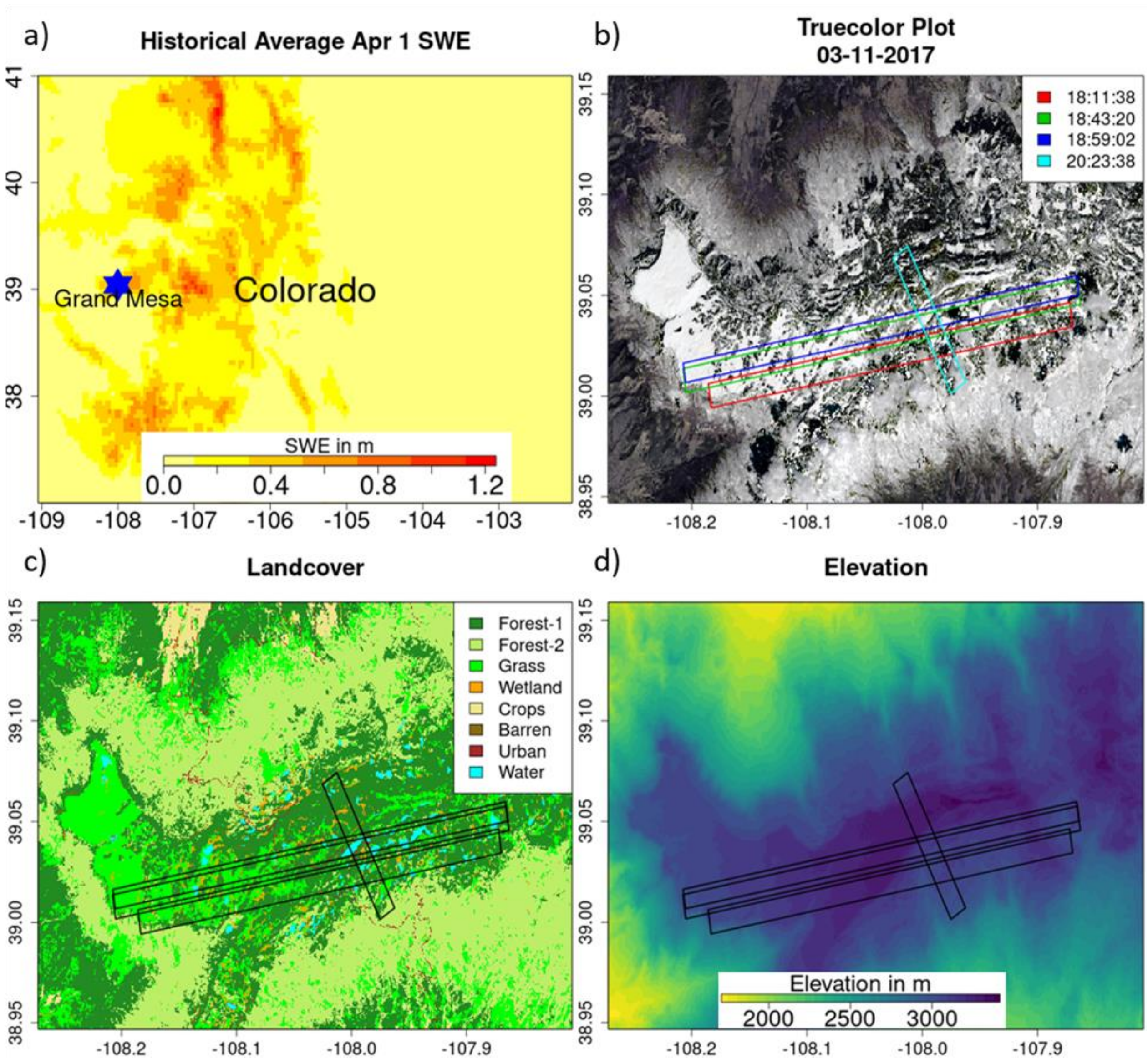

Figure 2: Study area in Grand Mesa, Colorado. a) Location of Grand Mesa in Colorado, with historical Apr 1 SWE average as base map. b) Paths of 4 SnowSAR SnowEx’17 flights on 21 Feb 2017, with true color image obtained from Landsat on 03/11/2017 as the base map. c) Land cover of the study region. Forest-1 are needle leaf forests; Forest-2 are broadleaf forests. d) Digital elevation map of the study region.

3.2 Atmospheric Forcing

Numerical Weather Prediction (NWP) outputs are used as the atmospheric forcing for the snow hydrology model and to set up boundary conditions. Previously, CB20 and CB23~~2~~ relied on HRRR

(High-Resolution Rapid Refresh) hourly forecasts at 3 km and downscaled it to 90 m in Grand Mesa. Here, the same data set was independently downscaled to 30 m as well. The HRRR dataset is produced by National Ocean and Atmospheric Agency (NOAA) by hourly assimilation of observations at 13 km resolution (Benjamin et al., 2016; Table 1). Hourly atmospheric forcing was linearly interpolated to 30 min temporal resolution used in the snow hydrology model.

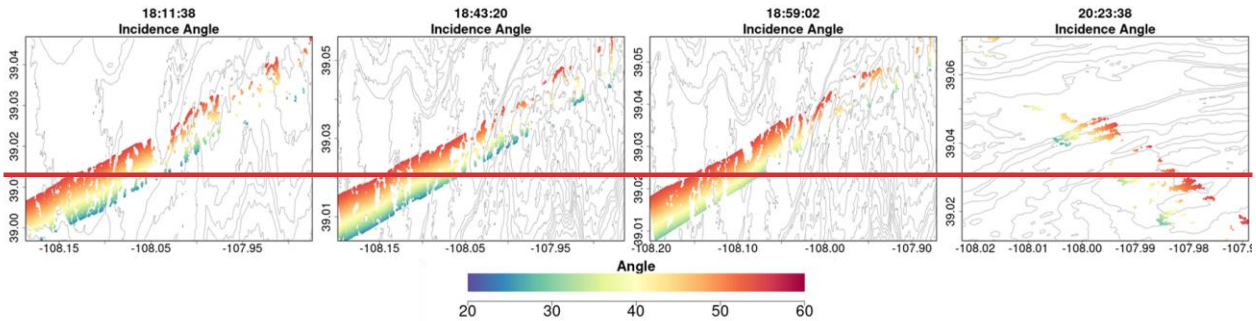

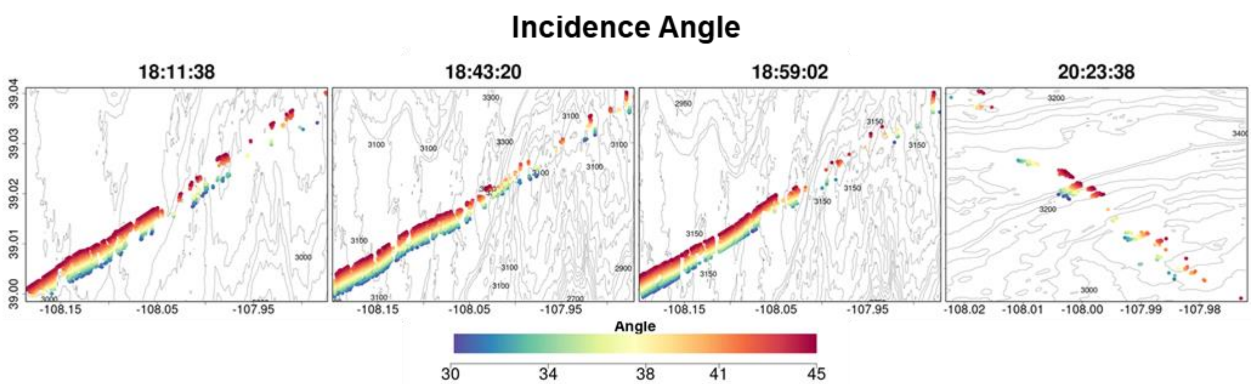

Figure 3: Maps of incidence angles along SnowSAR flight paths on February 21, 2017 during SnowEx'17.

3.34 SnowSAR Backscatter

During SnowEx'17, airborne microwave backscatter measurements were made in Grand Mesa on 21 Feb 2017 at 1 m resolution (Table 1). The SnowSAR instrument is a dual frequency (X and Ku Band) radar. A total of six flightlines were completed, two short ones on sloped densely forested terrain and four long lines on the plateau. Here, only the four flightlines on the plateau are used for analysis (Fig. 2 and Fig. 3). The flights are between 18:00 and 21:00 GMT (noon – 3PM MST). SnowSAR data quality control measures included filtering based on aircraft attitude (there were line segments with turbulence), beam incidence angle/antenna pattern, and signal-to-noise-ratio of the backscatter coefficients. Processing of the original airborne SAR measurements and quality control indicate that only the co-pol X-band HH- and VV-pol as well as Ku-band VV-pol measurements are adequate for retrieval. Geolocation was verified against corner reflector targets and geographic features and found to be very robust. The SnowSAR data were upscaled to 30 m and 90 m resolution by simple averaging of all SnowSAR measurements within each pixel.

3.4~~5~~ Validation Data

LIDAR Snow Depth – The Airborne Snow Observatory (ASO) LIDAR measurements of snow depth at 3m resolution across Grand Mesa are available for SnowEx'17 on February 25, thus 4 days after the SnowSAR flights (Painter et al., 2018; Table 1). There were no significant snow storms or strong winds in that period, except for about 3mm of rainfall for less than 1 hour on February 24~~th~~. These data are used to examine the distribution of retrieved snow depths, that is indicative of the spatial heterogeneity of the snowpack, and the relative absolute differences between LIDAR measurements and retrieval of snow depth, that are indicative of local retrieval errors. The LIDAR data were upscaled to 30 m and 90 m using simple averaging (e.g., Fig.4a). There can be large snow depth underestimation errors associated with upscaled LIDAR retrievals along the edges of forests where the snow depth is underestimated consistent with previous work (e.g. Deems et al. 2013; Jacobs et al. 2021). Given the expect measurement uncertainty on the order of 10-20 cm in Grand Mesa, which is amplified by microtopography, LIDAR pixels with snow depth shallower than 20 cm are not considered for evaluation.

Snowpit SWE - Multiple snowpits were excavated during the SnowEx'17 field campaign across Grand Mesa (Table 1). Due to the small number of snow pit measurements along the SnowSAR flightlines on 21 February, snowpit measurements on 20-24 of February were considered for evaluation assuming that in the absence of snowstorms or other weather events the snow pack does not change significantly during the 4-day period. Differences are expected at local places but the overall spatial trends should be maintained such as the west-east gradient in snow depth. The values of snowpit SWE are estimated using an average of the snow density measurements at different depths applied to the entire snow depth. Only pits in the non-forested areas were selected for evaluation (Fig. 4b).

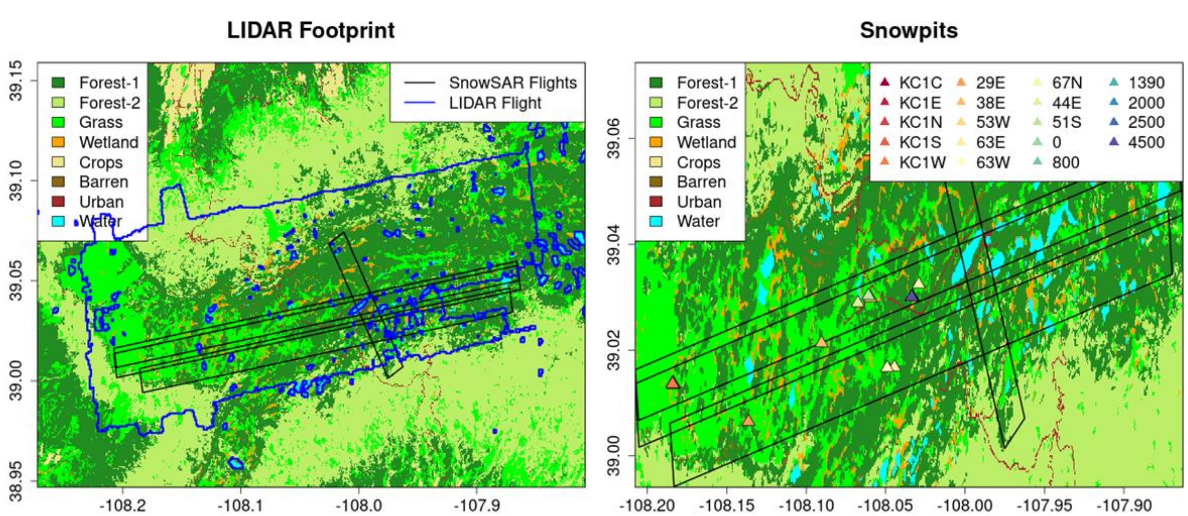

Figure 4: a) Flight footprint of the LIDAR instrument used to measure the snow depth during SnowEx'17. b) Location of snow pits used to measure SWE 20-24 Feb 2017. The legend identifies SnowEx'17 Pit IDs.

~~4. Methods~~

4.~~1~~ Retrieval Algorithm

Simplicity and computational efficiency are desirable attributes for an operational algorithm that produces successful retrievals, here understood as meeting science uncertainty requirements and latency adequate to meet applications needs defined by NASEM (2018). The retrieval methodology builds on existing and well evaluated snow hydrology, radiative transfer, and physical-statistical models (CB20,CB23, P17, P23) previously reviewed in Section 2. A list of forcings and coupling variables and parameters among MSHM, MEMLS and Base-AM is provided in Table 2.

Averaging is necessary to reduce the signal to noise ratio (SNR) in SnowSAR measurements at their native resolution (Section 3.3). Because the highest spatial resolution of available ancillary data sets is 30 m, the SnowSAR measurements were upscaled to 30 m to eliminate the need for interpolation and, or downscaling that introduce further uncertainty. Following results by Manickam and Barros (2020), the algorithm was also applied at 90 m resolution consistent with the first scaling break identified in Sentinel-1 SAR backscatter. The implication of linear scaling behavior is that successful retrievals at 90 m resolution can subsequently be statistically downscaled with confidence, which has significant computational advantages. Further upscaling was not conducted because the number of pixels becomes very small given the available coverage of SnowSAR flights.

~~The retrieval methodology builds on existing and well evaluated snow hydrology, radiative transfer, and physical-statistical models (CB20,CB22, P17, P23) previously reviewed in Section 2. Figure 6~~5 ~~illustrates the retrieval workflow consisting of four main steps: **(1a)** Snow hydrology simulation using MSHM to produce a layered snowpack; **(1b)** Volume backscatter σ_{vol} simulation using MEMLS and estimation of background backscatter σ_{bkg} by substration from SnowSAR σ_{total} measurements; **(2)** Determination of snowpack parameter prior distributions for retrieval: averaged snowpack physical property distributions for a 1 or 2 layer equivalent snowpack (1|2) with the same mass and total backscatter σ_{total}; **(3)** Determination of ground priors for retrieval: Bayesian estimation of ground parameters that govern the σ_{bkg} using MEMLS for a very thin (1 mm SD) film of snow on the ground; and **(4)** Retrieval: Bayesian optimization of simulated σ_{total} to derive posterior distributions of SD and ρ_{snow} for the 1|2 equivalent snowpack, and subsequent calculation of SWE.~~

Table 2: Input and output parameters from the three models in the SWE physical-statistical retrieval framework.

Model	**Input**	**Output**	**Reference**
MSHM	Rainfall Temperature Air Pressure Incoming shortwave radiation	Snow Temperature Profile Soil Temperature Profile Snow Density Profile	Cao and Barros (2020)

	Incoming longwave radiation Wind speed Humidity Albedo	Snow Depth Layering Profile Liquid Water Content Profile Snow Correlation Length Profile	
MEMLS	Snow Temperature Profile Soil Temperature Profile Snow Density Profile Snow Depth Layering Profile Snow Correlation Length Profile Cross polarization fraction Ground rms height	Diffused Reflectivity Profile Specular Reflectivity Profile Total Backscatter Coefficient	Proksch et al. (2015)
Base-AM	Equivalent Snow Temperature Prior Equivalent Soil Temperature Prior Equivalent Snow Density Prior Equivalent Snow Depth Prior Correlation Length Cross polarization fraction Ground rms height Total Backscatter Coefficient Prior	Optimized – Snow Layer Depth Snow Density	Pan et al., (2023)

Figure 5 illustrates the retrieval workflow consisting of four main steps. **Step 1 -** Snow hydrology simulation using MSHM to produce a layered snowpack and volume backscatter simulation using MEMLS (σ_{vol}^{sim}). **Step 2 -** Bayesian estimation of ground parameter priors that govern background backscatter σ_{bkg} using MEMLS assuming a very thin film of snow on the ground (1 mm SD) at the beginning of the accumulation season and estimation of the σ_{bkg} by subtraction of σ_{vol}^{sim} from SnowSAR total backscatter measurements σ_{SAR}^{tot}. **Step 3 -** Determination of snowpack priors for Bayesian SWE retrieval using results Step 1 and Step 2. **Step 4 -** Bayesian optimization of simulated σ_{SAR}^{tot} to derive posterior distributions of SD and ρ_{snow} for the single- and two-layer (1|2) equivalent snowpack, and subsequent calculation of retrieved SWE posperior distributions

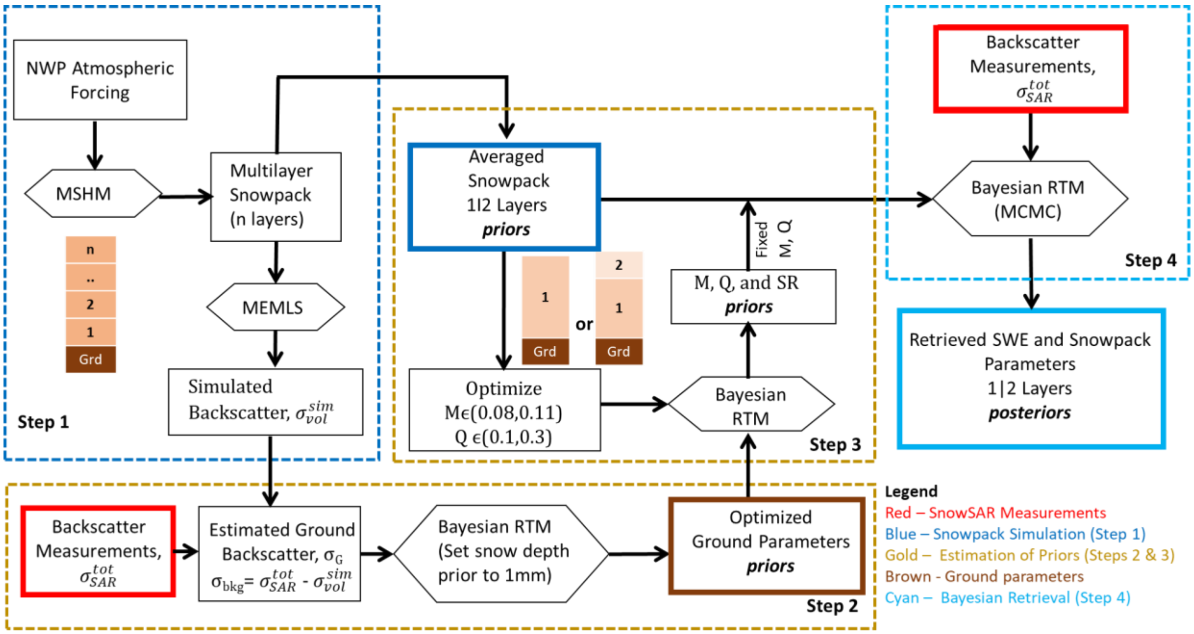

Figure 5: Workflow of the SWE Physical-Statistical retrieval framework. NWP atmospheric forcings drive MSHM to determine priors for the Bayesian radiative transfer model (Base-AM) and synthetic backscatter for ground parameters. SnowSAR backscatter measurements are assimilated to determine the posterior distribution of the snowpack parameters.

4.1 Layered Snowpack Simulations (Step 1)

Following the methodology presented in Section 2.1, MSHM was run for a full-year starting from snow free conditions on September 1st 2016 using downscaled HRRR data as atmospheric forcing (Section 3.2) and a timestep of 30 mins. On the day of the SnowSAR flights, the snowpack physical properties predicted at times corresponding to each of the four flights are used to derive the 1|2 Layer equivalent snowpack properties used in the retrieval. The simulated volume backscatter (σ_{vol}^{sim}) was estimated by specifying the cross polarization fraction parameter Q=0.2 following CB20. This is an empirical coefficient that distributes the diffuse scatering into cross and like polarization components in MEMLS (Proksch et al. 2014).

In realistic layered snowpacks, stratigraphy (i.e., vertical heterogeneity) is a dominant feature of the density, temperature, microstructure, and dielectric properties (e.g., emissivity and reflectivity). The vertical structure of snow microstructure in MSHM is described using a parameterization of snow correlation length (l_{ex}) consistent with MEMLS formulation. Depending on the number of layers, this poses an undetermined problem as the number of measurements is equal to the number of frequencies and the number of polarizations available (typically two or three). For example, there are only four observations for a dual-frequency measurement with dual polarization. In contrast, the set of independent parameters per layer includes snow density, layer thickness, liquid water content, snow grain size or correlation length, temperature, reflectivity, and transmissivity.

While converting the multi-layer snowpack to a single-layer model is the simpler path to address the undetermined inverse-propblem, fresh snowfall accumulation and snowpack crusting artifacts due to melt-refreeze cycles, as well as hardening by wind action introduce strong density and grain size differences at the top of the snowpack. To capture this behavior, we implement and evaluate the retrieval algorithm for both single and two-layer equivalent snowpacks derived from the layered snowpack simulated by MSHM. The equivalent single- or two-layered snowpack parameters for each pixel are obtained by matching SWE, snow depth (SD) and volume backscatter (σ_{vol}^{sim}) of the simulated multilayer snowpack.

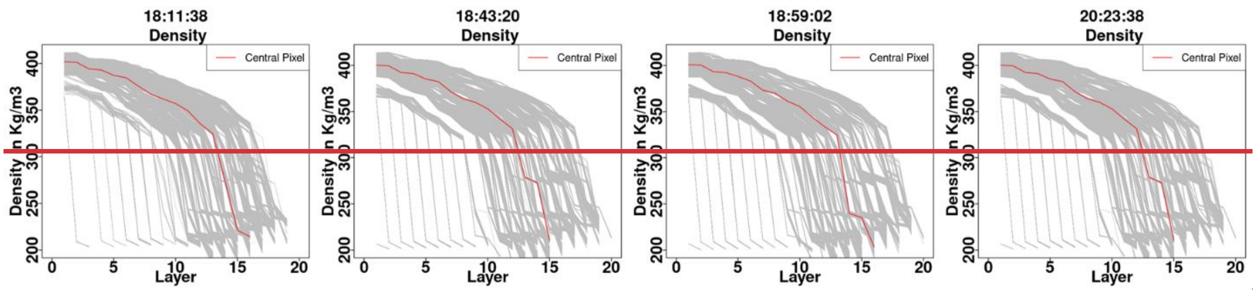

~~**Figure 5** - Density profiles obtained from MSHM for the 4 SnowSAR flight paths. The density profile of the central pixel for each of the flights is marked in red. Note the significant difference between the top 2-3 layers and the deeper snowpack supporting the two-layer snowpack concept.~~

4.2 Ground and Snowpack Parameter Priors (Steps 2 and 3)

~~4.1.1 Layered Snowpack Simulations and Prior Distributions (1a,2)~~

A first estimate of the σ_{bkg} is obtained by subtracting σ_{vol}^{sim} from SnowSAR X-band HH-pol σ_{SAR}^{tot} measurements following Baghdadi et al. (2011) who found better performance among backscattering models for HH-pol against TerraSAR-X measurements. In Base-AM, σ_{bkg} depends on the effective effective soil moisture and soil surface roughness. To optimize these parameters, σ_{bkg} is used as an "observed" value. To simulate snow-free conditions the snow depth is constrained to a maximum value of 1 mm in Step 2. The cross polarization fraction Q initially specified as Q=0.2 is optimized first and separately from other ground parameters in the third step of the retrieval algorithm (Fig. 5). The posterior distributions of the ground parameters in Step 2 are used along with the 1|2 layer prior distributions and the SnowSAR measurements to estimate the posterior distributions of snow depth and snow density using the Base-AM framework (Fig. 5) and both X- and Ku-band VVpol. SWE is subsequently derived from snow depth and snow density.

Single-layer Snowpack - The total snow depth and the averages of multilayered snowpack parameters are specified as the mean of the prior distribution for retrieval. Table 3 shows the range and standard deviation of the parameters.

Table 3: Base-AM model input variance and range for the parameters prepared using MSHM multilayer snowpack parameters. Alphanumerical subscript in 2-layer snowpack retrievals denotes layer number: 1- bottom layer; 2- top layer; avg- the average of all MSHM multilayer parameter values in the corresponding single or 2-layer snowpack. DZ is the MSHM snow depth.

Snow Parameters	**1 Layer Snowpack**			**2 Layer Snowpack**			
	Variance, σ^2	**Range**		**Variance, σ^2**		**Range for each layer**	
		Min	**Max**	**Bottom**	**Top**	**Min**	**Max**
Snow Temp., Ts [^{O}C]	$0.3\times Ts_{avg}$	$1.3\times Ts_{min}$	$0.7\times Ts_{max}$	$0.3\times Ts_{1,avg}$	$0.3\times Ts_{2,avg}$	$1.3\times Ts_{min}$	$0.7\times Ts_{max}$
Snow Density, ρ [Kg/m^3]	$0.3\times\rho_{avg}$	$0.8\times\rho_{min}$	$1.2\times\rho_{max}$	$0.3\times\rho_{1,avg}$	$0.3\times\rho_{2,avg}$	$0.8\times\rho_{min}$	$1.2\times\rho_{max}$
Snow Depth, DZ [m]	$0.3\times DZ$	$0.5\times DZ$	$1.5\times DZ$	$0.1\times DZ_1$	$0.2\times DZ_2$	$0.2\times DZ$	$0.9\times DZ$
Correlation Length, l_{ex}	$0.3\times l_{ex,avg}$	$l_{ex,min}$	$l_{ex,max}$	$0.2\times l_{ex,1,avg}$	$0.2\times l_{ex,2,avg}$	$l_{ex,min}$	$l_{ex,max}$
Soil Temp., Tsoil [^{O}C]	0.3	1.3		0.3		1.3	

~~MSHM was run for a full year starting from snow free conditions on September 1st 2016 using downscaled HRRR data as atmospheric forcing (Section 1.2) and a timestep of 30 mins. On the day of the SnowSAR flights, the snowpack physical properties predicted at times corresponding to each of the four flights are used to derive the 1|2 Layer equivalent snowpack properties used in the retrieval. Volume backscatter was estimated using the cross polarization fraction Q=0.2. The prior distributions for Base-AM are shown in Table 3.~~

Two-layer Snowpack – The average values of the snowpack physical properties for each layer are derived from the multilayer snowpack simulated by MSHM. The key requirement is to determine the depth of each one of the layers that best captures the snowpack vertical structure. Figure 6 shows MSHM simulated snowpack density profiles for each of the four SnowSAR flights. The shape of the profiles reflects the interplay between thermodynamic processes that change snow microstructure and dominate in the upper snowpack and mechanical consolidation processes that are dominant in the mid and lower layers. The snow depth point corresponding to the maximum change in snow density between adjacent layers in the multilayer snowpack is used here to divide the snowpack in two layers. Subsequently, the layer-depth weighted average density, snow temperature, and correlation length of the MSHM multilayer snowpack is calculated for the corresponding depths of the two-layer equivalent snowpack (Table 3).

~~In realistic layered snowpacks, stratigraphy (i.e., vertical heterogeneity) is a dominant feature of the density, temperature, microstructuremicrophysics, and dielectric properties (e.g., emissivity and reflectivity). The vertical structure of snow microphysics in MSHM is described using a parameterization of snow correlation length consistent with MEMLS formulation. Depending on the number of layers, this poses an overdetermined problem as the number of measurements is equal to the number of frequencies and the number of polarizations available (typically two or three). For example, there are only four observations for a dual-frequency measurement with dual polarization. In contrast, the set of independent parameters per layer includes snow density, layer thickness, liquid water content, snow grain size or correlation length, temperature, reflectivity, and transmissivity. To reduce the number of~~

~~independent parameters that need to be estimated, the multilayer snowpack is transformed into an equivalent single- or two-layered snowpack with the same SWE, snow depth (SD) and total backscatter σ_{total}.~~

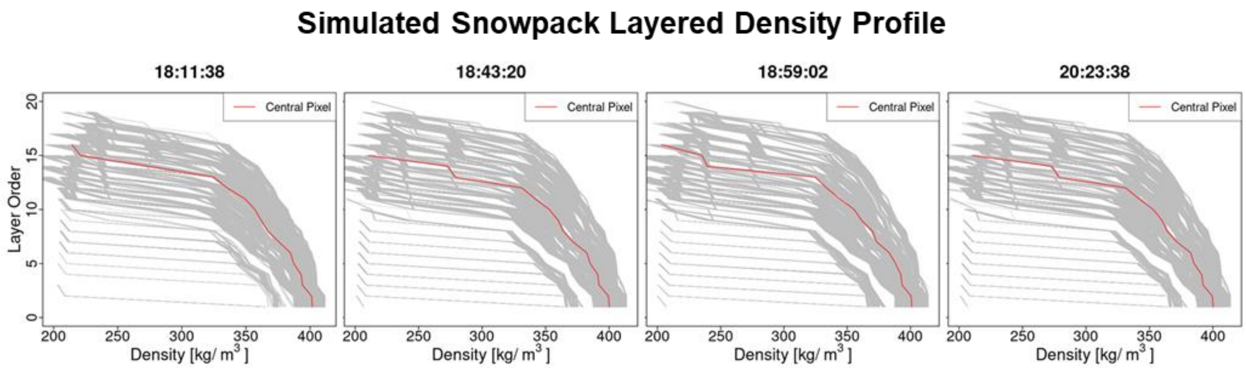

<u>**Figure 6** - Density profiles simulated by MSHM for all grassland pixels at 30 m resolution from the 4 SnowSAR flight paths. The density profile of the central pixel for each of the flights is marked in red. The snowpack layers are numbered from bottom to top tracking the evolution of simulated snowpack stratigraphy during the accumulation season. Note the significant difference between the top 2-3 layers and the deeper snowpack supporting the two-layer snowpack conceptual retrieval model.</u>

~~**Table 2:** Input and output parameters from the three models in the SWE physical-statistical retrieval framework.~~

~~**Model**~~	~~**Input**~~	~~**Output**~~	~~**Reference**~~
~~MSHM~~	~~Rainfall~~ ~~Temperature~~ ~~Air Pressure~~ ~~Incoming shortwave radiation~~ ~~Incoming longwave radiation~~ ~~Wind speed~~ ~~Humidity~~ ~~Albedo~~	~~Snow Temperature Profile~~ ~~Soil Temperature Profile~~ ~~Snow Density Profile~~ ~~Snow Depth Layering Profile~~ ~~Liquid Water Content Profile~~ ~~Snow Correlation Length Profile~~	~~Cao and Barros (2020)~~
~~MEMLS~~	~~Snow Temperature Profile~~ ~~Soil Temperature Profile~~ ~~Snow Density Profile~~ ~~Snow Depth Layering Profile~~ ~~Snow Correlation Length Profile~~ ~~Cross polarization fraction~~ ~~Ground rms height~~	~~Diffused Reflectivity Profile~~ ~~Specular Reflectivity Profile~~ ~~Total Backscatter Coefficient~~	~~Proksch et al. (2015)~~
~~Base AM~~	~~Equivalent Snow Temperature Prior~~ ~~Equivalent Soil Temperature Prior~~ ~~Equivalent Snow Density Prior~~	~~Optimized Snow Layer Depth~~ ~~Snow Density~~	~~Pan et al., 2023~~

	~~Equivalent Snow Depth Prior~~ ~~Correlation Length~~ ~~Cross polarization fraction~~ ~~Ground rms height~~ ~~Total Backscatter Coefficient Prior~~		

4.3 Bayesian Optimization (Step 4)

Realistic snowpack predictions from MSHM driven by weather forecasts (Step 1) are used to define the prior distributions of snowpack parameters and constrain Base-AM (Steps 2 and 3) to infer the posterior distribution of snowpack parameters given the SnowSAR backscatter measurements (Step 4) as discussed in Section 2.2.

The local mean of the posterior distribution for each parameter is hereafter referred to as the retrieval result for each pixel. SD retrievals are evaluated against LIDAR snow depth including spatial patterns and gradients, and overall statistical structure using histograms. SWE retrievals derived from the posterior distributions of snow density and snow depth are evaluated against SWE measurements at snowpits (Section 3.4). Original LIDAR measurements were reprojected and coregistered with the SnowSAR retrievals. A comparative analysis was conducted to examine the dependence of retrievals on incidence angle and the subgrid scale variability was quantified in terms of the standard deviation of original LIDAR measurements within the upscaled pixel. The amplitude error metrics are the mean, standard deviation, and mean absolute relative error (MARE):

~~**Table 3:** Base-AM model input standard deviation~~variance~~and range for the lognormal parameters prepared using MSHM multilayer snowpack parameters. Alphanumerical subscript in 2-layer snowpack retrievals denotes layer number: 1- bottom layer; 2- top layer; avg- the average of all MSHM multilayer parameter values in the corresponding single or 2-layer snowpack. DZ is the MSHM snow depth.~~

~~*Single-layer Snowpack* – The total snow depth and the averages of multilayered snowpack parameters are specified as the mean of the prior distribution for retrieval. Table 3 shows the range and standard deviation~~variance ~~of the parameters~~ for ~~.~~

~~*Two-layer Snowpack* – The average values of the snowpack physical properties for each of two layers are derived from the multilayer snowpack simulated by MSHM as for the single-layer case. The key requirement is to determine the depth of each one of the layers that best captures the snowpack vertical structure. Figure 5 shows examples of MSHM snow density profiles for each of the four SnowSAR flights. Note the large changes with depth of the snow density profiles. The shape of the profiles reflects the interplay between thermodynamic processes that change snow microstructure and dominate in the upper snowpack and mechanical consolidation processes that are dominant in the mid and lower layers. The snow depth point corresponding to the maximum change in snow density between adjacent layers in the multilayer snowpack is used here to divide the snowpack in two layers. Subsequently, the average density, snow temperature, and correlation~~

~~length of the MSHM multilayer snowpack is calculated for the corresponding depths of the two-layer equivalent snowpack (Table 3).~~

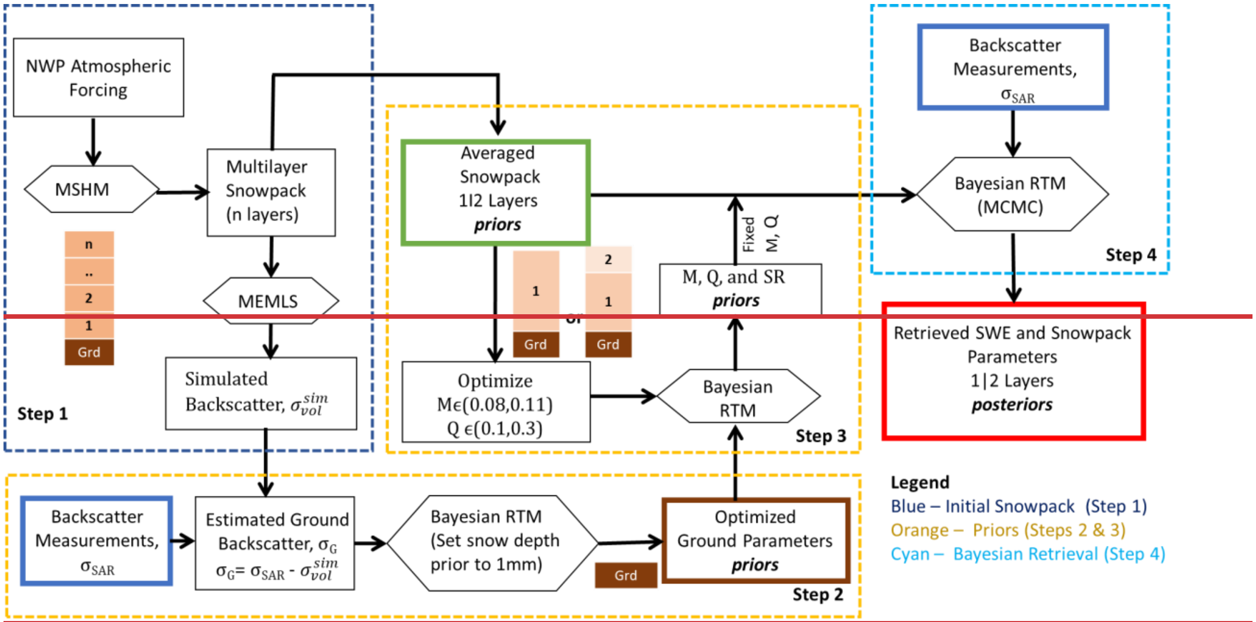

~~**Figure 6:** Workflow of the SWE Physical-Statistical retrieval. NWP atmospheric forcings are used to set up MSHM to determine priors for the Bayesian radiative transfer model (Base-AM) and synthetic backscatter for ground parameters. SnowSAR backscatter measurements are assimilated to determine the posterior distribution of the snowpack parameters.~~

~~4.1.2 Determination of Ground and Snowpack Microstructure Parameters (1b, 3)~~

~~A first estimate of the σ_{bkg} is obtained by subtracting σ_{vol} from SnowSAR X-band HH- pol σ_{total} measurements. (Baghdadi et al., 2011) estimated the compared the modelling of X band backscatter at different polarizations for rough bare soils and found HH polarizations had lower RMSE compared to other polarizations. Additoinally, the σ_{bkg} obtained using using Ku band backscatter observation from SnowSAR had a lot of negative values, and were not useful in the further simulation. In Base-AM, σ_{bkg} depends on the effective effective soil moisture and soil surface roughness. To optimize these parameters, σ_{bkg} is used as an "observed" value. To simulate snow-free conditions the snow depth is constrained to a maximum value of 1 mm. The cross polarization fraction Q initially specified as Q=0.2 is optimized first and separately from other ground parameters in the third step of the retrieval algorithm (Fig. 6). Finally, the posterior distributions of the ground parameters are used along with the 1|2 layer prior distributions and the SnowSAR measurements to estimate the posterior distributions of snow depth and snow density using the Base-AM framework (Fig. 6) and both X- and Ku-band VVpol. SWE is subsequently derived from snow depth and snow density.~~

~~**4.2 Retrieval Evaluation**~~

~~The local mean of the posterior distribution for each parameter is hereafter referred to as the retrieval result for each pixel. The retrievals are evaluated against LIDAR snow depth including spatial patterns and gradients, and overall statistical structure using histograms. SWE retrievals derived from the posterior distributions of snow density and snow depth are evaluated against SWE measurements at snowpits (Section 3). Original LIDAR measurements were reprojected and coregistered with the SnowSAR retrievals. A comparative analysis retrievals was conducted to examine the dependence of retrievals on incidence angle for different levels and the subgrid scale variability quantified as the standard deviation of original LIDAR measurements within the upscaled pixel. The amplitude error metrics are the mean, standard deviation, and mean absolute relative error (MARE):~~

$$MARE = \frac{\sum_{i=1}^{n} |\, 1 - R_i/O_i |}{N} \tag{6}$$

where O are observations and R are retrievals. The Bhattacharya coefficient (BC) is used to compare the spatial distributions of snow depth and backscatter. BC measures the similarity between two probability distributions p_1 and p_2 as follows (Bhattacharya, 1943)

$$BC = \sum_{i=1}^{N} \sqrt{p_1(i) p_2(i)} \tag{7}$$

Finally, among the 39 snowpits available for evaluation on February 21, only 15 pits in open areas (i.e. grasslands) were retained for evaluation and snow pits without SnowSAR measurements within a radius of 100 m were discarded.

5. Results and Discussion

5.1. Successful Retrievals

SnowSAR measurements are strongly affected by aircraft operations, viewing geometry that varies systematically along the flight path resulting in amplitude artifacts amplified by landform and landcover heterogeneity. Even after separating homogeneous grassland pixels, there is contamination from multiple bounce artifacts at grassland-forest transitions and adjacent wetlands that cannot be resolved at 30 or 9~~6~~0 m resolution. Other errors embedded in the retrieval are associated with downscaling of HRRR forcings that produce biased snow priors, snow hydrology model structure~~assumptions~~, and errors tied to the background backscatter estimation. ~~-~~Combined these errors compounded can lead to a weak convergence of the Bayesian optimization algorithm resulting in large backscatter residuals.~~-~~ ~~-~~To account for these errors and meet NASEM (2018) science requirements, SnowSAR pixels for which the relative residual backscatter (RRB) between Base-AM simulated σ_{sim}^{tot} ~~σ_{total}~~ and SnowSAR measurements σ_{SAR}^{tot} was greater than 30% were identified as unsuccessful. In an operational context, these pixels would be flagged and identified as failed or highly uncertain retrievals. The successful retrieval fraction after restricting the range of incidence angles and imposing the RRB < 30% criterion is summarized in Table 4 for the four flights, and for both 1|2 layer snowpack retrievals at 30 and 90 m resolution. Except for the later flight path over the predominantly forested areas in the eastern sector of Grand Mesa (Fig.1), the fraction of successful retrievals by restricting the incidence angle and RRB varies between 75 and 87% across the four SnowSAR flights with a maximum absolute bias of 1.2 dB. Only figures with retrieval results at 30 m resolution are shown in the main text; retrieval results at 90 m resolution as well as other supporting analysis can be found in Appendix A.

Table 4: Spatial bias between SnowSAR backscatter and converged backscatter from Base-AM for successful retrievals for grassland pixels at 30 and 90 m spatial resolution over each flight. Successful retrievals are for pixels with local incidence angles in the 30°-45° range and relative residual backscatter (RRB) of less than 30% for each of the four flights. ~~Shaded columns are for retrievals at 90 m resolution.~~

Flight Time	Successful Retrieval Fraction				Bias (Observed - Converged) [dB]							
	1 Layer		2 Layer		1 Layer				2 Layer			
	30 m	90 m	30 m	90 m	30 m		90 m		30 m		90 m	
					X	Ku	X	Ku	X	Ku	X	Ku
18:11:38	0.86	0.87	0.85	0.86	0.92	-0.45	0.96	-0.48	0.94	-0.46	0.97	-0.50
18:43:20	0.75	0.75	0.75	0.75	1.08	-0.54	0.98	-0.36	1.07	-0.46	0.98	-0.37
18:59:02	0.78	0.81	0.81	0.81	1.20	-0.78	1.21	-0.79	1.15	-0.73	1.22	-0.83
20:23:38	0.66	0.69	0.57	0.69	0.51	-0.58	0.70	-0.43	0.62	-0.85	0.72	-0.45

5.2. Retrieval Skill

Figure 7 compares LIDAR snow depth (Fig. 7a) against colocated SnowSAR retrievals at 30 m for the SNOWSAR flight at 18:11:38 GMT(GMT=MST+6). The SnowSAR retrievals for high incidence angles underestimate the LIDAR snow depth (orange and red points). Lemmetyinen et al. (2022) suggested a nominal incidence angle of 35°-45° for retrievals ensuring proper focusing and calibration of SnowSAR swaths. CB23~~2~~ showed good skill in forward backscatter simulations for incidence angles as low as 30°. Overall the retrievals here also show very good performance for incidence angles between 30°-45°. Note however the large residuals for SnowSAR retrievals with high incidence angles (red and orange points in Fig. 7b) corresponding to LIDAR pixels with shallow snow depth (below the 1:1 line) and large subgrid-scale variability (orange and red points, Fig. 7c). Analysis for all flights at both 30 and 90 m resolution can be found in Appendix A (please see Figs. A1 and A2 similar to Fig. 7b; and Figs. A3 and A4 similar to Fig. 7c). Figures 7d, 7e, and 7f show the landcover, spatial distribution of subgrid standard deviation (SSTD) and absolute residual (Retrieved – LIDAR) snow depth for the same flight. Along the edges of forest, the SSTD ~~standard deviation~~ in the upscaled pixels is large due to high heterogeneity that cannot be resolved by the the LIDAR fusion algorithm for snow depth retrieval (Painter et al. 2016). The red box identifies an area with complex grassland-forest boundaries (Fig. 7d) and high subgrid scale variability (Fig. 7e) resulting in poor LIDAR estimates. The edge of wetlands also has comparatively higher residuals than completely homogeneous grasslands. This corresponds to the

LIDAR pixels with ~~standard deviation~~SSTD > ~~of more than~~ 0.3 m (yellow, orange and red in Fig. 7c). Therefore, only LIDAR pixels with SSTD ~~subgrid-scale standard deviations~~ ≤ 0.3m are used for assessment of retrievals.

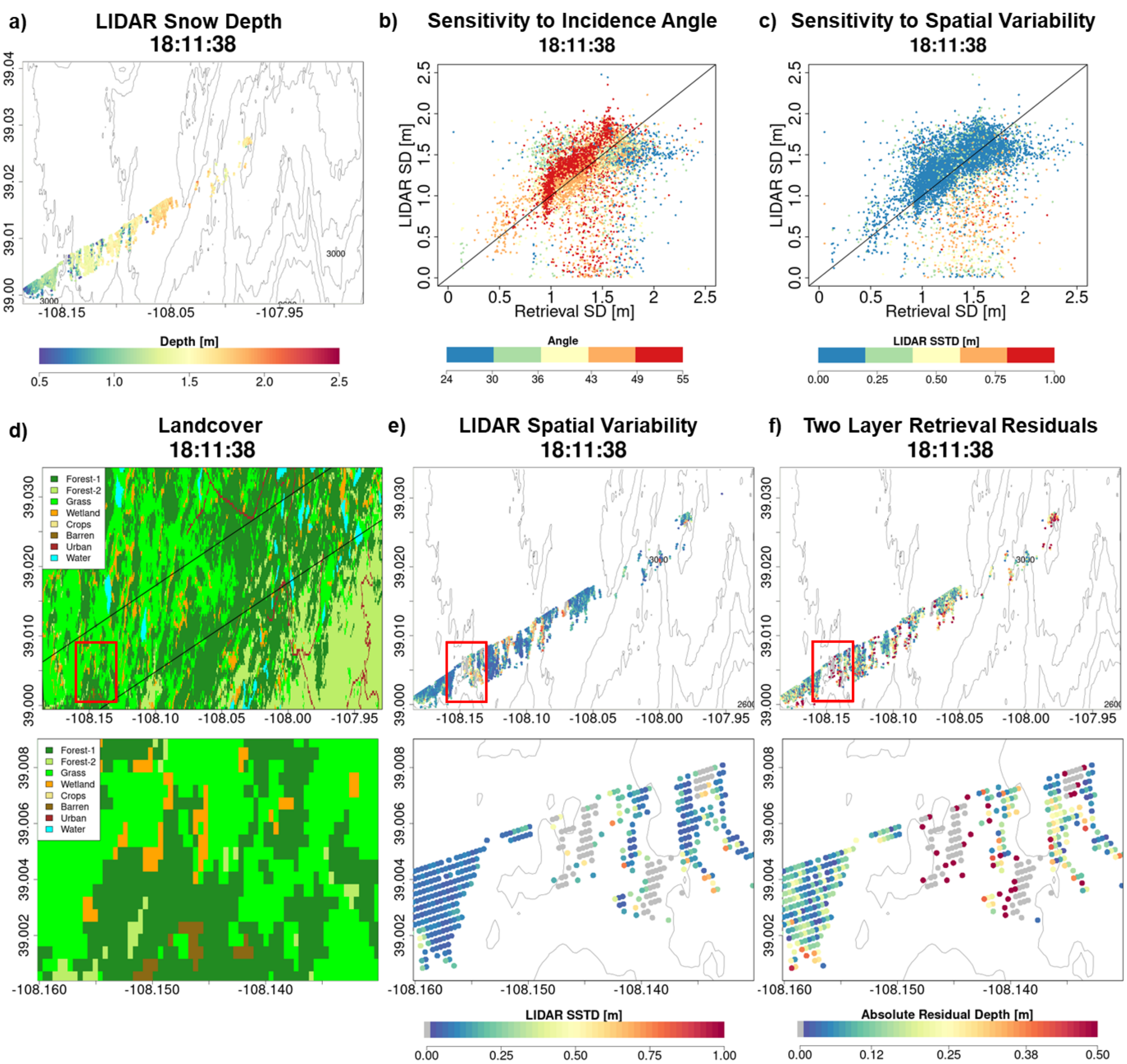

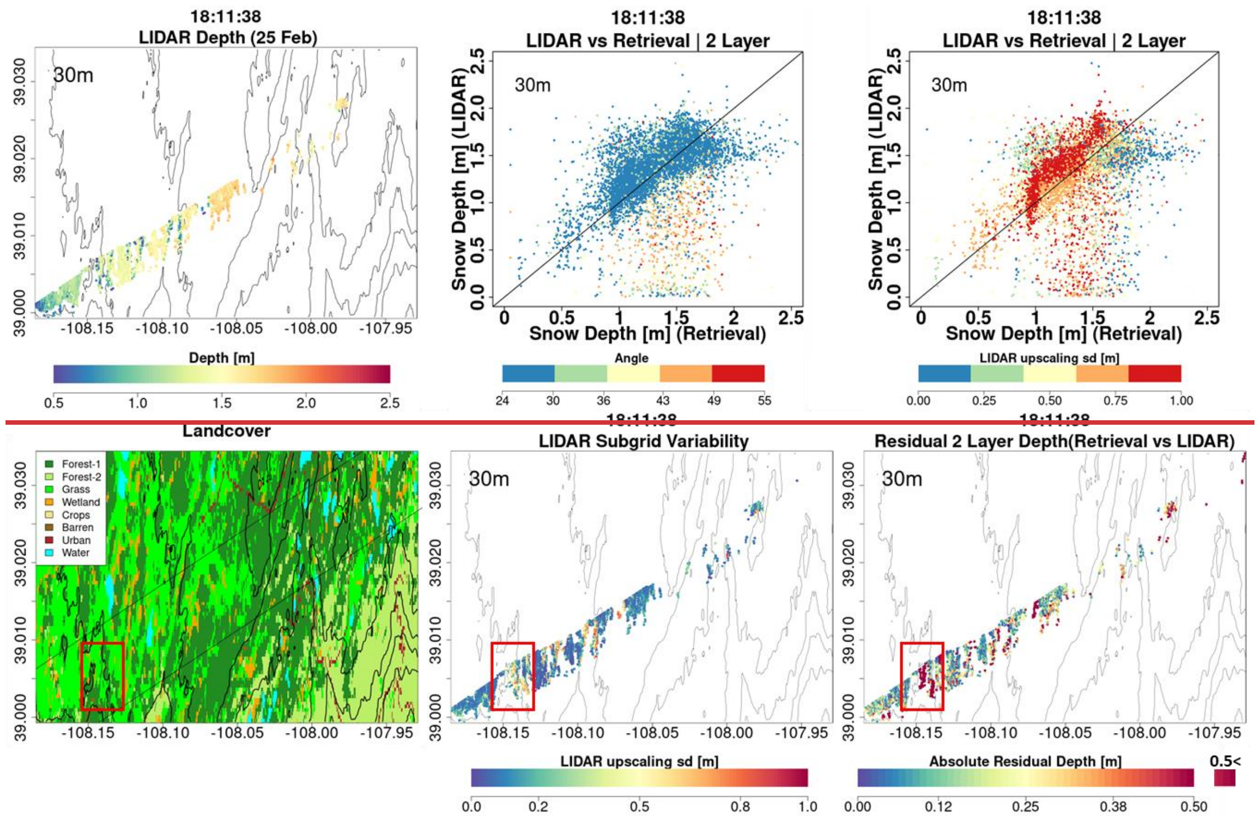

Figure 7: Snow depth measurements using airborne LIDAR on 2/25/17, 4 days after the SnowSAR flights. b) Comparison between LIDAR snow depth and the 2-layer retrieved snow depth from SnowSAR on 2/21/17 at 18:11:38 GMT. The pixels are color-coded according to the SnowSAR incidence angle. c) same as (b) with pixels color-coded according to the subgrid-scale variability measured by standard deviation of LIDAR snow depth within the corresponding 30 m pixel. Pixels on the edge of forests and grasslands have higher subgridscale standard deviations (SSTD). d) Landcover distribution along the flight path; bottom panel – zoom view of area in red box. e) Spatial distribution of upscaled LIDAR snow depth SSTD at 30m; bottom panel – zoom view of area in red box. The edges of forests have higher SSTD due to errors in the LIDAR snow depth retrievals at high resolution. f) Absolute residual between retrievals and LIDAR snow depth; bottom panel – zoom view of area in red box. Residuals equal to 0.5 m and above are grouped in the same category. The red box in parts (d), (e), and (f) delineates an area with large absolute residuals. Vegetation-snowpack backscatter interactions at the grassland-forest and grassland-wetland margins not accounted for in the retrievals. Gray points in the central panel correspond to zero depth LIDAR estimates due to errors in heterogenous landcover.~~.a) Snow depth measurements using airborne LIDAR on 2/25/17, 4 days after the SnowSAR flights. b) Comparison between LIDAR snow depth and the retrieved snow depth for 2-layer snowpack for the SnowSAR on 2/21/17 at 18:11:38 GMT. The pixels are color-coded according to the incidence angle for the SnowSAR observations. c) The same comparison is shown; however, the pixels are color-coded according to the subgrid-scale variability of LIDAR snow depth within the corresponding 30 m pixel. Pixels on the edge of forests and grassland have higher standard deviations. d) Landcover distribution along the flight path. e) Spatial distribution of subgrid-scale variability of upscaled LIDAR snow depth at 30m corresponding to part c). The edges of forests have higher subgrid-scale variability due to errors in the LIDAR snow depth retrievals at high resolution. f) Absolute residual between retrieved and LIDAR snow depth. Residuals equal to 0.5 m and above are grouped in the same category. The red box in the parts d), e), and f) delineates an area with large absolute residuals. The areas on the edge of the forests have large subgrid-scale variability in the LIDAR retrievals contributing and there are vegetation-snowpack backscatter interactions that are not accounted for in the retrievals. Additionally, areas surrounding the wetlands have comparatively higher residuals than the homogenous grasslands.~~

Figure 8 shows heatmaps (density maps) to compare successful retrievals against observed X- and Ku-band VV-pol total backscatter at 30 m resolution. There is good agreement between the two values for both the bands specially in the -15 to -10 dB range without significant differences between single and two-layer snowpack retrievals. Note the positive bias in the case of X-band simulations compared to observations, whereas Ku-band has a negative bias as quantified in Table 4. Overall, the retrievals at 90 m resolution show better agreement than those at 30 m resolution due to averaging (Fig. A5).

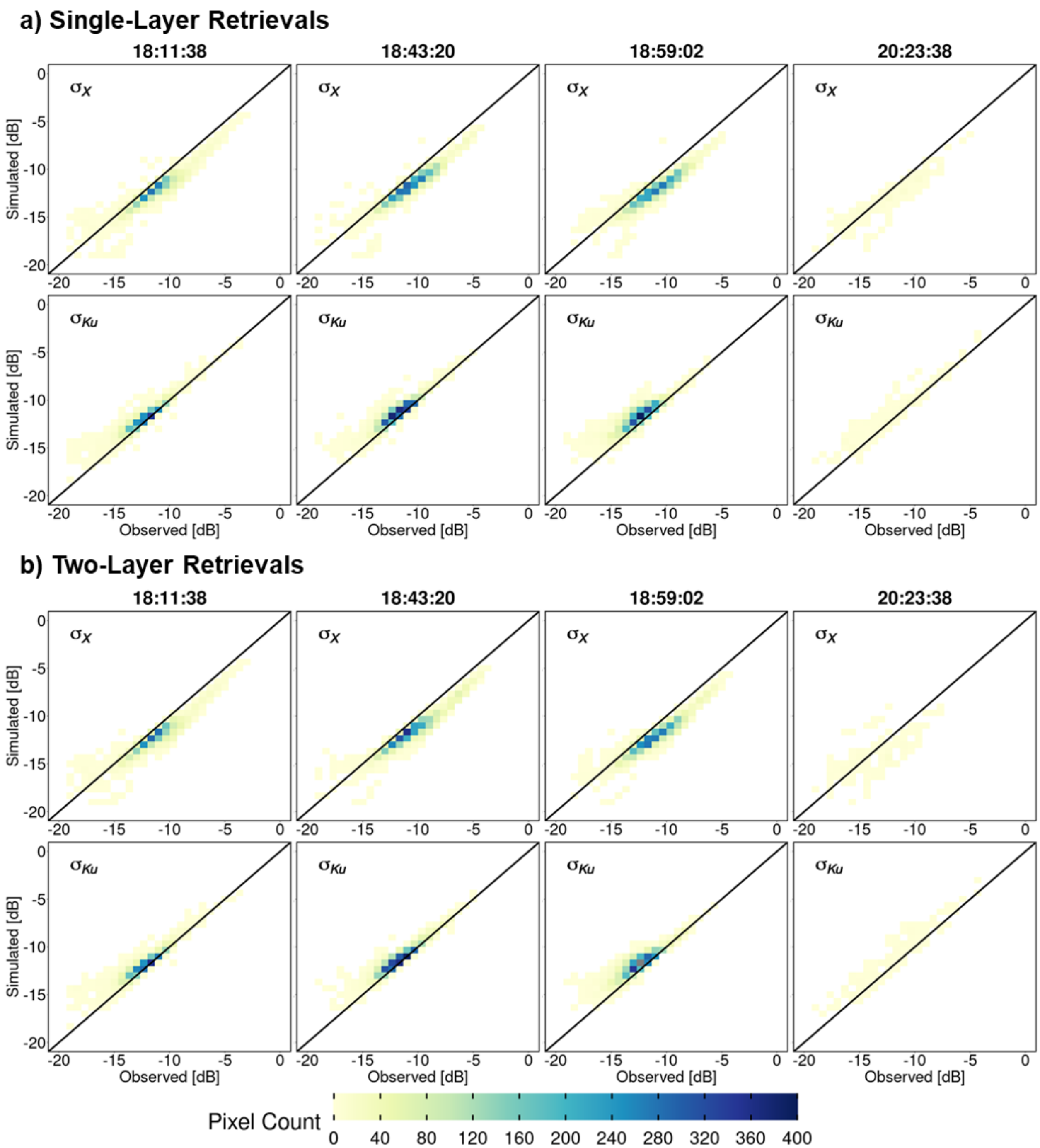

~~Figures 8 and 9 shows heatmaps to compare successful retrievals and observed X-band and Ku-band VV-pol total backscatter at 30 m resolution. There is good agreement between the two values for both the bands specially for -15 dB to -10 dB without significant differences between single~~

~~and two-layer snowpack retrievals. There is a constant positive bias in case of X-band simulations compared to observations, whereas Ku-band has a constant negative bias as quantified in Table 4. Overall, the retrievals at 90 m resolution show better agreement than those at 30 m resolution due to averaging (Figs. A5 and A6).~~

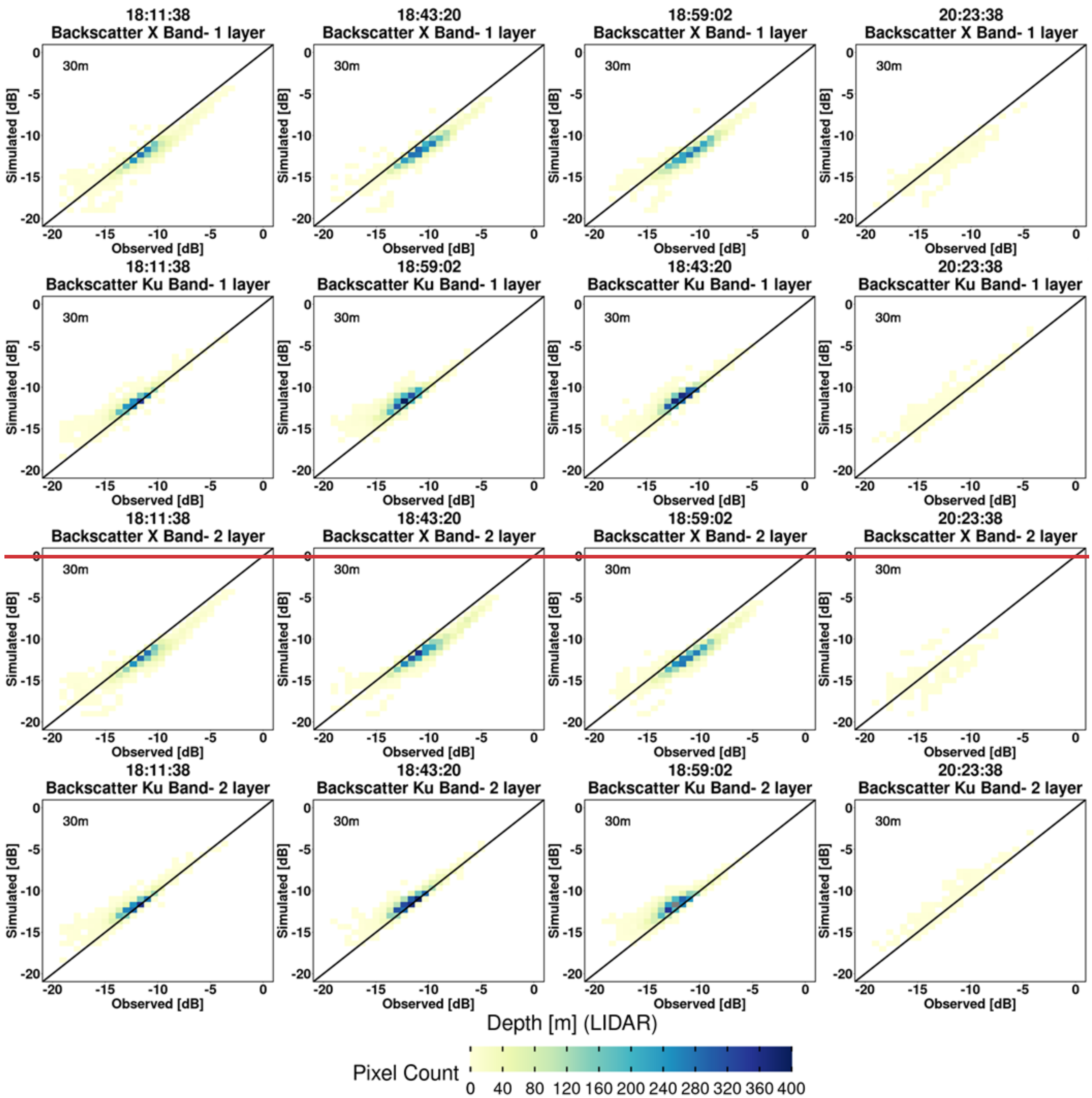

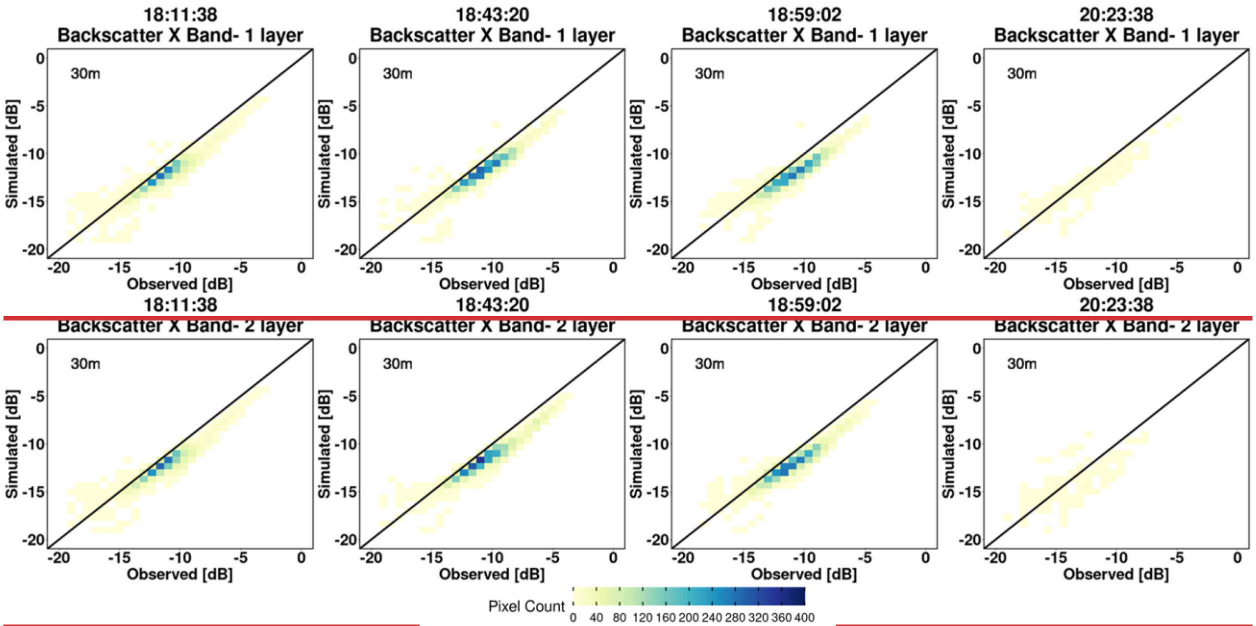

~~**Figure 8:** Heatmaps of SnowSAR (observed) backscatter (X~~ and Ku ~~band) versus converged (simulated) backscatter at 30 m resolution: 1-layer snowpack (top row); 2-layer snowpack (bottom row). Successful retrievals are for pixels with local incidence angles in the 30°- 45° range and relative residual backscatter (RRB) of less than 30% for each of the four flights (see Table 4).~~

Figure 8: Heatmaps of SnowSAR mesurements (observed) versus retrievals (simulated) backscatter (σ) at 30 m resolution for X- (σ_X) and Ku- (σ_{Ku}) bands: a) single-layer snowpack; and b) 2-layer snowpack. Successful retrievals are for pixels with local incidence angles in the 30°- 45° range and relative residual backscatter (RRB) of less than 30% for each of the four flights (see Table 4).

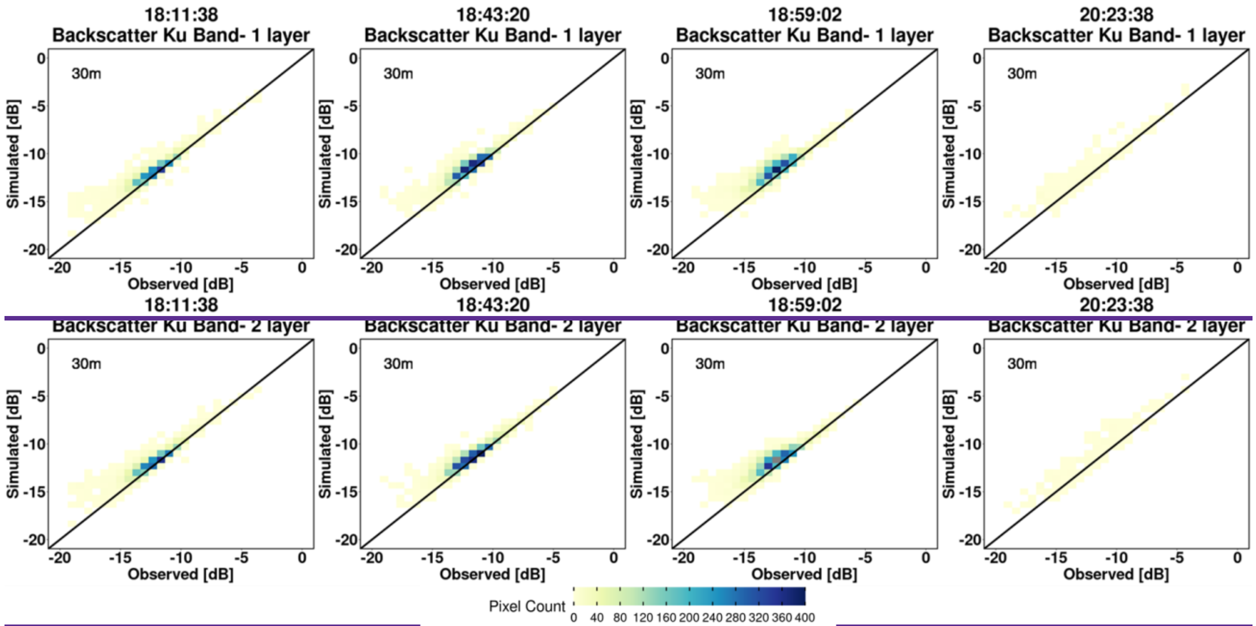

Figure 9: ~~Heatmaps of SnowSAR (observed) backscatter (Ku-band) versus converged backscatter (simulated) for successful retrievals at 30 m resolution: 1-layer snowpack (top row) and 2-layer snowpack(bottom row). Successful retrievals are for pixels with local incidence angles in the 30°–45° range and relative residual backscatter (RRB) of less than 30% for each of the four flights (see Table 4).~~

Maps of successful SWE retrievals for the four SnowSAR flight paths are shown in Fig. 9~~10~~ and Fig. A6 ~~A7~~ at 30 m and 90 m resolution, respectively. The retrievals capture well the west-east gradient in SWE, and show realistic spatial variability across Grand Mesa. The very low SWE and shallower snow depths at the easternmost boundary of the flightlines are underestimates introduced by upscaling of the SNOWSAR backscatter values where there are significant changes in topography at the edge of the Plateau (see Fig.2).

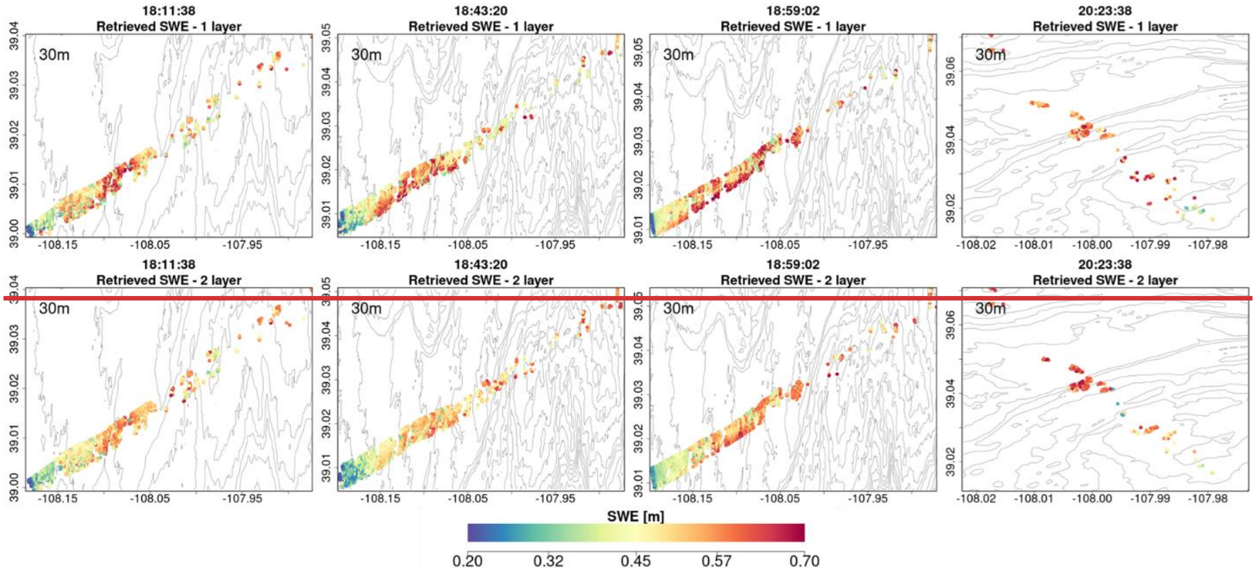

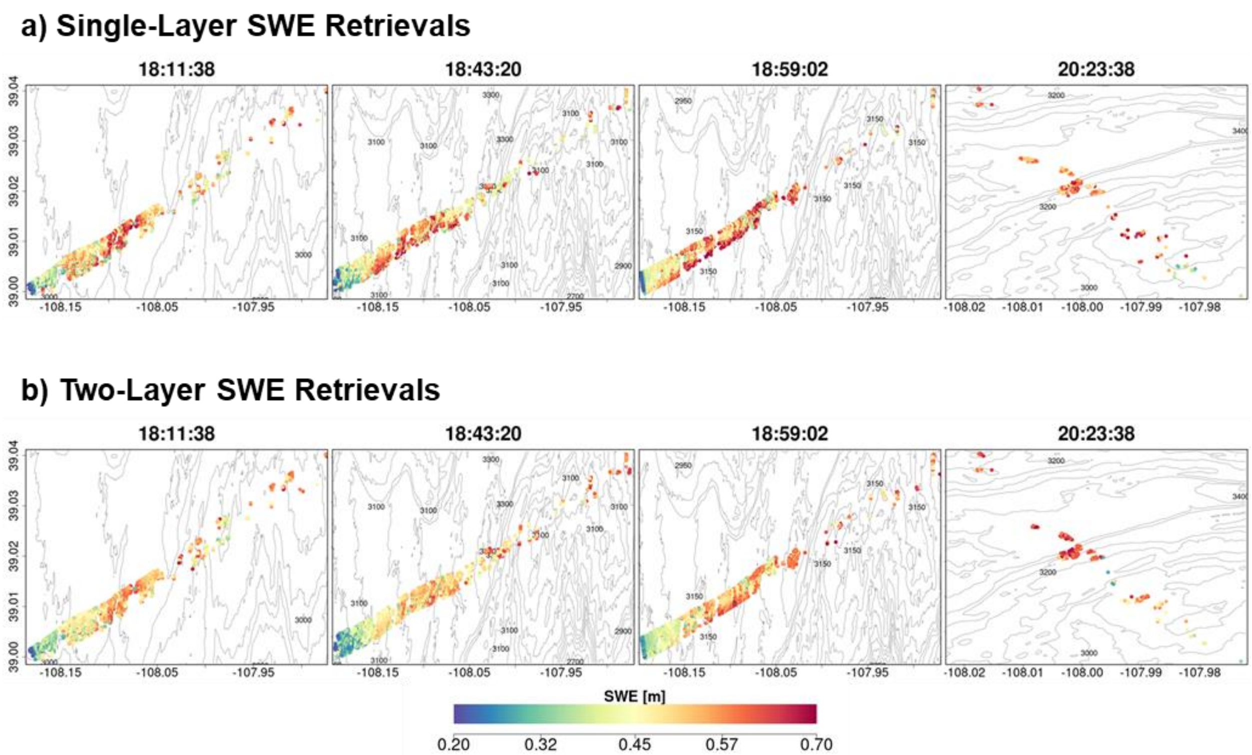

Figure 9: Spatial distribution of successful SWE retrievals for 1-layer (a) and 2-layer (b) snowpacks in grassland pixels at 30 m resolution. Successful retrievals are for pixels with local incidence angles in the 30°- 45° range and relative residual backscatter (RRB) of less than 30% for each of the four flights (see Table 4).

~~**Figure 910**: Spatial distribution of successful SWE retrievals for 1-layer and 2-layer snowpacks in grassland pixels at 30 m resolution. Successful retrievals are for pixels with local incidence angles in the 30°- 45° range and relative residual backscatter (RRB) of less than 30% for each of the four flights (see Table 4).~~

Heatmaps of total snow depth priors (MSHM predicted snow depth) against LIDAR snow depth are shown in Fig. 10~~11~~ and Figs. A7~~8~~ at 30 m and 90 m resolution and can be contrasted with heatmaps of total snow depth posteriors) against LIDAR snow depth in Figs. 11~~2~~ and A8~~123~~ using both single and two-layer retrievals. Note the narrow range of the prior snow depths concentrated around 1.5 m and the positive bias relative to LIDAR. The posteriors show much wider range of variability and deeper snow consistent with the LIDAR data for both single and two-layer retrievals, albeit with better agreement for the latter with high counts overlaying the 1:1 line at both spatial resolutions. This behavior is further confirmed by examining the snow depth histograms in Figs. A9 and A10~~at 30 m and 90m resolution~~. ~~-~~The retrievals capture well the range of the LIDAR snow depths for all flights, and there is a substantial improvement in the shape of the distributions as revealed by the heatmaps.

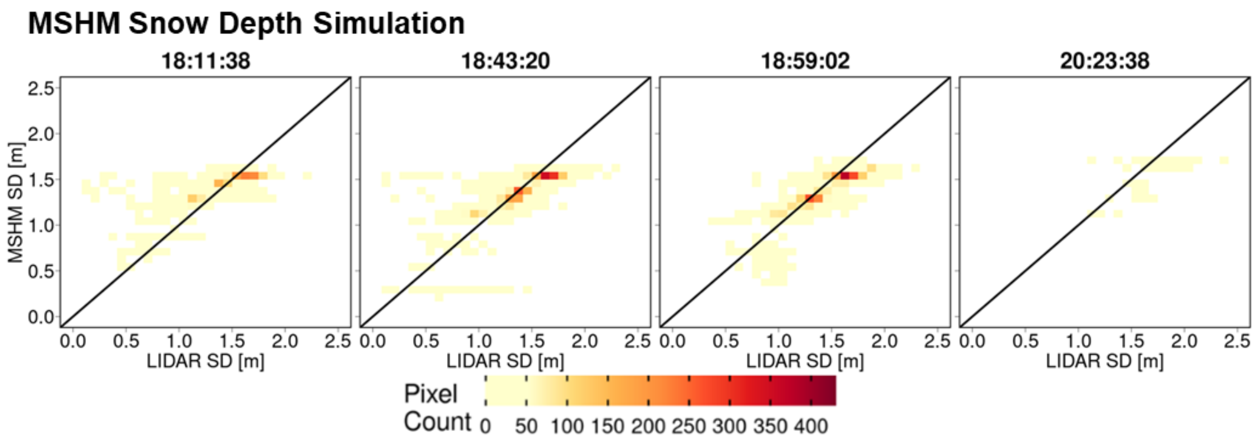

Figure 10: Heatmap of LIDAR and MSHM predicted snow depth priors at 30 m resolution using overlapping pixels from the MSHM and LIDAR. Only pixels with incidence angle between 30° -45°, and moderate sub-grid scale variability of LIDAR snow depth (< 0.3).

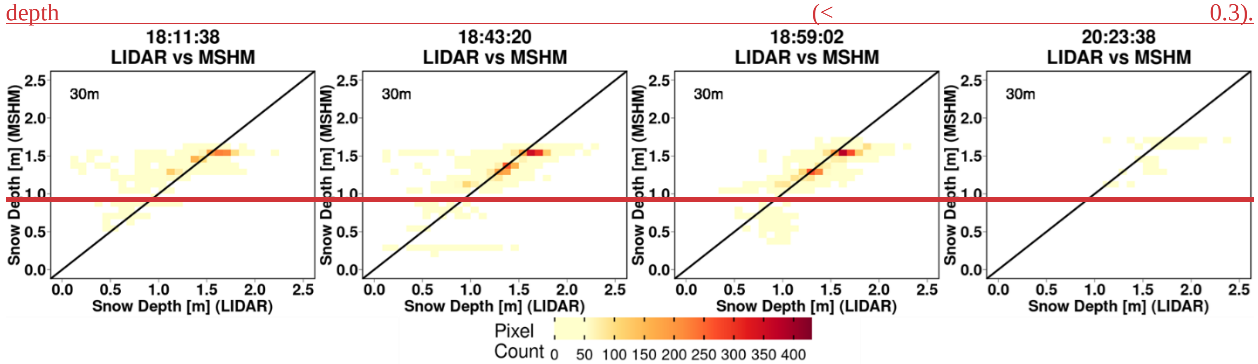

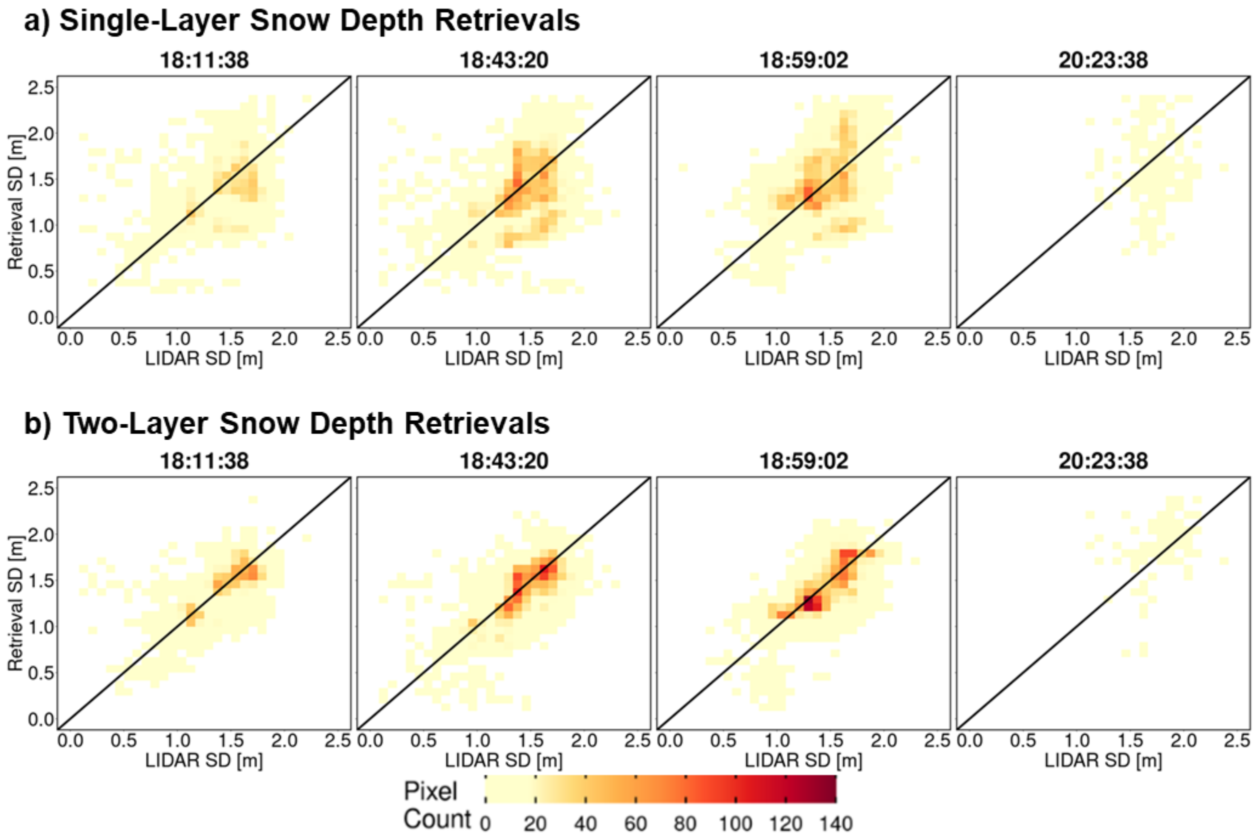

Figure 11: Heatmap of LIDAR versus successful snow depth (SD) retrievals at 30 m resolution using overlapping LIDAR and retrieval pixels. Successful retrievals are for pixels with local SnowSAR incidence angles in the 30º- 45º range and relative residual backscatter (RRB) of less than 30% for each of the four flights (see Table 4). LIDAR SD in pixels with subgrid scale variability corresponding to standard deviation of less than 0.3 m for the upscaled 90 m LIDAR pixel are not included.

~~**Figure 101:** Heatmap of LIDAR and MSHM predicted snow depth priors at 30 m resolution using overlapping pixels from the MSHM and LIDAR. Only pixels with incidence angle between 30º–45º, and moderate sub-grid scale variability of LIDAR snow depth (< 0.3).~~

Quantitative assessment metrics are presented in Tables 5 and A1~~6~~ for the comparison between various snow depth datasets at 30 and 90 m resolutions, respectively. The snow depth MARE is higher for the retrievals compared to the priors (MSHM) due to the fact that MARE is an effective metric capturing distance from the mean. CB20 showed that the MSHM simulated average snow mass accumulation at the Grand Mesa scale is within 10% of observations at a monthly time-scale in February 2017. The BC coefficients The BC coefficients of 0.95 and above at 30 m resolution indicate ~~show~~ significant agreement between ~~in~~ the shapes of the distributions at 0.95 or above at 30m resolution using the two-layer retrievals for the west-east flights, and 0.76 for the fourth flight ~~over the forest area~~ at 20:23:38 GMT over the forested area. There is significant improvement relative to MSHM priors in the statistical similarity of the snow depth retrievals vis-à-vis the LIDAR data for all cases, and more so for the fourth flight over the forest. ~~—~~For snow depth, 30 m resolution and two-layer retrievals outperform the 90 m resolution and single-layer retrievals for all flights.~~In all cases, 30 m retrievals and two-layer retrievals performed better than 90 m and single-layer retrievals for snow depth.~~ This is explained in part by landcover classification errors that are smaller at 30 m. Figure A11 shows that the number of pixels where retrievals produce large mean absolute residuals is very small and characterize by low confidence in the LIDAR estimates.

Table 5: Summary of statistics and error metrics of the 3 snow depth (SD) data sets at 30 m resolution: LIDAR measurements, MSHM predictions, and successful SnowSAR retrievals for grassland pixels and subgrid-scale standard deviation (σ) of less than 0.3 m for the upscaled LIDAR pixel. MARE – Mean Absolute Relative Error (Eq. 6); BC – Bhattacharya Coefficient (Eq. 7). Here mean and standard deviation refer to the spatial distribution, unlike the prior mean and standard deviation used in Base-AM (Table 3). Successful retrievals are for pixels with local incidence angles in the 30°- 45° range and relative residual backscatter (RRB) of less than 30% for each of the four flights (see Table 4).

Flight (GMT)	**N Layer**	**Spatial SD μ [m]**			**Spatial SD σ [m]**			**MARE SD**		**BC SD**	
		Retrieved	**MSHM**	**LIDAR**	**Retrieved**	**MSHM**	**LIDAR**	**Retrieved-LIDAR**	**MSHM-LIDAR**	**Retrieved-LIDAR**	**MSHM-LIDAR**
18:11:38	1	1.39	1.42	1.42	0.32	0.15	0.28	0.19	0.11	0.94	0.67
18:43:20		1.41	1.38	1.42	0.32	0.21	0.27	0.18	0.11	0.96	0.75
18:59:02		1.49	1.38	1.44	0.33	0.20	0.27	0.18	0.09	0.94	0.76
20:23:38		1.66	1.58	1.77	0.36	0.16	0.22	0.21	0.13	0.71	0.25
18:11:38	2	1.38	1.41	1.40	0.30	0.17	0.29	0.14	0.12	0.98	0.67
18:43:20		1.35	1.38	1.42	0.31	0.20	0.28	0.14	0.11	0.97	0.75
18:59:02		1.40	1.38	1.44	0.31	0.20	0.27	0.12	0.09	0.95	0.75
20:23:38		1.89	1.61	1.80	0.39	0.14	0.24	0.17	0.12	0.76	0.23

Tables 6 and A2 summarize the average absolute relative errors between snowpits and SWE retrievals from all flights within 100 m of the snowpits. The results are significantly better for two-layer snowpack retrievals. The mean absolute relative errors at 30 m resolution are 0.22 and 0.13 for 1 layer and 2 layer snowpacks respectively. The mean absolute relative errors at 90 m resolution are 0.2 and 0.12 for 1 layer and 2 layer snowpacks respectively. There is a variable number of pixels used for the calculation of the error metrics for each snow pit, which in the case of 51S is so small that it suggests the pit is not in the flight path. The large errors for pits 4500, 44E and and 53W are attributed to very heterogeneous landcover including water and forest (4500), and proximity to roads (53W and 44E). After removing these snowpits in the central area marked in Fig. A12, the average absolute relative SWE residuals are 5-7% (15-18%) for the two-layer (single-layer) retrieval algorithm.

Table 6: Evaluation of successful SWE retrievals at 30 m resolution against SWE at SnowEx'17 snow pits and retrieved snowpacks at 30 m resolution. All N pixels with centroids within 100 m of each snow pit are in the Grasslands (according to the Landcover dataset at 30 m resolution, see Table 1). SD – snow depth. Italicized rows correspond to large local MARE (Mean Absolute Relative Error, Eq. 6).

Date	**x**	**y**	**Pit SD (m)**	**Pit SWE (m)**	**Retrieved SWE (m)**	**MARE**	**N pixels**	**Avg. Dist**	**Pit ID**

					1 Lyr	2 Lyr	1 Lyr	2 Lyr		(m)	
2/20/2017	-108.184	39.014	1.15	0.368	0.455	0.386	0.236	0.049	28	18	KC1C
2/20/2017	-108.184	39.014	1.19	0.386	0.457	0.387	0.184	0.003	27	12	KC1E
2/20/2017	-108.184	39.014	1.18	0.386	0.456	0.387	0.181	0.003	26	15	KC1N
2/20/2017	-108.184	39.013	1.24	0.414	0.456	0.387	0.101	0.065	27	20	KC1S
2/20/2017	-108.184	39.014	1.30	0.435	0.455	0.385	0.046	0.115	29	11	KC1W
2/22/2017	-108.136	39.006	1.32	0.436	0.556	0.484	0.275	0.110	22	8	29E
2/22/2017	-108.090	39.021	1.65	0.583	0.685	0.596	0.175	0.022	19	17	38E
2/22/2017	*-108.060*	*39.030*	*2.10*	*0.763*	*0.368*	*0.449*	*0.518*	*0.412*	*12*	*16*	*53W*
2/22/2017	-108.044	39.017	1.68	0.566	0.480	0.505	0.152	0.108	5	51	63E
2/22/2017	-108.049	39.017	1.49	0.48	0.494	0.513	0.029	0.069	13	29	63W
2/22/2017	-108.029	39.032	1.66	0.55	0.558	0.581	0.015	0.056	18	15	67N
2/23/2017	*-108.067*	*39.029*	*2.13*	*0.761*	*0.593*	*0.504*	*0.221*	*0.338*	*9*	*23*	*44E*
2/23/2017	*-108.061*	*39.030*	*1.59*	*0.568*	*0.365*	*0.408*	*0.357*	*0.282*	*3*	*75*	*51S*
2/24/2017	-108.033	39.030	1.80	0.576	0.657	0.573	0.141	0.005	20	10	0
2/24/2017	-108.033	39.030	1.84	0.598	0.652	0.581	0.090	0.028	21	14	800
2/24/2017	-108.033	39.030	1.80	0.571	0.650	0.581	0.138	0.018	22	19	1390
2/24/2017	-108.033	39.030	1.75	0.566	0.654	0.581	0.155	0.027	21	15	2000
2/24/2017	-108.033	39.030	1.67	0.560	0.654	0.581	0.168	0.037	21	9	2500
2/24/2017	*-108.034*	*39.030*	*1.12*	*0.331*	*0.660*	*0.580*	*0.994*	*0.752*	*18*	*19*	*4500*
Mean			1.56	0.52	0.54	0.50	0.22	0.13	19.00	20.84	

Finally, composite spatial maps of successful SWE retrievals from all flights overlain by the snowpit measurements between 20-24 February are shown in Fig. 12. Because of the different viewing geometries, retrievals between incident angles 30º-35º for flight path at 18:59:02 in the composite of overlapping flight paths at 18:43:20 and 18:59:02 GMT were removed. Note the consistency at 30 m and 90 m resolutions as well as the overall agreement between SWE at snowpits and SWE retrievals on the flightlines.

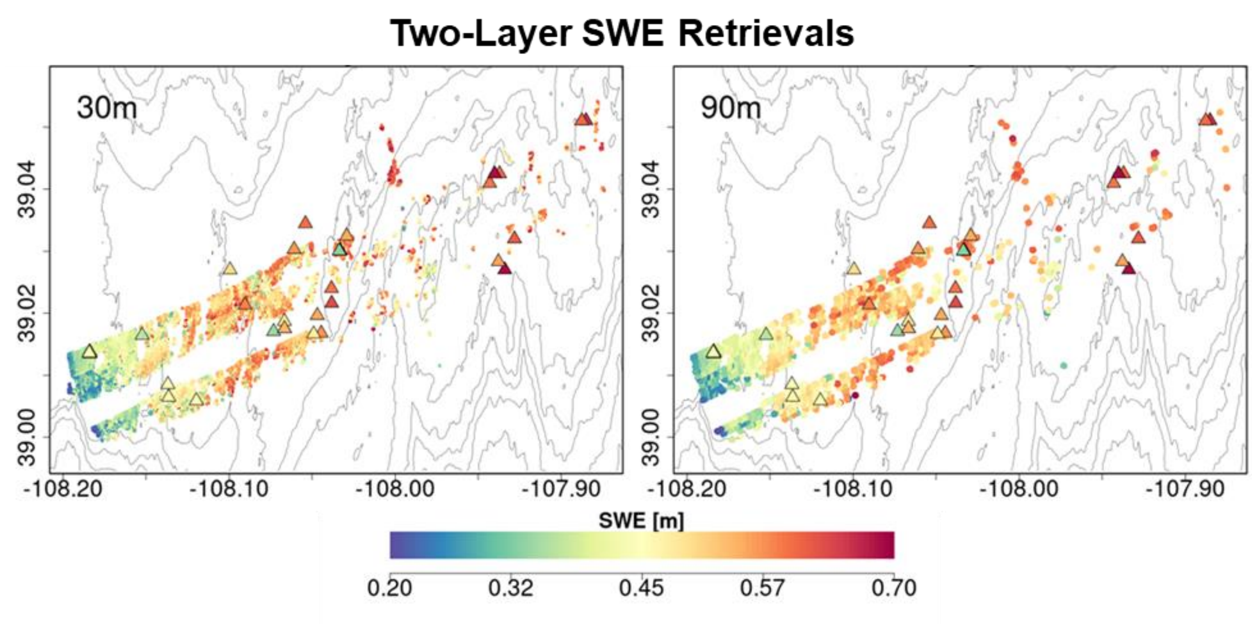

Figure 12: Composite spatial distribution of SWE (2-layer retrievals) successfully retrieved at 30m (left) and 90m (right) resolution for grassland pixels for the four SnowSAR flights. Snow pits (20-24 Feb, Fig. 4, Tables 6) are marked by triangles colored according to SWE. SnowEx'17 snow pit locations are marked by triangles and colored according to SWE. Successful retrievals are for pixels with local incidence angles in the 30°- 45° range and relative residual backscatter (RRB) of less than 30% for each of the four flights (see Table 4). As two flights Gray elevation contours are plotted every 100m.

6. Conclusion

A Bayesian physical-statistical SWE retrieval framework leveraging prior work (CB20, CB23, P17, P23, Fig. 5) was applied to airborne X- and Ku-band measurements yielding robust results from multiple SnowSAR flights over grassland and mixed grassland and forest in Grand Mesa, Colorado. Prior distributions of snowpack parameters were obtained from a multilayer snow hydrology model with atmospheric forcing derived from operational NWP forecasts and analysis (CB20, CB23). In order to reconcile the number of independent measurements, physical constraints, and reduce the number of snowpack parameters, snowpack stratigraphy was mapped into single-layer and two-layer snowpacks and then Bayesian inference using Base-AM was applied (P17, P23). The SnowSAR measurements were averaged to 30 and 90 m resolutions, and retrievals were conducted independently for every measurement pixel along the flight lines. Retrievals for measurements with convergence backscatter relative errors less than 30% (±1.2dB) and for incidence angles in the 30°- 45° range were considered successful over grasslands, corresponding to 75 -87% of all retrievals depending on the flight.

The retrievals, specifically the local means of the posterior distributions, were evaluated against the spatial distribution of LIDAR snow depth estimates up to 2 m and against snowpit SWE measurements up to 700 mm and snow depth up to 2.13 m. Since the LIDAR and snowpit measurements were not concurrent with the SnowSAR flights, the assessment of retrieval skill was conducted over a period of five days without snowfall or significant day-to-day weather changes. The two-layer snowpack retrievals perform better overall capturing the observed spatial gradients of snow depth, with SWE relative errors ≤ 7% as compared with 18% for single-layer SWE retrievals, and snow depth absolute retrieval residuals 10-20% depending on landcover heterogeneity and measurement uncertainty. The statistical structure of retrieved snow depth is similar to that estimated by LIDAR, which is indicative of the retrievals ability to capture snow patterns and scaling behavior to support scientific process studies. For satellite-based monitoring from space in the context of a future snow mission, time-series of measurements would be available that should improve the estimates of the priors based on antecedent information. This is not possible for one-time observations during field experiments such as SnowEx'17, and thus improved results would be expected under realistic satellite-based applications. NWP forecasts are available worldwide and therefore this retrieval framework can be applied to SAR measurements anywhere.

The radar model used in this study (MEMLS) does incorporate snow-ground-vegetation scattering interactions. Grassland vegetation during the accumulation season is assumed to be submerged and the impact of vegetation is included in the estimation of the background backscatter (σ_{bkg}, Fig. 1). Because the landcover data are categorical, in addition to the uncertainty of the data at 30 m resolution, additional uncertainty is tied to the selection of homogeneous grassland pixels at 90 resolution, which explains some of the unsuccessful retrievals especially along the grassland-forest, shrub and wetland boundaries. The potential for estimating σ_{bkg} independently for each location as proposed by Cao and Barros (2023b) provides an alternative to simplify the retrieval workflow and target the Bayesian inference to the snowmass and volume backscatter ($\sigma_{vol}=\sigma_{total}-\sigma_{bkg}$).

Airborne measurements are characterized by large changes in viewing geometry across the flight-line and due to other factors such as variable winds and turbulence depending on weather conditions, thus pointing to improved skill from satellite platforms. Building on previous mission concepts (e.g. Rott et al. 2012) and leveraging substantial theory advances and field campaigns in the last decade, this study demonstrates the utility and effectiveness of X-and Ku-band SAR technology to remotely monitor snowmass at high spatial resolution and with accuracy and uncertainty that meet the requirements expressed in the most recent Earth Science and Applications from Space Decadal Survey (NASEM, 2018).

7. Appendix A

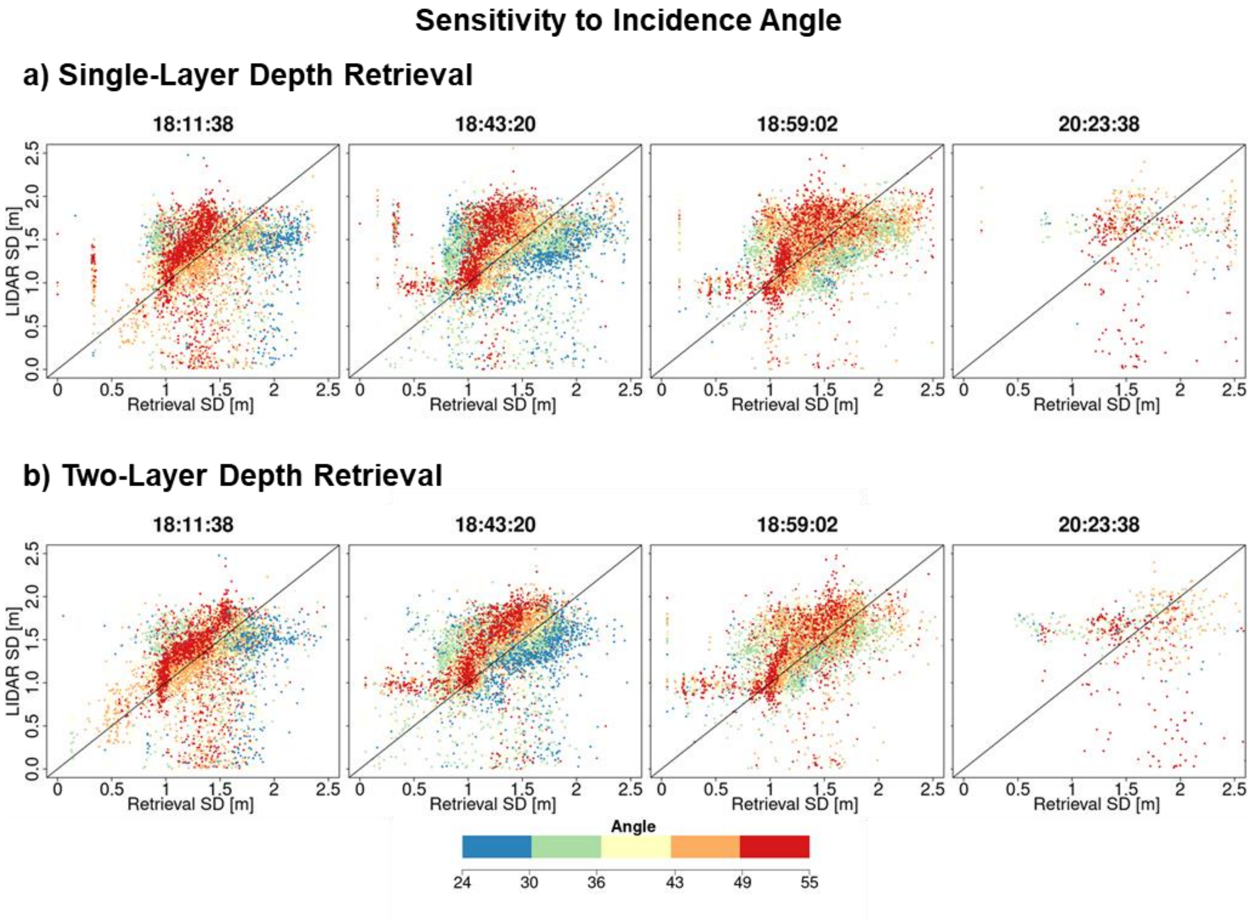

765

766

767 **Figure A1**: Same as Fig. 7b with pixels color coded according to the local SnowSAR incidence angle for all four flightlines and
768 for single-(top row) and two-layer (bottom row) retrievals at 30 m resolution.

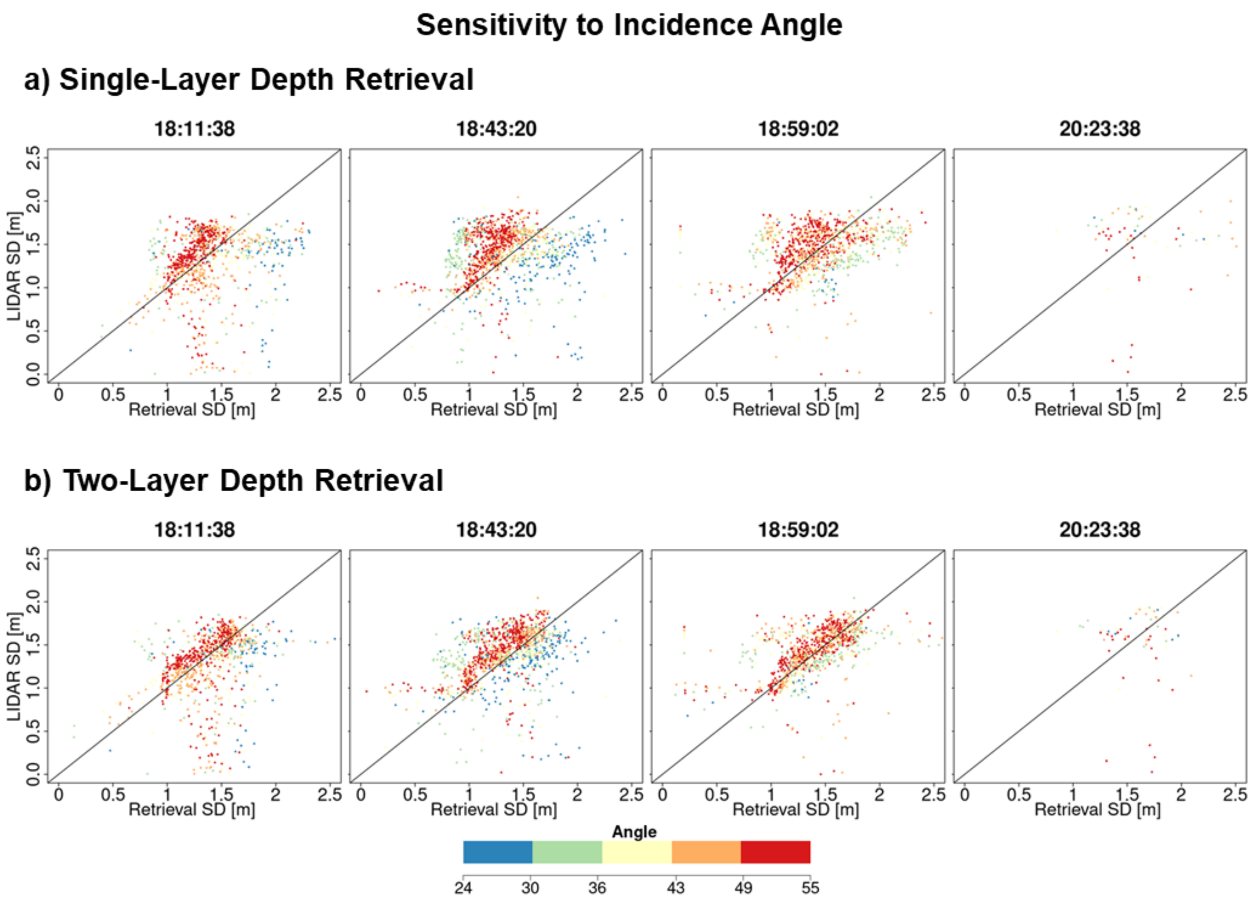

Figure A2: Same as Fig. 7b with pixels color coded according to the local SnowSAR incidence angle for all four flightlines and for single-(top row) and two-layer (bottom row) retrievals at 90 m resolution.

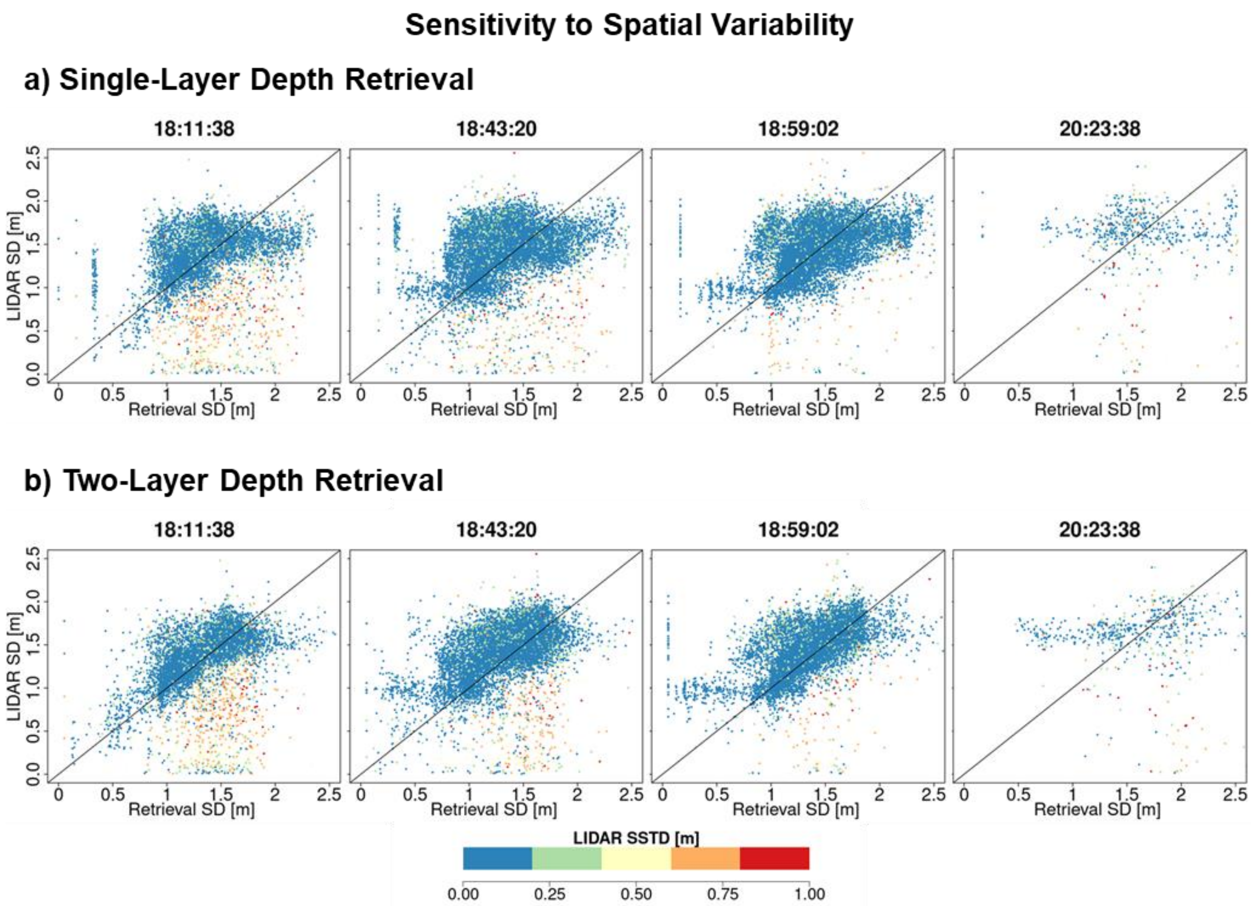

Figure A3: Comparison between LIDAR snow depth (SD) and successful retrievals for single and two-layer algorithms. The pixels are color coded according to the subgrid scale variability of the 30 m upscaled LIDAR pixel.

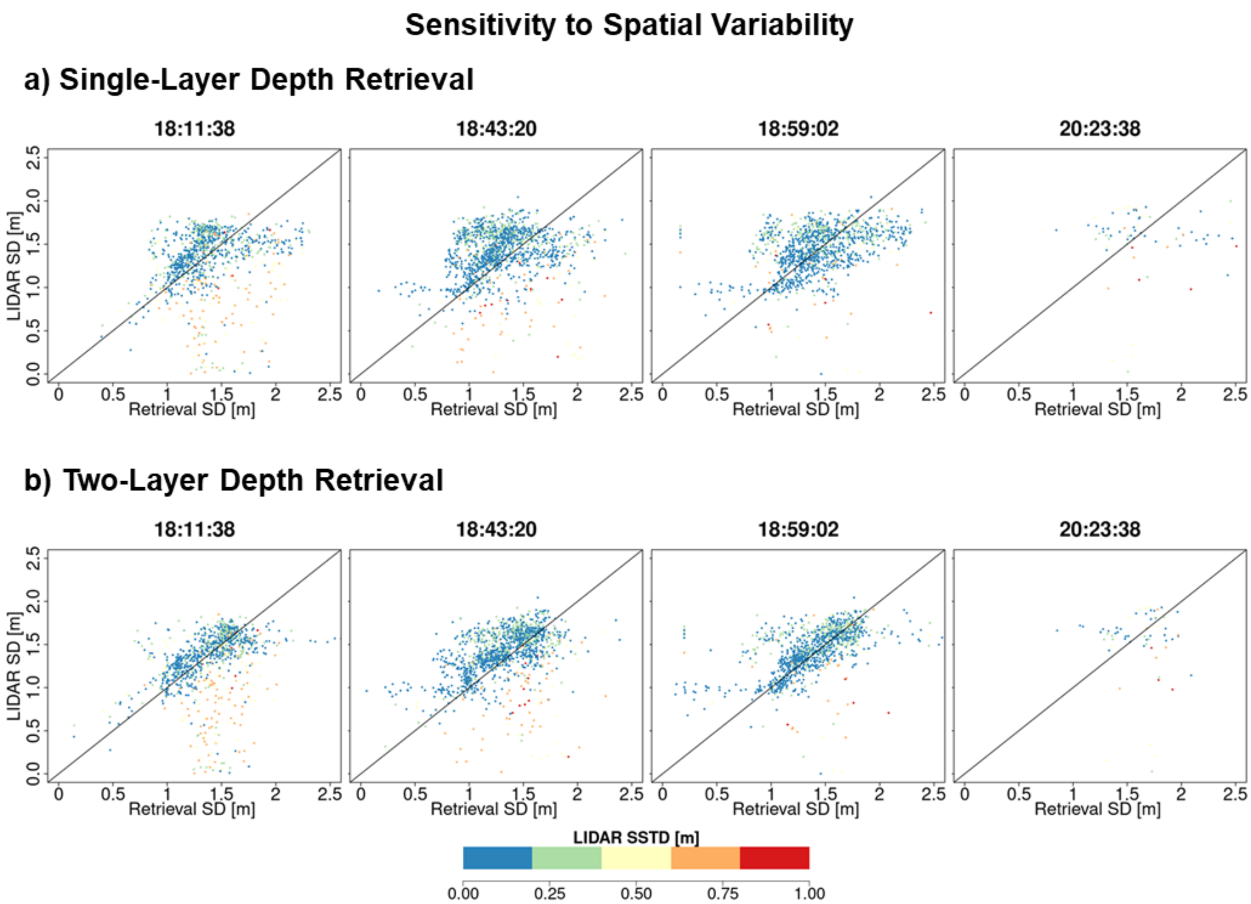

Figure A4: Comparison between SnowSAR snow depth and successful retrievals. The pixels are color coded according to the subgrid scale variability of the 90 m upscaled LIDAR pixel.

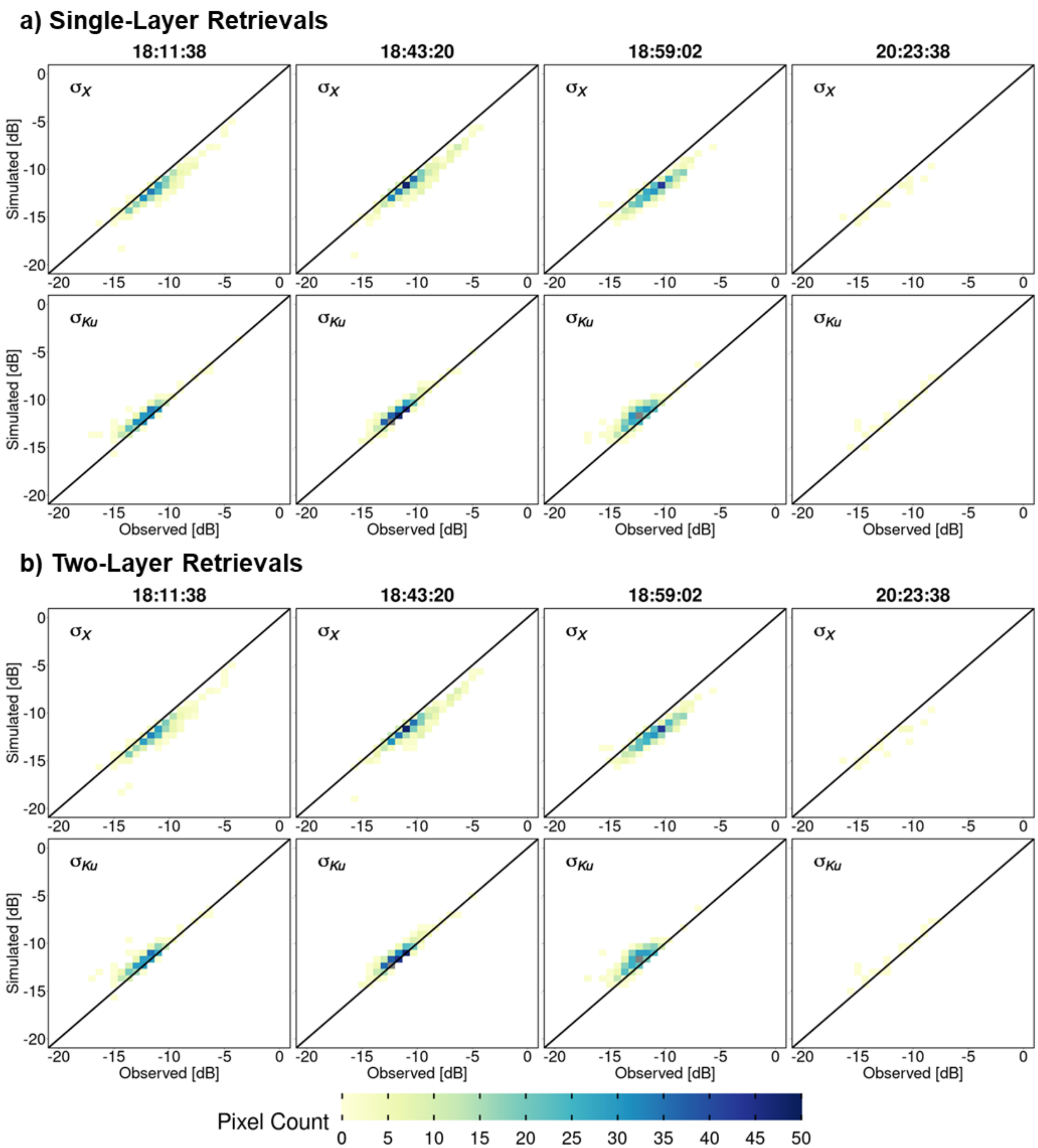

Figure A5: Heatmaps of SnowSAR backscatter mesurements (observed) versus retrievals (simulated) backscatter at 90 m resolution: a) single-layer snowpack; b) 2-layer snowpack for X-(σ_X) and Ku- (σ_{Ku}) bands. Successful retrievals are for pixels with local incidence angles in the 30°- 45° range and relative residual backscatter (RRB) of less than 30% for each of the four flights (see Table 4).

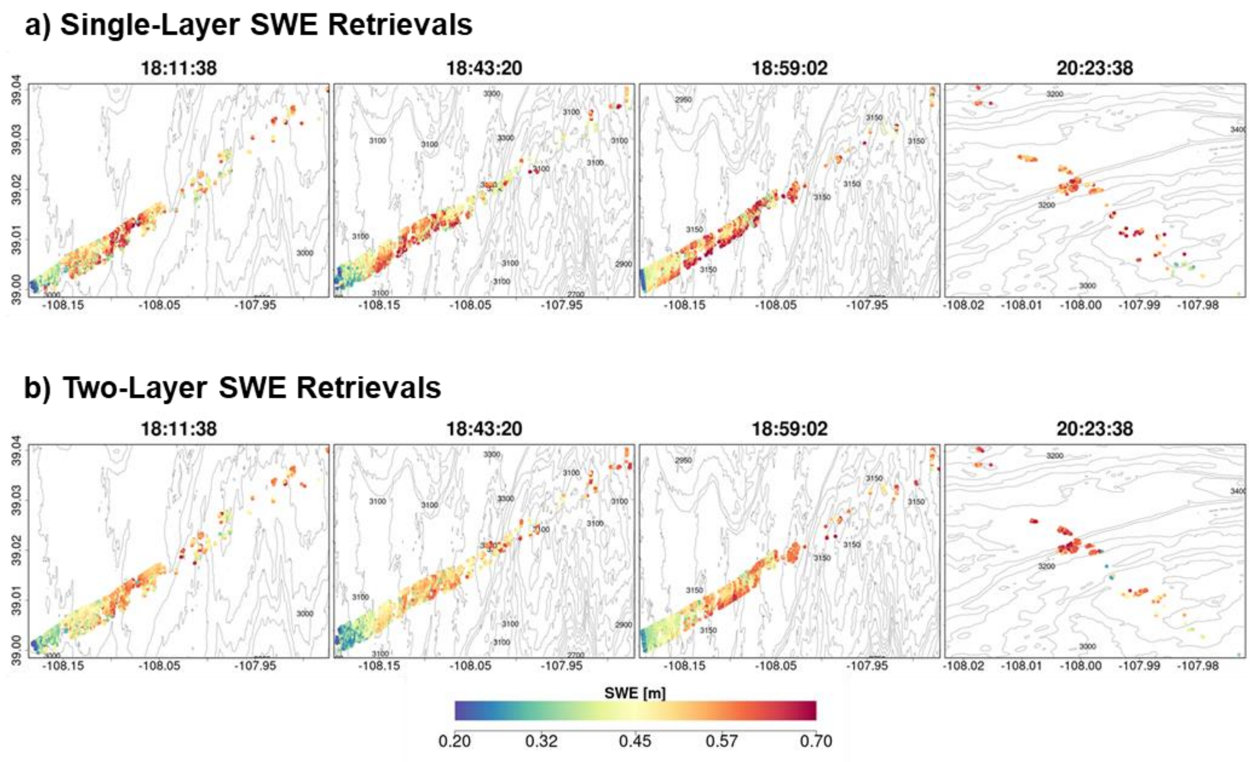

Figure A6 Spatial distribution of successful SWE retrievals for 1-layer (a) and 2-layer (b) snowpacks in grassland pixels at 90 m resolution. Successful retrievals are for pixels with local incidence angles in the 30^{o}- 45^{o} range and relative residual backscatter (RRB) of less than 30% for each of the four flights (see Table 4).

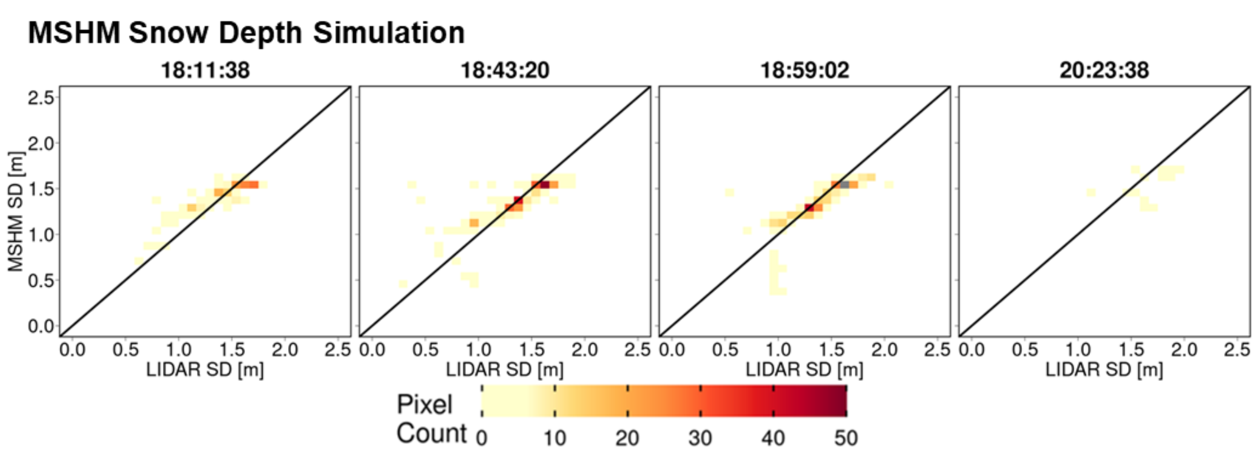

Figure A7: Heatmaps of LIDAR snow depth and snow depth predicted by MSHM at the time of SnowSAR flights for overlapping pixels at 90 m resolution.

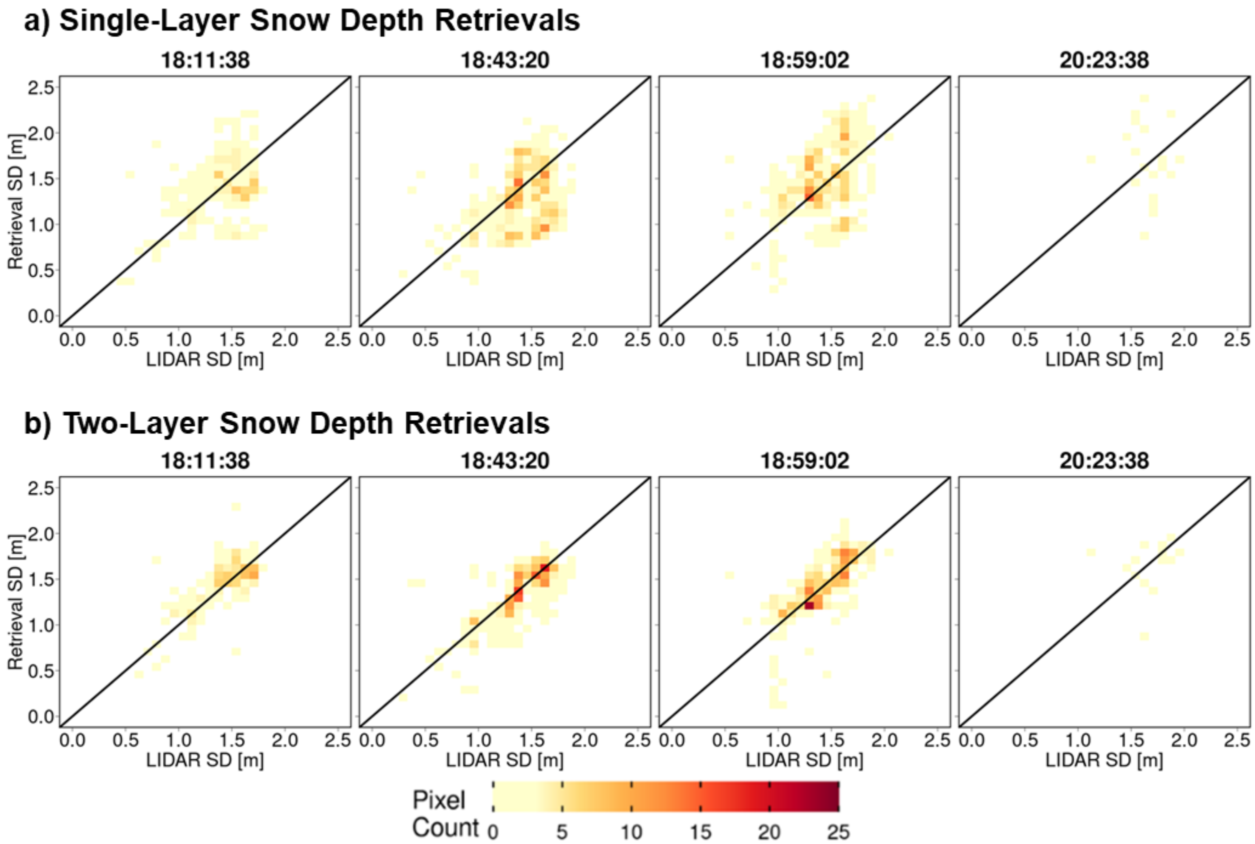

Figure A8: Heatmaps of LIDAR versus successful snow depth (SD) retrievals at 90 m resolution using overlapping LIDAR and retrieval pixels. Successful retrievals are for pixels with local SnowSAR incidence angles in the 30°- 45° range and relative residual backscatter (RRB) of less than 30% for each of the four flights (see Table 4). LIDAR SD in pixels with subgrid scale variability corresponding to standard deviation of less than 0.3 m for the upscaled 90 m LIDAR pixel are not included.

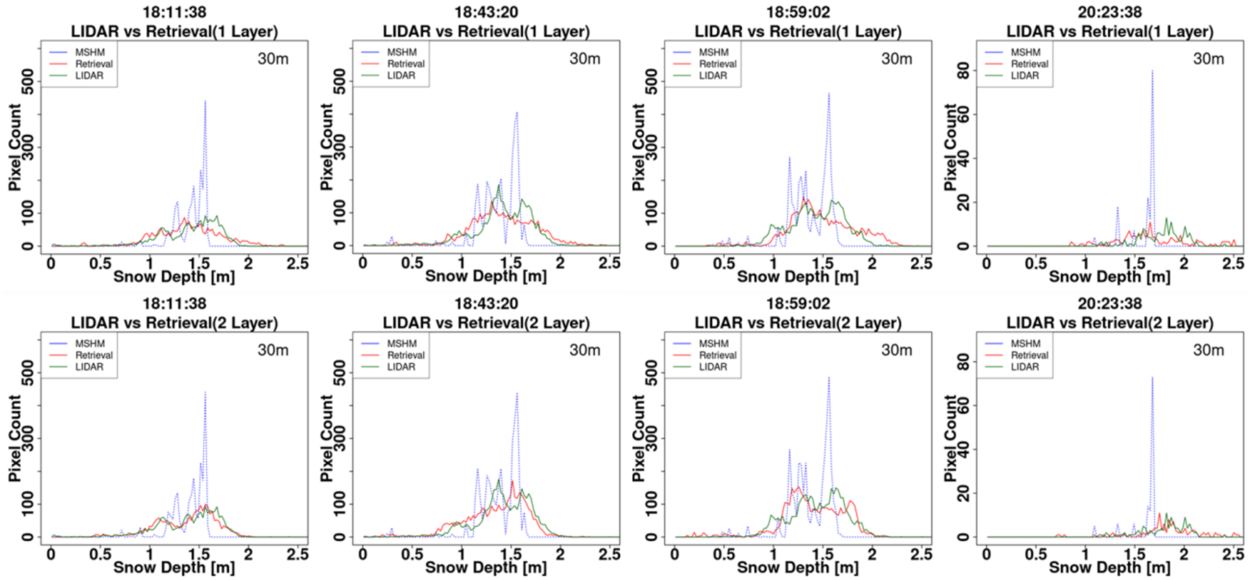

Figure A9: Histogram of snow depth (SD) from LIDAR, MSHM, and successful retrievals at 30 m using 1- and 2- layer snowpacks. The total number of pixels for each snow depth product is the same. Successful retrievals are for pixels with local incidence angles in the 30°- 45° range and relative residual backscatter (RRB) of less than 30% for each of the four flights (see Table 4). LIDAR SD in pixels with subgrid scale variability corresponding to standard deviation of less than 0.3 m for the upscaled 90 m LIDAR pixel are not included.

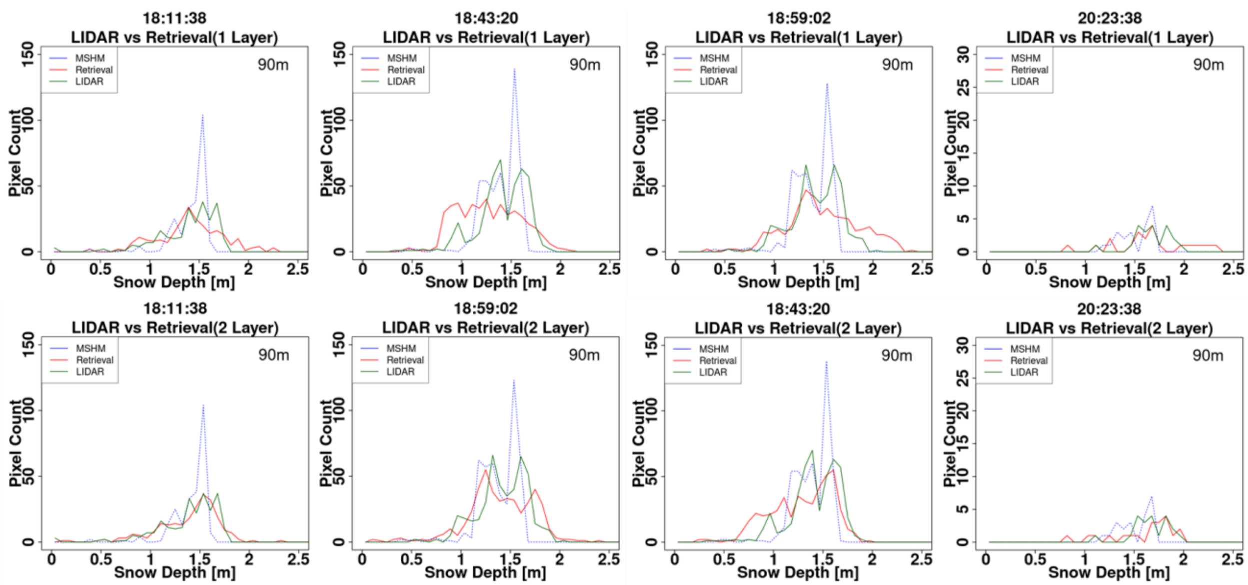

Figure A10 - Histogram of snow depth (SD) from LIDAR, MSHM, and successful retrievals at 90 m using 1- and 2- layer snowpacks. The total number of pixels for each snow depth product is the same. Successful retrievals are for pixels with local incidence angles in the 30°- 45° range and relative residual backscatter (RRB) of less than 30% for each of the four flights (see Table 4). LIDAR SD in pixels with subgrid scale variability corresponding to standard deviation of less than 0.3 m for the upscaled 90 m LIDAR pixel are not included.

Table A1 – Same as Table 5 but for resolution of 90 m.

Flight (GMT)	N Layer	Spatial SD μ [m]			Spatial SD σ [m]			MARE SD		BC SD	
		Retrieved	MSHM	LIDAR	Retrieved	MSHM	LIDAR	Retrieved -LIDAR	MSHM-LIDAR	Retrieved -LIDAR	MSHM-LIDAR
18:11:38	1	1.41	1.42	1.40	0.33	0.18	0.26	0.19	0.09	0.90	0.78
18:43:20		1.27	1.39	1.41	0.32	0.19	0.25	0.21	0.08	0.90	0.85
18:59:02		1.48	1.38	1.42	0.37	0.20	0.25	0.21	0.07	0.90	0.82
20:23:38		1.68	1.52	1.66	0.38	0.17	0.19	0.24	0.12	0.66	0.50
18:11:38	2	1.41	1.42	1.40	0.35	0.18	0.26	0.15	0.09	0.95	0.77
18:43:20		1.29	1.39	1.41	0.32	0.19	0.25	0.16	0.08	0.92	0.85
18:59:02		1.41	1.38	1.42	0.35	0.20	0.25	0.15	0.07	0.92	0.82
20:23:38		1.67	1.52	1.66	0.45	0.17	0.19	0.22	0.12	0.76	0.50

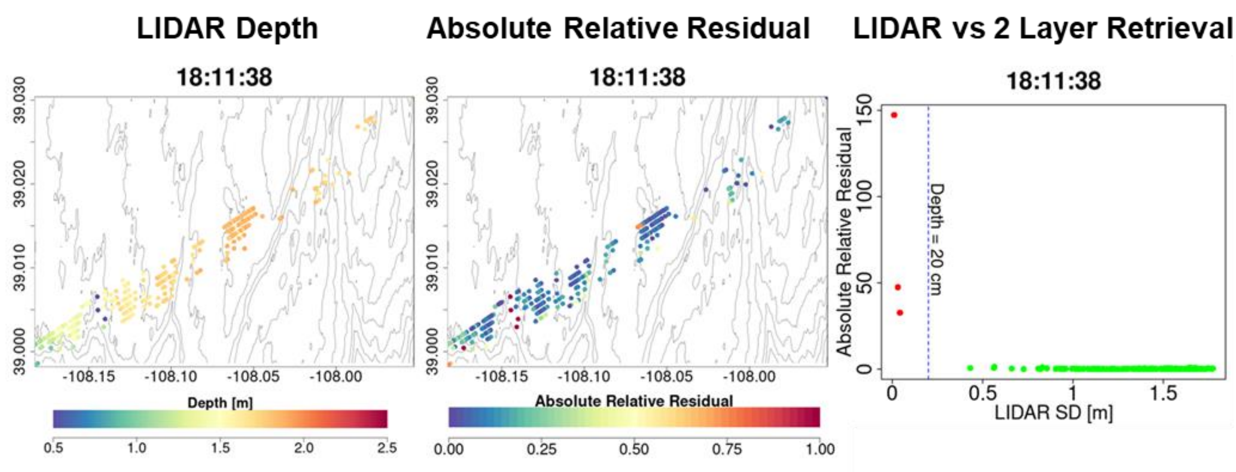

Figure A11 - Analysis of unsuccessful retrievals for pixels with large mean snow depth residuals at 90 m resolution: a) Map of LIDAR snow depth highlighting in deep blue the locations where very shallow snow is attributed to measurement error. b) Note spatial agreement between shallow snow depth and very large residuals. c)There are only a few points at the edges of forests and shallow snow depths that are flagged not successful. The gray elevation contours are plotted every 50 m.

Table A2: Same as Table 7 but for resolution of 90 m.

Date	x	y	Pit SD (m)	Pit SWE (m)	Retrieved SWE (m)		Mean Abs Rel Error		N pixels	Avg. Dist (m)	Pit ID
					1 Lyr	2 Lyr	1 Lyr	2 Lyr			
2/20/2017	-108.184	39.014	1.15	0.368	0.473	0.398	0.29	0.08	4	18	KC1C
2/20/2017	-108.184	39.014	1.19	0.386	0.471	0.397	0.22	0.03	3	12	KC1E
2/20/2017	-108.184	39.014	1.18	0.386	0.473	0.399	0.22	0.03	2	29	KC1N
2/20/2017	-108.184	39.013	1.24	0.414	0.474	0.398	0.15	0.04	3	27	KC1S
2/20/2017	-108.184	39.014	1.3	0.435	0.476	0.399	0.09	0.08	3	47	KC1W
2/22/2017	-108.136	39.006	1.32	0.436	0.572	0.490	0.31	0.12	2	39	29E
2/22/2017	*-108.060*	*39.030*	*2.10*	*0.763*	*0.340*	*0.384*	*0.55*	*0.50*	*1*	*43*	*53W*
2/22/2017	-108.044	39.017	1.68	0.566	0.454	0.499	0.20	0.12	1	75	63E
2/22/2017	-108.049	39.017	1.49	0.480	0.521	0.530	0.09	0.10	1	29	63W
2/22/2017	-108.029	39.032	1.66	0.550	0.529	0.553	0.04	0.01	4	47	67N
2/23/2017	-108.067	39.029	2.13	0.761	0.751	0.606	0.01	0.20	1	70	44E
2/24/2017	-108.033	39.030	1.8	0.576	0.718	0.601	0.25	0.04	3	60	0
2/24/2017	-108.033	39.030	1.84	0.598	0.717	0.600	0.20	0.00	2	57	800
2/24/2017	-108.033	39.030	1.80	0.571	0.717	0.600	0.26	0.05	2	55	1390
2/24/2017	-108.033	39.030	1.75	0.566	0.687	0.592	0.21	0.05	1	54	2000
2/24/2017	-108.033	39.030	1.67	0.560	0.687	0.592	0.23	0.06	1	54	2500
2/24/2017	*-108.034*	*39.030*	*1.12*	*0.331*	*0.687*	*0.592*	*1.08*	*0.79*	*1*	*62*	*4500*
2/20/2017	-108.184	39.014	1.15	0.368	0.473	0.398	0.29	0.08	4	18	KC1C
2/20/2017	-108.184	39.014	1.19	0.386	0.471	0.397	0.22	0.03	3	12	KC1E
Mean			1.51	0.50	0.56	0.50	0.26	0.13	2.21	42.53	

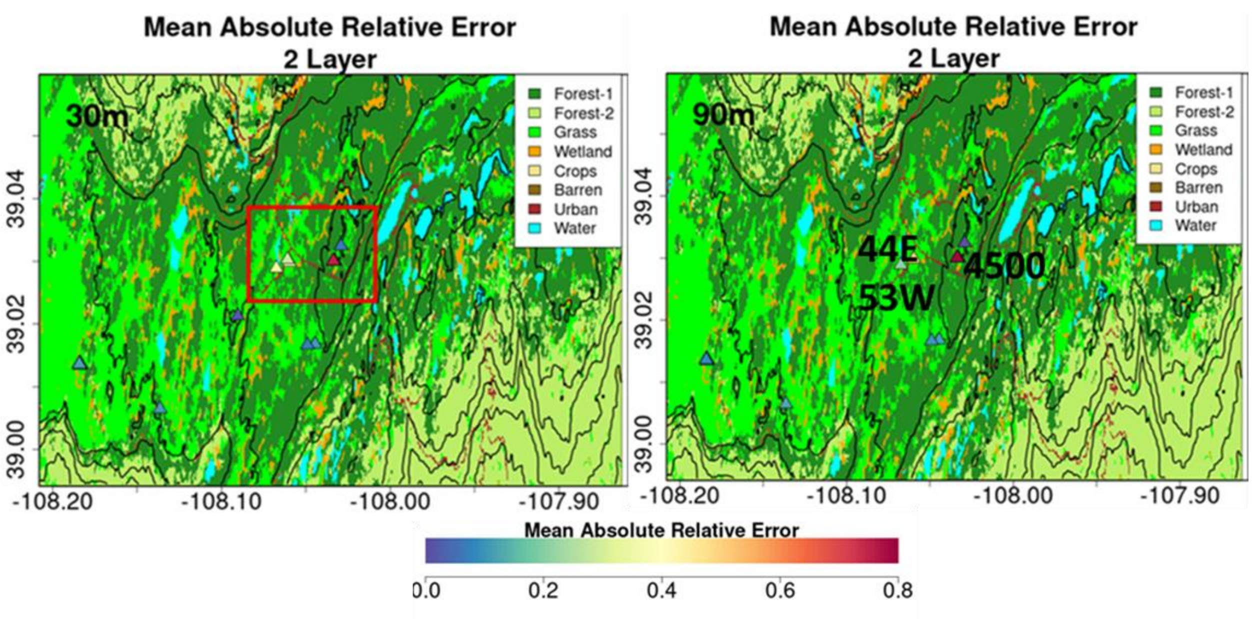

Figure A12 – Spatial context for snow pits with very large absolute relative errors (MARE) calculated as the mean of the relative difference between SWE retrievals within 100 m of the snow pit and the values at the snow pit Locations with very large errors (orange to red) are inside the red box marked in top plot. Snowpit 4500 is a region of complex land cover including evergreen forest, a road and a pond. Snowpits 53W and 44E are close to each other on the same side of the road in expansive grassland.

8. Data Availability

Links to access all datasets used in this study are provided in Table 1.

9. Author Contribution

AB and MD conceptualized the study; SS developed and implemented the retrieval framework including modifications and coupling of the codes under the guidance of AB; SS completed the retrievals and analyzed the results under the guidance of AB with input from MD; MD provided the original code of the Base-AM model; AB provided the original MSHM code; EK curated the SnowSAR dataset; SS and APB wrote the paper and replied to Reviewers with comments from MD and EK.

10~~8~~. Competing Interests

The contact author has declared that none of the authors has any competing interests

11. References

Bateni, S. M., Margulis, S. A., Podest, E., and McDonald, K. C.: Characterizing Snowpack and the Freeze–Thaw State of Underlying Soil via Assimilation of Multifrequency Passive/Active Microwave Data: A Case Study (NASA CLPX 2003), IEEE Trans. Geosci. Remote Sens., 53, 173–189, https://doi.org/10.1109/TGRS.2014.2320264, 2015.

Benjamin, S. G., Weygandt, S. S., Brown, J. M., Hu, M., Alexander, C. R., Smirnova, T. G., Olson, J. B., James, E. P., Dowell, D. C., Grell, G. A., Lin, H., Peckham, S. E., Smith, T. L., Moninger, W. R., Kenyon, J. S., and Manikin, G. S.: A North American Hourly Assimilation and Model Forecast Cycle: The Rapid Refresh, Mon. Weather Rev., 144, 1669–1694, https://doi.org/10.1175/MWR-D-15-0242.1, 2016.

Berliner, L. M.: Physical-statistical modeling in geophysics: Physical-Statistical Modeling in Geophysics, J. Geophys. Res. Atmospheres, 108, n/a-n/a, https://doi.org/10.1029/2002JD002865, 2003.

Bhattacharyya, A.: On a measure of divergence between two statistical populations defined by their probability distributions". https://doi.org/10.3390/rs12203422, 2020.

Cao, Y. and Barros, A.P.: Weather-Dependent Nonlinear Microwave Behavior of Seasonal High-Elevation Snowpacks, Remote Sens., 12, 3422, https://doi.org/10.3390/rs12203422, 2020.

Cao, Y. and Barros, A. P.: Topographic controls on active microwave behavior of mountain snowpacks, Remote Sens. Environ., 284, 113373, https://doi.org/10.1016/j.rse.2022.113373, 2023a.

Cao, Y. and Barros, A. P.: Indirect Estimation of Vegetation Contribution to Microwave Backscatter Via Triple-Frequency SAR Data, in: IGARSS 2023 - 2023 IEEE International Geoscience and Remote Sensing Symposium, Pasadena, CA, USA, 3114–3117, https://doi.org/10.1109/IGARSS52108.2023.10281754, 2023b.

Deems, J. S., Painter, T. H., and Finnegan, D. C.: Lidar measurement of snow depth: a review, J. Glaciol., 59, 467–479, https://doi.org/10.3189/2013JoG12J154, 2013.

Dobson, M., Ulaby, F., Hallikainen, M., and El-rayes, M.: Microwave Dielectric Behavior of Wet Soil-Part II: Dielectric Mixing Models, IEEE Trans. Geosci. Remote Sens., GE-23, 35–46, https://doi.org/10.1109/TGRS.1985.289498, 1985.

Dobson, M., Ulaby, F., Hallikainen, M., and El-rayes, M.: Microwave Dielectric Behavior of Wet Soil-Part II: Dielectric Mixing Models, IEEE Trans. Geosci. Remote Sens., GE-23, 35–46, https://doi.org/10.1109/TGRS.1985.289498, 1985.

Hallikainen, M., Ulaby, F., Dobson, M., El-rayes, M., and Wu, L.: Microwave Dielectric Behavior of Wet Soil-Part 1: Empirical Models and Experimental Observations, IEEE Trans. Geosci. Remote Sens., GE-23, 25–34, https://doi.org/10.1109/TGRS.1985.289497, 1985.

Huang, X. and Swain, D. L.: Climate change is increasing the risk of a California megaflood, Sci. Adv., 8, eabq0995, https://doi.org/10.1126/sciadv.abq0995, 2022.

Jacobs, J. M., Hunsaker, A. G., Sullivan, F. B., Palace, M., Burakowski, E. A., Herrick, C., and Cho, E.: Snow depth mapping with unpiloted aerial system lidar observations: a case study in Durham, New Hampshire, United States, The Cryosphere, 15, 1485–1500, https://doi.org/10.5194/tc-15-1485-2021, 2021.

Kang, D. H. and Barros, A. P.: Observing System Simulation of Snow Microwave Emissions Over Data Sparse Regions— Part I: Single Layer Physics, IEEE Trans. Geosci. Remote Sens., 50, 1785–1805, https://doi.org/10.1109/TGRS.2011.2169073, 2012a.

Kang, D. H. and Barros, A. P.: Observing System Simulation of Snow Microwave Emissions Over Data Sparse Regions—Part II: Multilayer Physics, IEEE Trans. Geosci. Remote Sens., 50, 1806–1820, https://doi.org/10.1109/TGRS.2011.2169074, 2012b.

Kim, E., Gatebe, C., Hall, D., Newlin, J., Misakonis, A., Elder, K., Marshall, H. P., Hiemstra, C., Brucker, L., De Marco, E., Crawford, C., Kang, D. H., and Entin, J.: NASA's snowex campaign: Observing seasonal snow in a forested environment, in: 2017 IEEE International Geoscience and Remote Sensing Symposium (IGARSS), 2017 IEEE International Geoscience and Remote Sensing Symposium (IGARSS), Fort Worth, TX, 1388–1390, https://doi.org/10.1109/IGARSS.2017.8127222, 2017.

Kim, R. S., Durand, M., Li, D., Baldo, E., Margulis, S. A., Dumont, M., and Morin, S.: Estimating alpine snow depth by combining multifrequency passive radiance observations with ensemble snowpack modeling, Remote Sens. Environ., 226, 1–15, https://doi.org/10.1016/j.rse.2019.03.016, 2019.

Kuhnert, P. M. (2017). Physical-statistical modeling. In Wiley StatsRef: Statistics Reference Online, pages 1–5. Wiley.

Li, D., Durand, M., and Margulis, S. A.: Estimating snow water equivalent in a Sierra Nevada watershed via spaceborne radiance data assimilation, Water Resour. Res., 53, 647–671, https://doi.org/10.1002/2016WR018878, 2017.

Lowman, L., and Barros, A.P.: Investigating links between climate and orography in the central Andes: Coupling erosion and precipitation using a physical-statistical model, J. Geophys. Res. Earth Surf., 119, 1322-1353,https://doi:10.1002/2013JF002940.

Manickam, S. and Barros, A.: Parsing Synthetic Aperture Radar Measurements of Snow in Complex Terrain: Scaling Behaviour and Sensitivity to Snow Wetness and Landcover, Remote Sens., 12, 483, https://doi.org/10.3390/rs12030483, 2020.

Martinec, J., Seidel, K., Burkart, U., and Baumann, R.: Areal modelling of snow water equivalent based on remote sensing techniques., XX General Assembly IUGG in Vienna, 1991.

Mendoza, P. A., Musselman, K. N., Revuelto, J., Deems, J. S., López-Moreno, J. I., and McPhee, J.: Interannual and Seasonal Variability of Snow Depth Scaling Behavior in a Subalpine Catchment, Water Resour. Res., 56, https://doi.org/10.1029/2020WR027343, 2020.

Metropolis, N., Rosenbluth, A.W., Rosenbluth, M,.N., Teller, A., and Teller, E.: Equation of State Calculations by Fast Computing Machines. The Journal of Chemical Physics, 21, 1087-1092, https://doi.org/10.1063/1.1699114, 1953.

Mote, T. L., Grundstein, A. J., Leathers, D. J., and Robinson, D. A.: A comparison of modeled, remotely sensed, and measured snow water equivalent in the northern Great Plains: Comparison of Snow Water Equivalent, Water Resour. Res., 39, https://doi.org/10.1029/2002WR001782, 2003.

Musselman, K. N., Addor, N., Vano, J. A., and Molotch, N. P.: Winter melt trends portend widespread declines in snow water resources, Nat. Clim. Change, 11, 418–424, https://doi.org/10.1038/s41558-021-01014-9, 2021.

National Academies of Sciences, Engineering, and Medicine: Thriving on Our Changing Planet: A Decadal Strategy for Earth Observation from Space. Washington, DC: The National Academies Press. https://doi.org/10.17226/24938, 2018.

Painter, Thomas H., Berisford, Daniel F., Boardman, Joseph W., Bormann, Kathryn J., Deems, Jeffrey S., Gehrke, Frank, Joyce, Michael, Laidlaw, Ross, Mattmann, Chris, McGurk, Bruce, Ramirez, Paul, Richardson, Megan, and Skiles, S. McKenzie: ASO L4 Lidar Snow Depth 3m UTM Grid, Version 1, https://doi.org/10.5067/KIE9QNVG7HP0, 2018.

Pan, J., Durand, M. T., Vander Jagt, B. J., and Liu, D.: Application of a Markov Chain Monte Carlo algorithm for snow water equivalent retrieval from passive microwave measurements, Remote Sens. Environ., 192, 150–165, https://doi.org/10.1016/j.rse.2017.02.006, 2017.

Pan, J., Durand, M., Lemmetyinen, J., Liu, D., and Shi, J.: Snow water equivalent retrieved from X- and dual Ku-band scatterometer measurements at Sodankylä using the Markov Chain Monte Carlo method, The Cryosphere Discuss. [preprint], https://doi.org/10.5194/tc-2023-85, in review, 2023.

Proksch, M., Mätzler, C., Wiesmann, A., Lemmetyinen, J., Schwank, M., Löwe, H., and Schneebeli, M.: MEMLS3&a: Microwave Emission Model of Layered Snowpacks adapted to include backscattering, Geosci. Model Dev., 8, 2611–2626, https://doi.org/10.5194/gmd-8-2611-2015, 2015.

Rott, H., Cline, D. W., Duguay, C., Essery, R., Etchevers, P., Hajnsek, I., Kern, M., Macelloni, G., Malnes, E., Pulliainen, J., and Yueh, S. H.: CoReH2O, a dual frequency radar mission for snow and ice observations, in: 2012 IEEE International Geoscience and Remote Sensing Symposium, IGARSS 2012 - 2012 IEEE International Geoscience and Remote Sensing Symposium, Munich, Germany, 5550–5553, https://doi.org/10.1109/IGARSS.2012.6352348, 2012.

Sturm, M., Taras, B., Liston, G. E., Derksen, C., Jonas, T., and Lea, J.: Estimating Snow Water Equivalent Using Snow Depth Data and Climate Classes, J. Hydrometeorol., 11, 1380–1394, https://doi.org/10.1175/2010JHM1202.1, 2010.

Tsang, L., Durand, M., Derksen, C., Barros, A. P., Kang, D.-H., Lievens, H., Marshall, H.-P., Zhu, J., Johnson, J., King, J., Lemmetyinen, J., Sandells, M., Rutter, N., Siqueira, P., Nolin, A., Osmanoglu, B., Vuyovich, C., Kim, E., Taylor, D., Merkouriadi, I., Brucker, L., Navari, M., Dumont, M., Kelly, R., Kim, R. S., Liao, T.-H., Borah, F., and Xu, X.: Review article: Global monitoring of snow water equivalent using high-frequency radar remote sensing, The Cryosphere, 16, 3531–3573, https://doi.org/10.5194/tc-16-3531-2022, 2022.

Villano, M., Ustalli, N., Dell'Amore, L., Jeon, S.-Y., Krieger, G., Moreira, A., Peixoto, M. N., and Krecke, J.: NewSpace SAR: Disruptive Concepts for Cost-Effective Earth Observation Missions, in: 2020 IEEE Radar Conference (RadarConf20), 2020 IEEE Radar Conference (RadarConf20), Florence, Italy, 1–5, https://doi.org/10.1109/RadarConf2043947.2020.9266694, 2020.

Wiesmann, A. and Mätzler, C.: Microwave Emission Model of Layered Snowpacks, Remote Sens. Environ., 70, 307–316, https://doi.org/10.1016/S0034-4257(99)00046-2, 1999.

~~**Table 5:** Summary of statistics and error metrics of the 3 snow depth (SD) data sets at 30 m resolution: LIDAR measurements, MSHM predictions, and successful SnowSAR retrievals for grassland pixels and subgrid-scale standard deviation (σ) of less than 0.3 m for the upscaled LIDAR pixel. MARE – Mean Absolute Relative Error (Eq. 6); BC – Bhattacharya Coefficient (Eq. 7). Here mean and standard deviation refer to the spatial distribution, unlike the prior mean and standard deviation used in Base-AM (Table 3). Successful retrievals are for pixels with local incidence angles in the 30°–45° range and relative residual backscatter (RRB) of less than 30% for each of the four flights (see Table 4).~~

Flight (GMT)	**N Layer**	**Spatial SD μ [m]**			**Spatial SD σ [m]**			**MARE SD**		**BC SD**	
		Retrieved	**MSHM**	**LIDAR**	**Retrieved**	**MSHM**	**LIDAR**	**Retrieved -LIDAR**	**MSHM-LIDAR**	**Retrieved -LIDAR**	**MSHM-LIDAR**
18:11:38	1	1.39	1.42	1.42	0.32	0.15	0.28	0.19	0.11	0.94	0.67
18:43:20		1.41	1.38	1.42	0.32	0.21	0.27	0.18	0.11	0.96	0.75
18:59:02		1.49	1.38	1.44	0.33	0.20	0.27	0.18	0.09	0.94	0.76
20:23:38		1.66	1.58	1.77	0.36	0.16	0.22	0.21	0.13	0.71	0.25
18:11:38	2	1.38	1.41	1.40	0.30	0.17	0.29	0.14	0.12	0.98	0.67
18:43:20		1.35	1.38	1.42	0.31	0.20	0.28	0.14	0.11	0.97	0.75
18:59:02		1.40	1.38	1.44	0.31	0.20	0.27	0.12	0.09	0.95	0.75
20:23:38		1.89	1.61	1.80	0.39	0.14	0.24	0.17	0.12	0.76	0.23

~~**Table 6** - Summary of statistics and error metrics of the 3 snow depth (SD) data sets at 90 m resolution: LIDAR measurements, MSHM predictions, and successful SnowSAR retrievals for grassland pixels and subgrid-scale standard deviation (σ) of less than 0.3 m for the upscaled LIDAR pixel. MARE – Mean Absolute Relative Error; BC – Bhattacharya Coefficient. Here mean and standard deviation refer to the spatial distribution, unlike the Prior mean and standard deviation used in Base-AM. Successful retrievals are for pixels with local incidence angles in the 30°-45° range and relative residual backscatter (RRB) of less than 30% for each of the four flights (see Table 4).~~

Flight (GMT)	**N Layer**	**Spatial SD μ [m]**			**Spatial SD σ [m]**			**MARE SD**		**BC SD**	
		Retrieved	**MSHM**	**LIDAR**	**Retrieved**	**MSHM**	**LIDAR**	**Retrieved -LIDAR**	**MSHM-LIDAR**	**Retrieved -LIDAR**	**MSHM-LIDAR**
18:11:38	1	1.41	1.42	1.40	0.33	0.18	0.26	0.19	0.09	0.90	0.78
18:43:20		1.27	1.39	1.41	0.32	0.19	0.25	0.21	0.08	0.90	0.85
18:59:02		1.48	1.38	1.42	0.37	0.20	0.25	0.21	0.07	0.90	0.82
20:23:38		1.68	1.52	1.66	0.38	0.17	0.19	0.24	0.12	0.66	0.50
18:11:38	2	1.41	1.42	1.40	0.35	0.18	0.26	0.15	0.09	0.95	0.77
18:43:20		1.29	1.39	1.41	0.32	0.19	0.25	0.16	0.08	0.92	0.85
18:59:02		1.41	1.38	1.42	0.35	0.20	0.25	0.15	0.07	0.92	0.82

~~20:23:38~~		~~1.67~~	~~1.52~~	~~1.66~~	~~0.45~~	~~0.17~~	~~0.19~~	~~0.22~~	~~0.12~~	~~0.76~~	~~0.50~~

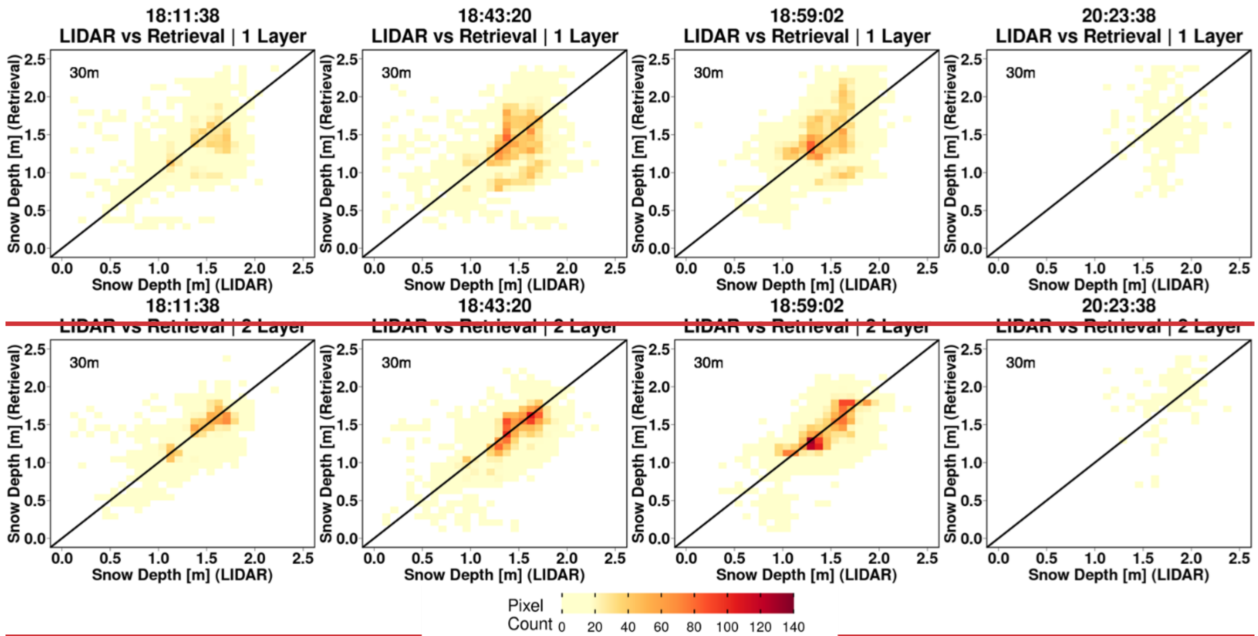

~~**Figure 112:** Heatmap of LIDAR versus successful snow depth retrievals at 30 m resolution using overlapping LIDAR and retrieval pixels. Successful retrievals are for pixels with local SnowSAR incidence angles in the 30°–45° range and relative residual backscatter (RRB) of less than 30% for each of the four flights (see Table 4). LIDAR SD in pixels with subgrid scale variability corresponding to standard deviation of less than 0.3 m for the upscaled 90 m LIDAR pixel are not included.~~

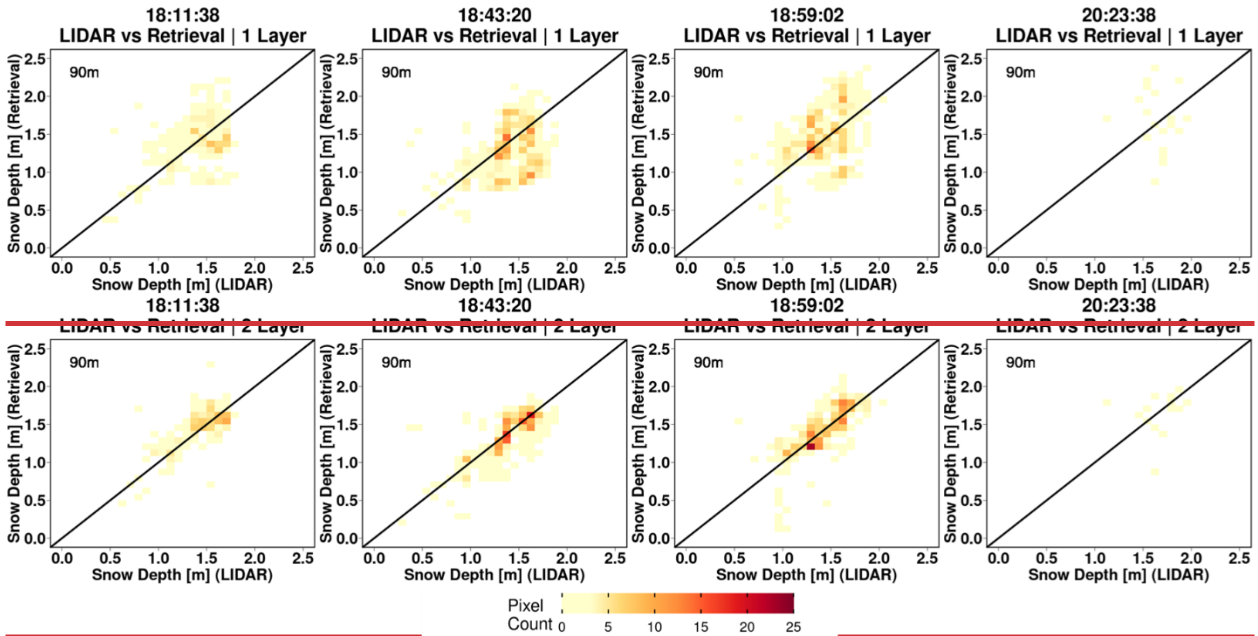

~~**Figure 123:** Heatmaps of LIDAR versus successful snow depth retrievals at 90 m resolution using overlapping LIDAR and retrieval pixels. Successful retrievals are for pixels with local SnowSAR incidence angles in the 30°–45° range and relative residual backscatter (RRB) of less than 30% for each of the four flights (see Table 4). LIDAR SD in pixels with subgrid scale variability corresponding to standard deviation of less than 0.3 m for the upscaled 90 m LIDAR pixel are not included.~~

~~Composite spatial maps of successful SWE retrievals from all flights overlain by the snowpit measurements between 20-24 February are shown in Fig. 134. Note the consistency at 30 m and 90 m resolutions as well as the overall agreement between SWE at snowpits and SWE retrievals on the flightlines. Tables 7 and 8 summarize the average absolute relative errors between snowpits and all SWE retrievals within 100 m of the snowpits. The results are significantly better for two-layer snowpack retrievals. The mean absolute relative errors at 30 m resolution are 0.22 and 0.13 for 1 layer and 2 layer snowpacks respectively. The mean absolute relative errors at 90 m resolution are 0.2 and 0.12 for 1 layer and 2 layer snowpacks respectively. There is a variable number of pixels for each snow pit, which in the case of 51S is so small that indicates it is not in the flight path. After removing snowpits in the central area marked in Fig. A12 is due to very heterogeneous landcover including water, forest, (4500) and proximity to roads (53W and 44E), the average absolute relative SWE residuals is 5-7% (15-18%) for the two-layer (single-layer) retrieval algorithm.~~

~~**Table 7:** Evaluation of successful SWE retrievals at 30 m resolution against SWE at SnowEx'17 snow pits and retrieved snowpacks at 30 m resolution. All N pixels with centroids within 100 m of each snow pit are in the Grasslands (according to the Landcover dataset at 30 m resolution, see Table 1). SD – snow depth. Shaded rows correspond to large local MARE (Mean Absolute Relative Error, Eq. 6).~~

~~**Table 8**: Evaluation of successful SWE retrievals at 90 m resolution against SWE at SnowEx'17 snow pits and retrieved snowpacks at 90 m resolution. All N pixels with centroids within 100 m of each snow pit are in the Grasslands (according to the Landcover dataset at 90 m resolution, see Table 1). SD – Snow depth. Rows in italics correspond to large local MARE (Mean Absolute Relative Error, Eq. 6).~~

~~**Date**~~	~~**x**~~	~~**y**~~	~~**Pit SD (m)**~~	~~**Pit SWE (m)**~~	~~**Retrieved SWE (m)**~~		~~**Mean Abs Rel Error**~~		~~**N pixels**~~	~~**Avg. Dist (m)**~~	~~**Pit ID**~~
					~~**1 Lyr**~~	~~**2 Lyr**~~	~~**1 Lyr**~~	~~**2 Lyr**~~			
~~2/20/2017~~	~~-108.184~~	~~39.014~~	~~1.15~~	~~0.368~~	~~0.473~~	~~0.398~~	~~0.29~~	~~0.08~~	~~4~~	~~18~~	~~KC1C~~
~~2/20/2017~~	~~-108.184~~	~~39.014~~	~~1.19~~	~~0.386~~	~~0.471~~	~~0.397~~	~~0.22~~	~~0.03~~	~~3~~	~~12~~	~~KC1E~~
~~2/20/2017~~	~~-108.184~~	~~39.014~~	~~1.18~~	~~0.386~~	~~0.473~~	~~0.399~~	~~0.22~~	~~0.03~~	~~2~~	~~29~~	~~KC1N~~
~~2/20/2017~~	~~-108.184~~	~~39.013~~	~~1.24~~	~~0.414~~	~~0.474~~	~~0.398~~	~~0.15~~	~~0.04~~	~~3~~	~~27~~	~~KC1S~~
~~2/20/2017~~	~~-108.184~~	~~39.014~~	~~1.3~~	~~0.435~~	~~0.476~~	~~0.399~~	~~0.09~~	~~0.08~~	~~3~~	~~47~~	~~KC1W~~

2/22/2017	-108.136	39.006	1.32	0.436	0.572	0.490	0.31	0.12	2	39	29E
2/22/2017	*-108.060*	*39.030*	*2.10*	*0.763*	*0.340*	*0.384*	*0.55*	*0.50*	*1*	*43*	*53W*
2/22/2017	-108.044	39.017	1.68	0.566	0.454	0.499	0.20	0.12	1	75	63E
2/22/2017	-108.049	39.017	1.49	0.480	0.521	0.530	0.09	0.10	1	29	63W
2/22/2017	-108.029	39.032	1.66	0.550	0.529	0.553	0.04	0.01	4	47	67N
2/23/2017	-108.067	39.029	2.13	0.761	0.751	0.606	0.01	0.20	1	70	44E
2/24/2017	-108.033	39.030	1.8	0.576	0.718	0.601	0.25	0.04	3	60	0
2/24/2017	-108.033	39.030	1.84	0.598	0.717	0.600	0.20	0.00	2	57	800
2/24/2017	-108.033	39.030	1.80	0.571	0.717	0.600	0.26	0.05	2	55	1390
2/24/2017	-108.033	39.030	1.75	0.566	0.687	0.592	0.21	0.05	1	54	2000
2/24/2017	-108.033	39.030	1.67	0.560	0.687	0.592	0.23	0.06	1	54	2500
2/24/2017	*-108.034*	*39.030*	*1.12*	*0.331*	*0.687*	*0.592*	*1.08*	*0.79*	*1*	*62*	*4500*
2/20/2017	-108.184	39.014	1.15	0.368	0.473	0.398	0.29	0.08	4	18	KC1C
2/20/2017	-108.184	39.014	1.19	0.386	0.471	0.397	0.22	0.03	3	12	KC1E

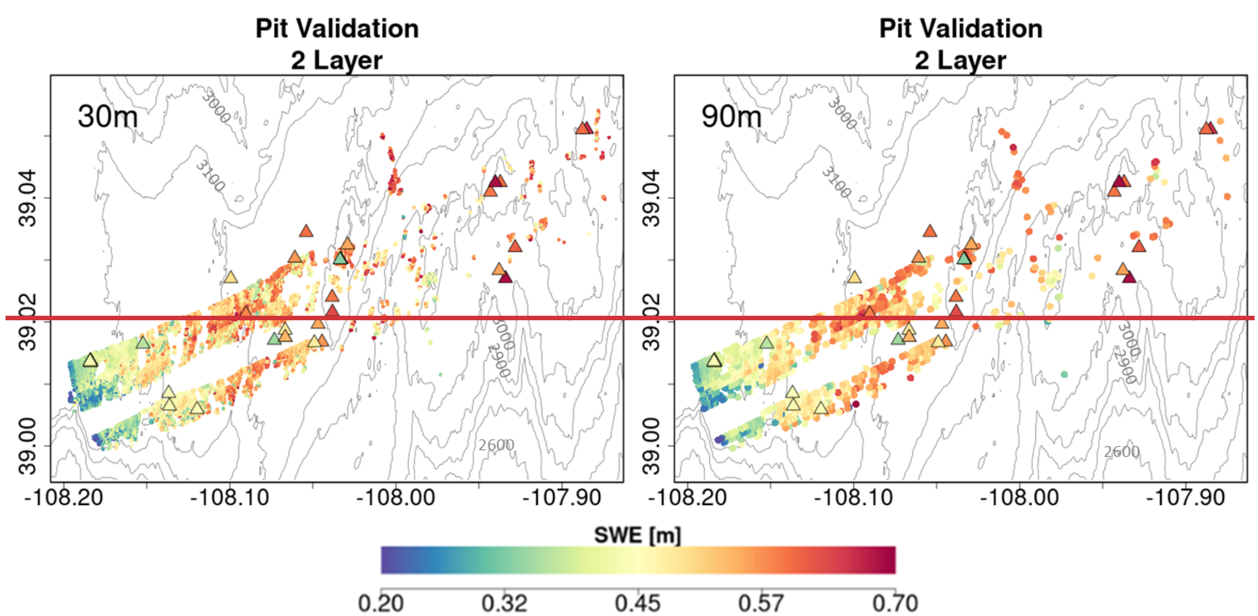

~~**Figure 134:** Composite spatial distribution of SWE (2-layer snowpack) successfully retrieved at 30m (left) and 90m (right) resolution for grassland pixels for the four SnowSAR flights. Snow pits (19-24 Feb, Fig. 4, Tables 7 and 8) are marked by triangles colored according to SWE. SnowEx'17 snow pit locations are marked by triangles and colored according to SWE. Successful retrievals are for pixels with local incidence angles in the 30°–45° range and relative residual backscatter (RRB) of less than 30% for each of the four flights (see Table 4). Gray elevation contours are plotted every 100m.~~

~~6. Conclusion~~

~~A Bayesian physical-statistical SWE retrieval framework leveraging prior work (CB20, CB22, P17, P23, Fig. 5) was applied to airborne X- and Ku-band measurements yielding robust results for multiple flights including overlapping paths over grassland and mixed grassland and forest in Grand Mesa, Colorado. Prior distributions of snowpack parameters were obtained from a multilayer snow hydrology model with atmospheric forcing derived from operational NWP forecasts and analysis (CB20, CB22). In order to reconcile the number of independent measurements, physical constraints, and reduce the number of snowpack parameters, snowpack stratigraphy was mapped into single-layer and two-layer snowpacks for Bayesian inference using Base-AM (P17, P23). The SnowSAR measurements were averaged to 30 and 90 m resolutions, and retrievals were conducted for every measurement pixel along the flight lines. Retrievals for measurements with convergence backscatter relative errors less than 30% (±1.2dB) and for incidence angles in the 30º-45º range were considered successful over grasslands, corresponding to 75-87% of all retrievals.~~

~~The retrievals (i.e. the local mean of the posterior distribution) were evaluated against the spatial distribution of LIDAR snow depth estimates up to 2 m and against snowpit SWE measurements up to 700 mm. Note that the LIDAR and snowpit measurements are not at the same time of the SnowSAR flights, and the assessment of retrieval skill was conducted over a period of five days without snowfall or significant day-to-day weather changes. The two-layer snowpack retrievals perform better overall being able to capture the statistical variability of snow depth with high fidelity, with SWE relative errors ≤ 7% as compared with 18% for single-layer SWE retrievals, and snow depth absolute retrieval residuals 10-20% depending on landcover heterogeneity and measurement uncertainty. The statistical structure of retrieved snow depth is similar to that estimated by LIDAR, which is indicative of the retrievals ability to capture snow patterns and scaling behavior to support process studies. For satellite-based monitoring from space in the context of a future snow mission, time-series of measurements would be available that should improve the estimates of the priors for the present retrieval cycle. This is not possible for field experiments such as SnowEx'17, and thus improved results would be expected under realistic satellite-based applications. NWP forecasts are available worldwide and therefore this retrieval framework can be applied to SAR measurements anywhere.~~

~~The radar model used in this study (MEMLS) does incorporate snow-ground-vegetation scattering interactions. Grassland vegetation during the accumulation season is assumed to be submerged and the impact of vegetation is included in the estimation of the background backscatter (σ_{bkg}, Fig. 1). Because the landcover data are categorical, in addition to the uncertainty of the data at 30 m resolution, additional uncertainty is tied to the selection of homogeneous grassland pixels at 90 resolution, which explains some of the unsuccessful retrievals especially along the grassland-forest and shrub boundaries. The potential for estimating σ_{bkg} independently for each location as proposed by Cao and Barros (2023) provides an alternative to simplify the retrieval workflow and target the Bayesian inference to the snowmass and volume backscatter (σ_{vol}=σ_{total}−σ_{bkg}).~~

~~Airborne measurements are characterized by large changes in viewing geometry across the flight-line and due to other factors such as variable winds and turbulence depending on weather conditions, thus pointing to improved skill from satellite platforms. Building on previous mission concepts (e.g. Rott et al. 2012) and leveraging substantial theory advances and field campaigns in the last decade, this study demonstrates the utility and effectiveness of X-and Ku-band SAR technology to remotely monitor snowmass at high spatial resolution and with accuracy and uncertainty that meet the requirements expressed in the most recent Earth Science and Applications from Space Decadal Survey (NASEM, 2018).~~

~~7. Appendix A~~

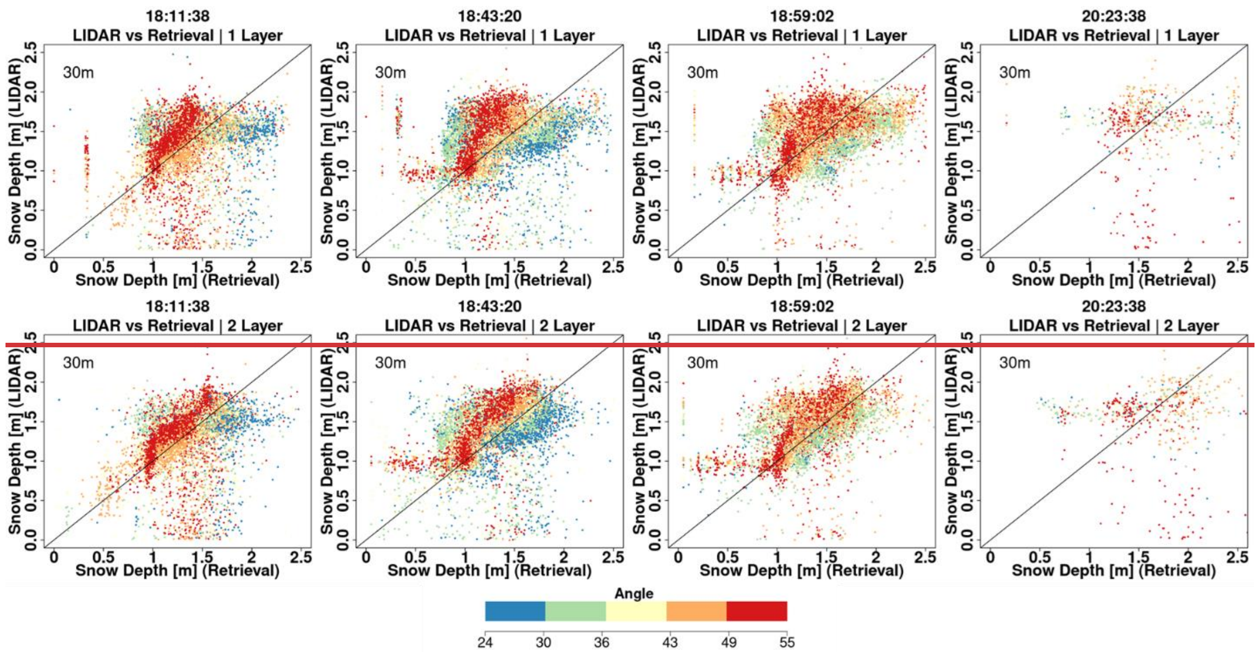

~~**Figure A1**: Same as Fig. 7b with pixels color coded according to the local SnowSAR incidence angle for all four flightlines and for single (top row) and two-layer (bottom row) retrievals at 30 m resolution.~~

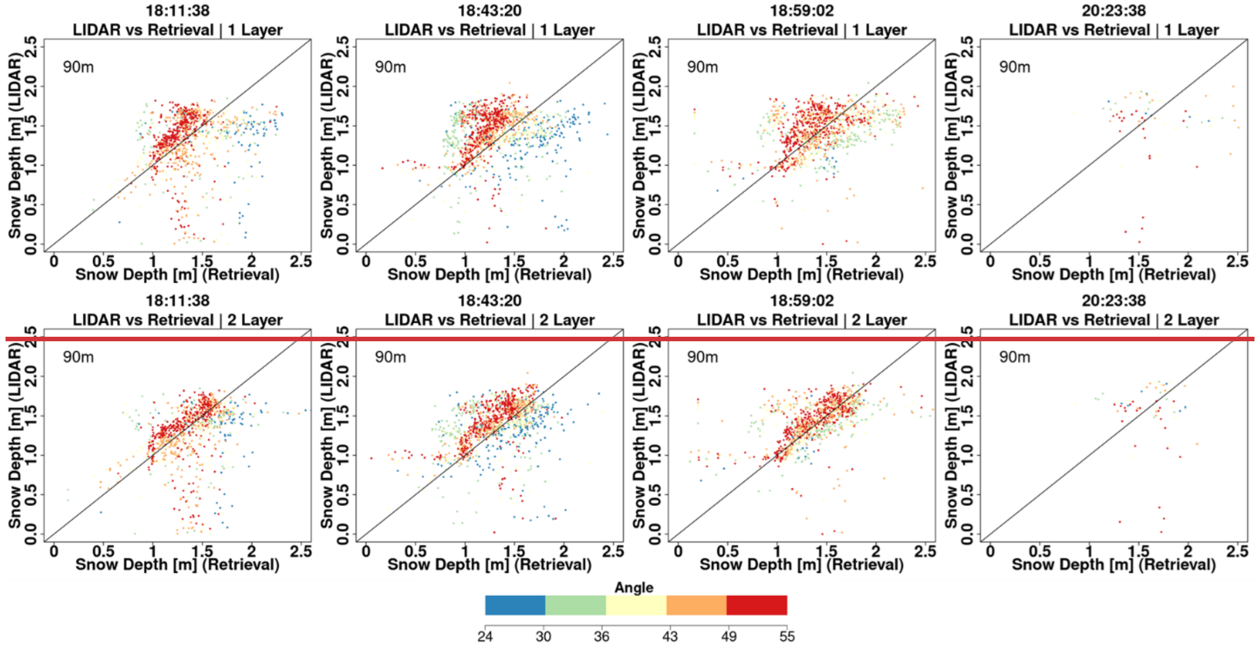

~~**Figure A2**: Same as Fig. 7b with pixels color coded according to the local SnowSAR incidence angle for all four flightlines and for single-(top row) and two-layer (bottom row) retrievals at 90 m resolution.~~

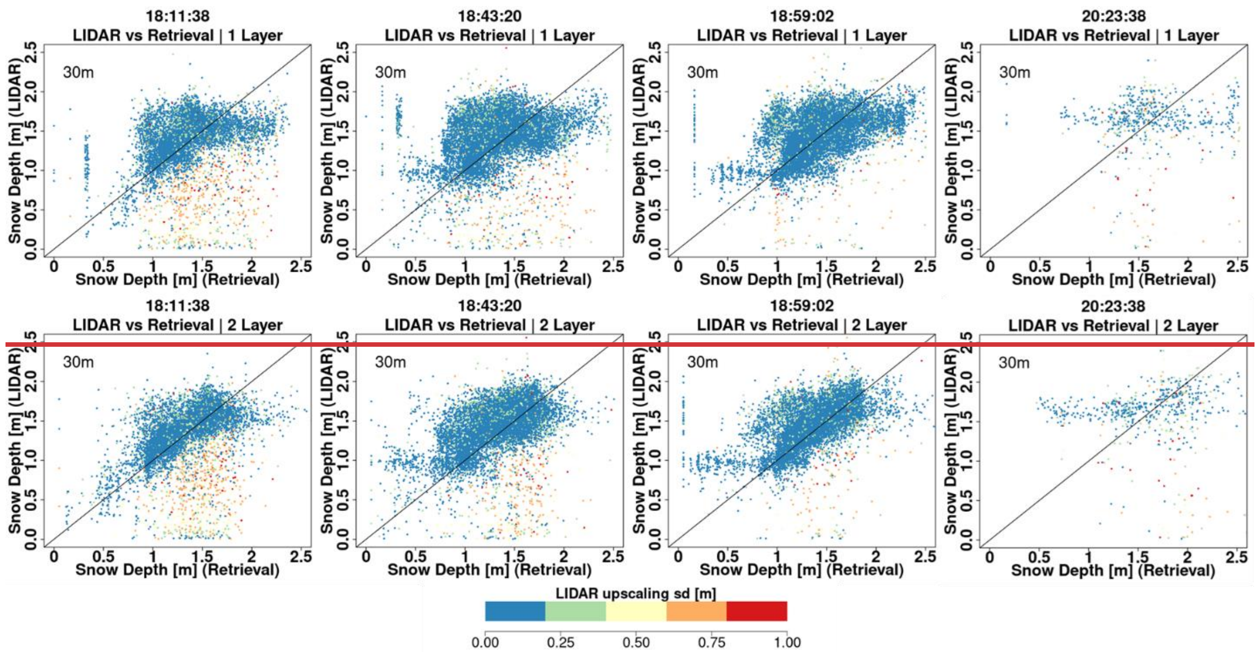

~~**Figure A3**: Comparison between LIDAR snow depth and successful retrievals for single and two-layer algorithms. The pixels are color coded according to the subgrid scale variability of the 30 m upscaled LIDAR pixel.~~

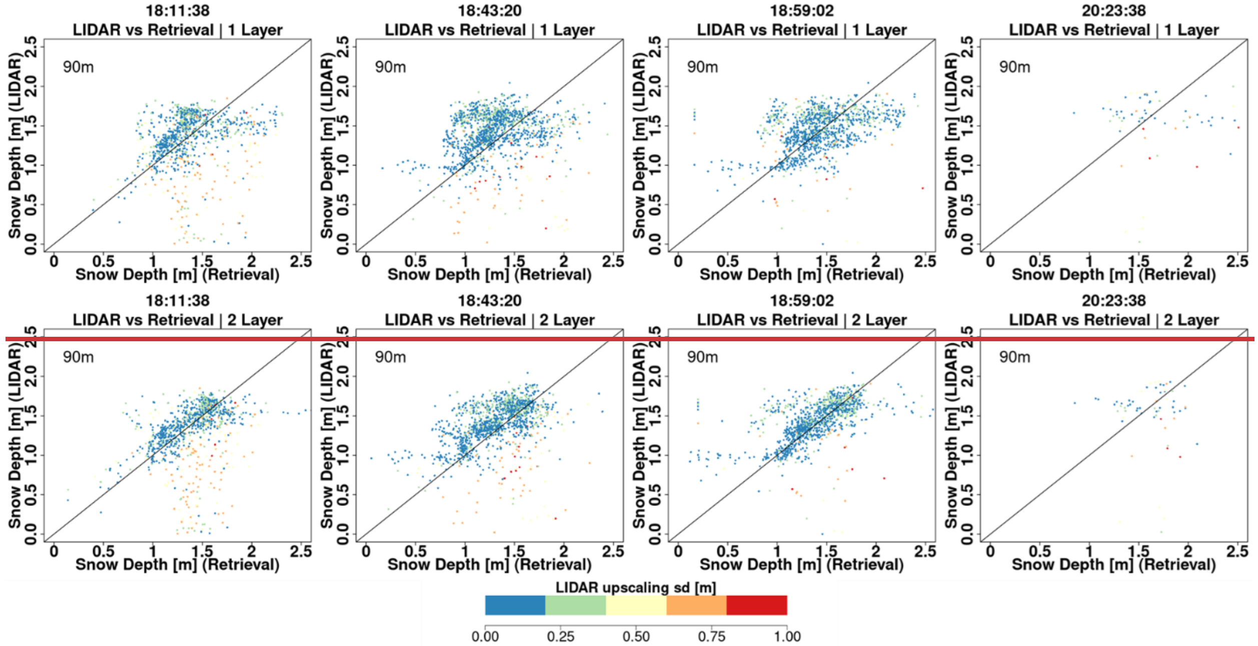

~~**Figure A4:** Comparison between SnowSAR snow depth and successful retrievals. The pixels are color coded according to the subgrid scale variability of the 90 m upscaled LIDAR pixel.~~

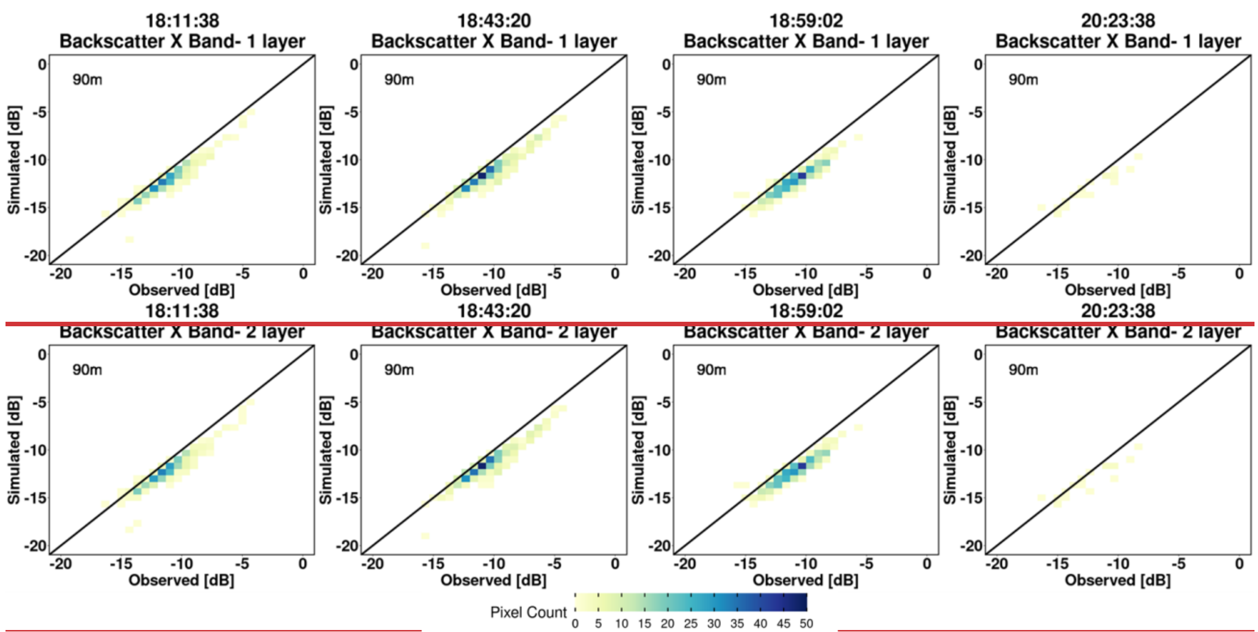

~~**Figure A5**: Comparison between SnowSAR backscatter (X-band) and BASE-AM converged backscatter at 90 m resolution for successful retrievals. Error statistics can be found in Table 4.~~

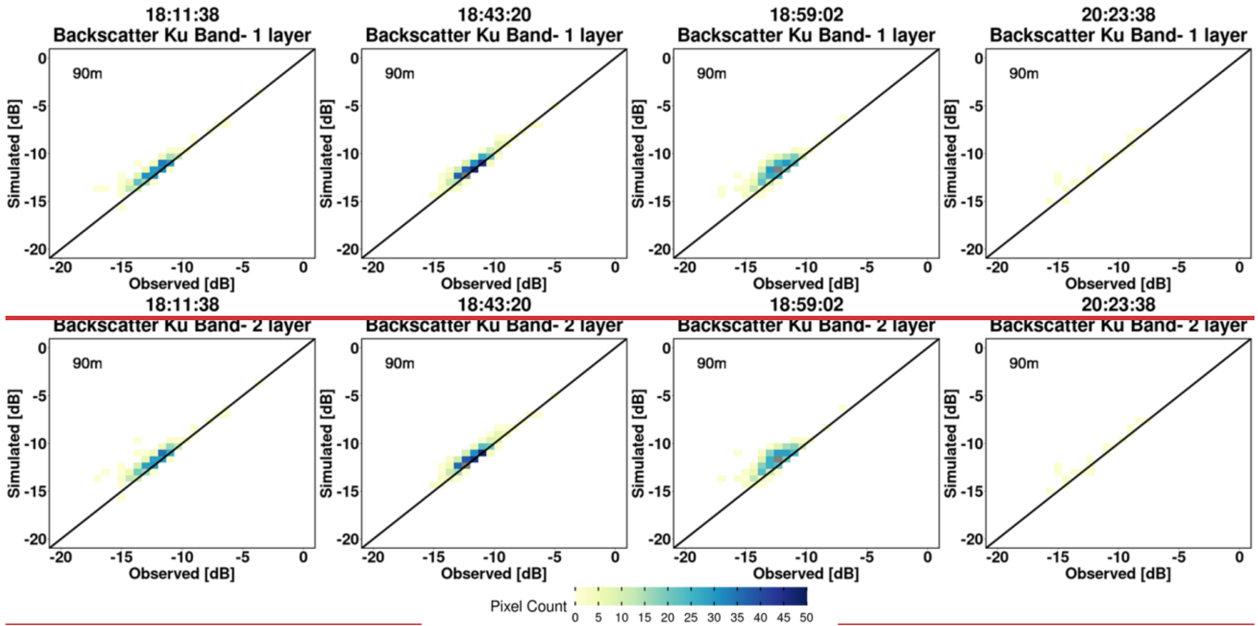

~~**Figure A6** - Comparison between SnowSAR backscatter (Ku-band) and Base-AM converged backscatter at 90 m resolution for successful retrievals. Error statistics can be found in Table 4.~~

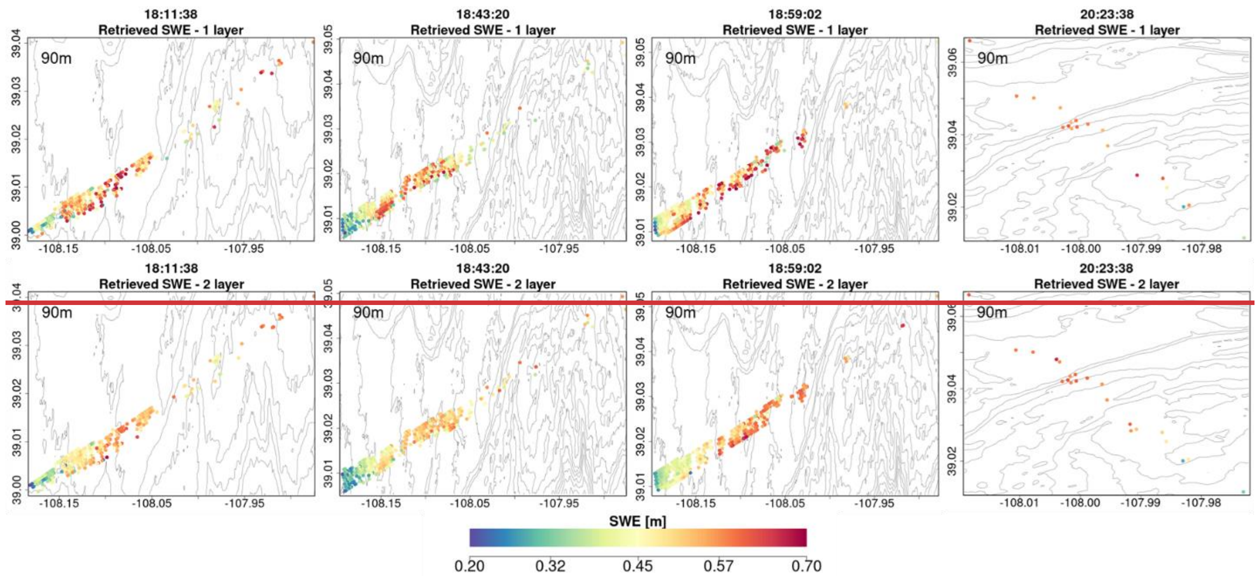

~~**Figure A7:** Spatial distribution of successful SWE retrievals for single- and 2-layer snowpacks at 90 m resolution. The retrievals are for grassland pixels only.~~

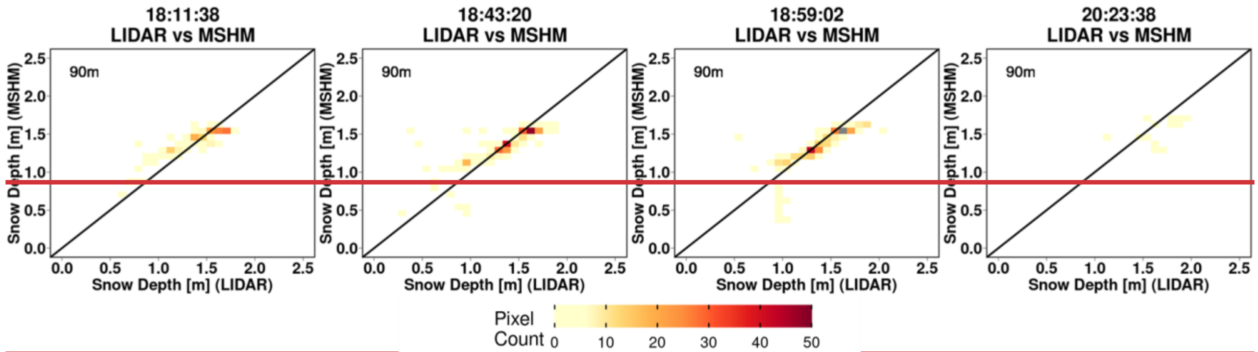

~~**Figure A8:** Heatmaps of LIDAR snow depth and snow depth predicted by MSHM at the time of SnowSAR flights for overlapping pixels at 90 m resolution.~~

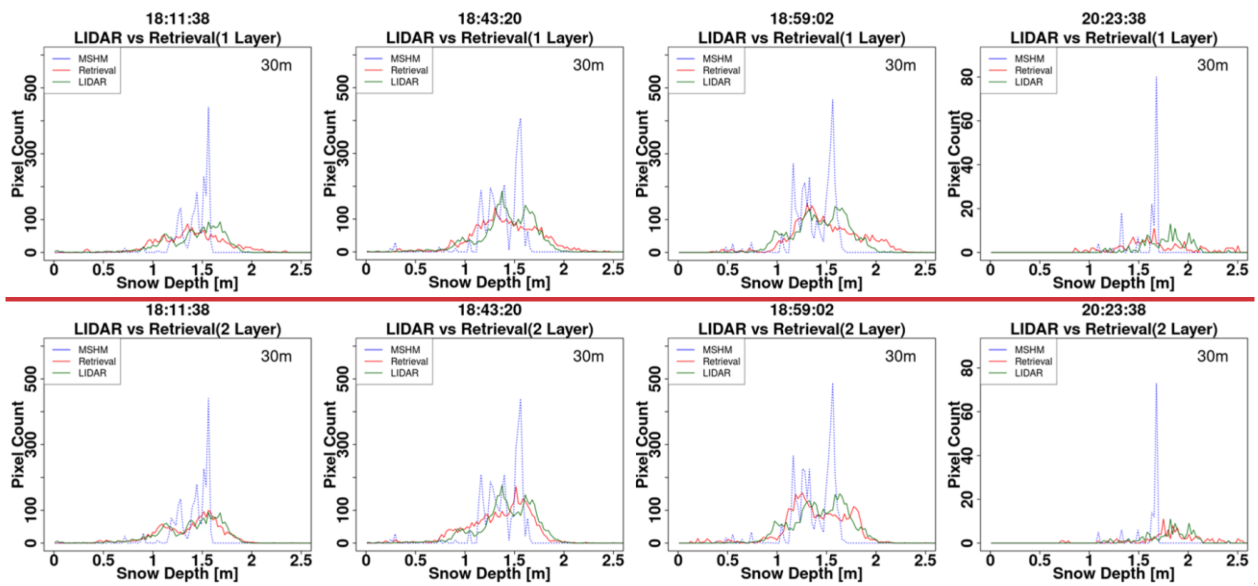

~~**Figure A9:** Histogram of snow depth (SD) from LIDAR, MSHM, and successful retrievals at 30 m using 1- and 2- layer snowpacks. The total number of pixels for each snow depth product is the same. Successful retrievals are for pixels with local incidence angles in the 30º–45º range and relative residual backscatter (RRB) of less than 30% for each of the four flights (see Table 4). LIDAR SD in pixels with subgrid scale variability corresponding to standard deviation of less than 0.3 m for the upscaled 90 m LIDAR pixel are not included.~~

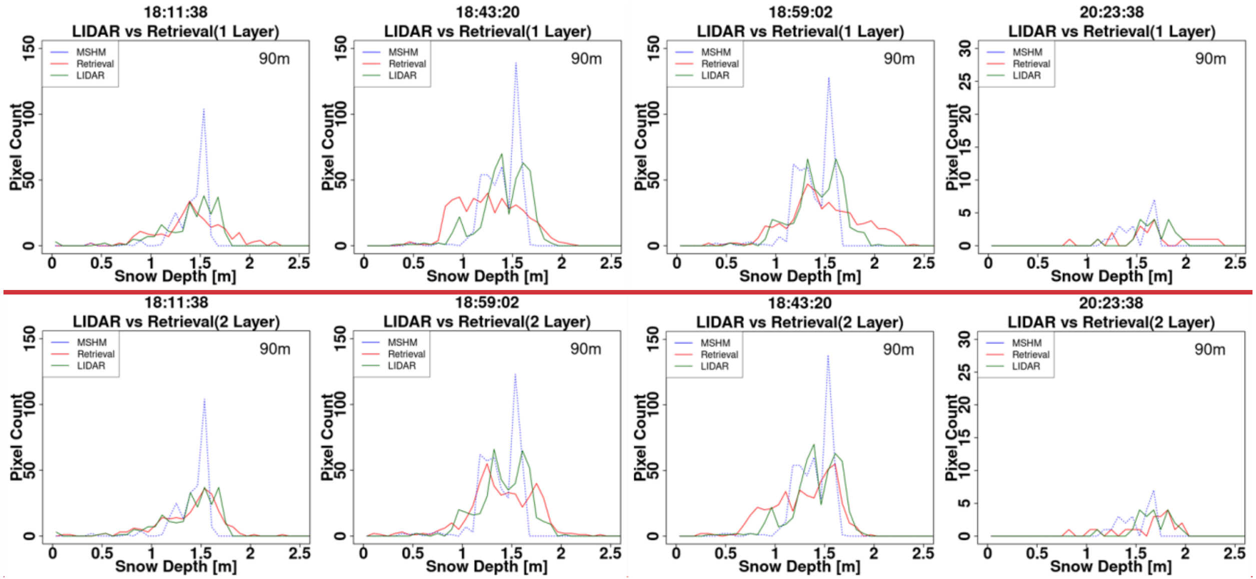

~~**Figure A10** - Histogram of snow depth (SD) from LIDAR, MSHM, and successful retrievals at 90 m using 1- and 2- layer snowpacks. The total number of pixels for each snow depth product is the same. Successful retrievals are for pixels with local incidence angles in the 30°–45° range and relative residual backscatter (RRB) of less than 30% for each of the four flights (see Table 4). LIDAR SD in pixels with subgrid scale variability corresponding to standard deviation of less than 0.3 m for the upscaled 90 m LIDAR pixel are not included.~~

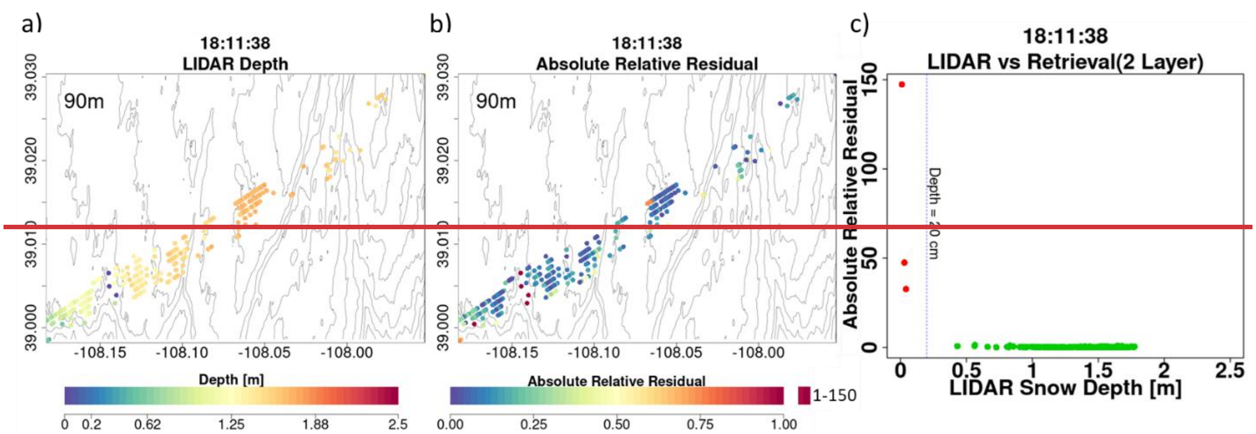

~~**Figure A11** – Analysis of unsuccessful retrievals for pixels with large mean snow depth residuals at 90 m resolution: a) Map of LIDAR snow depth highlighting in deep blue the locations where very shallow snow is attributed to measurement error. b) Note spatial agreement between shallow snow depth and very large residuals. c)There are only a few points at the edges of forests and shallow snow depths that are flagged not successful. The gray elevation contours are plotted every 50 m.~~

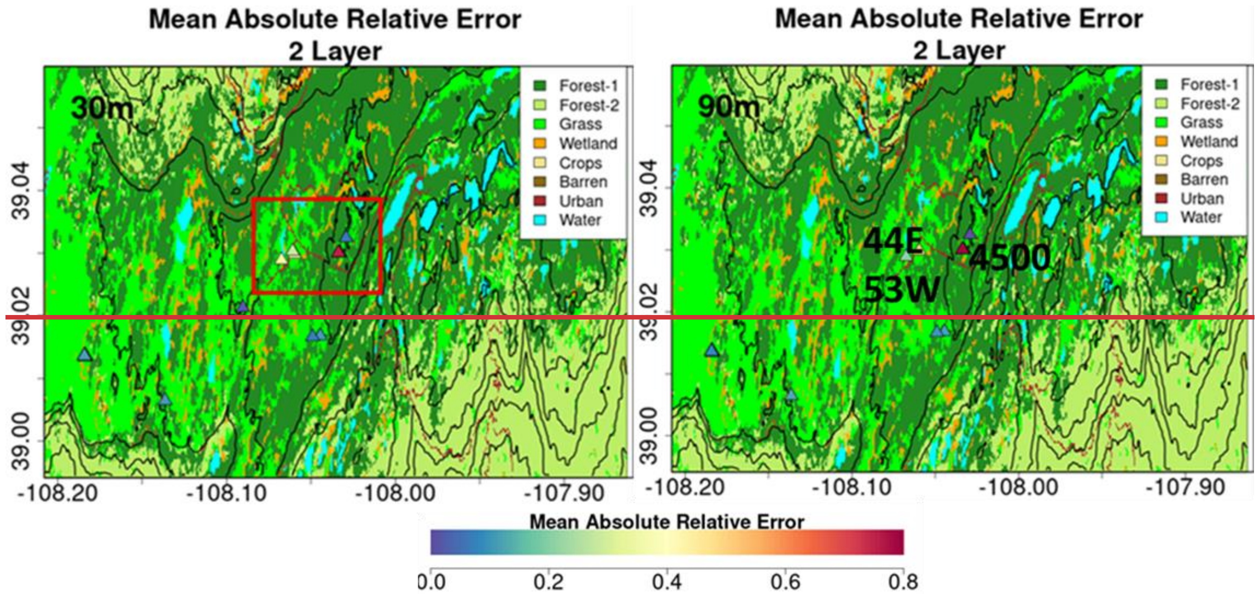

~~**Figure A12** Spatial context for snow pits with very large absolute relative errors (MARE) calculated as the mean of the relative difference between SWE retrievals within 100 m of the snow pit and the values at the snow pit. Locations with very large errors (orange to red) are inside the red box marked in top plot. Snowpit 4500 is a region of complex land cover including evergreen forest, a road and a pond. Snowpits 53W and 44E are close to each other on the same side of the road in expansive grassland.~~

~~8. Competing Interests~~

~~The contact author has declared that none of the authors has any competing interests~~

~~9. References~~

~~Bateni, S. M., Margulis, S. A., Podest, E., and McDonald, K. C.: Characterizing Snowpack and the Freeze–Thaw State of Underlying Soil via Assimilation of Multifrequency Passive/Active Microwave Data: A Case Study (NASA CLPX 2003), IEEE Trans. Geosci. Remote Sens., 53, 173–189, https://doi.org/10.1109/TGRS.2014.2320264, 2015.~~

~~Benjamin, S. G., Weygandt, S. S., Brown, J. M., Hu, M., Alexander, C. R., Smirnova, T. G., Olson, J. B., James, E. P., Dowell, D. C., Grell, G. A., Lin, H., Peckham, S. E., Smith, T. L., Moninger, W. R., Kenyon, J. S., and Manikin, G. S.: A North American Hourly Assimilation and Model Forecast Cycle: The Rapid Refresh, Mon. Weather Rev., 144, 1669–1694, https://doi.org/10.1175/MWR-D-15-0242.1, 2016.~~

~~Berliner, L. M.: Physical-statistical modeling in geophysics: Physical-Statistical Modeling in Geophysics, J. Geophys. Res. Atmospheres, 108, n/a-n/a, https://doi.org/10.1029/2002JD002865, 2003.~~

~~Bhattacharyya, A.: On a measure of divergence between two statistical populations defined by their probability distributions". https://doi.org/10.3390/rs12203422, 2020.~~

~~Cao, Y. and Barros, A.P.: Weather-Dependent Nonlinear Microwave Behavior of Seasonal High-Elevation Snowpacks, Remote Sens., 12, 3422, https://doi.org/10.3390/rs12203422, 2020.~~

~~Cao, Y. and Barros, A. P.: Topographic controls on active microwave behavior of mountain snowpacks, Remote Sens. Environ., 284, 113373, https://doi.org/10.1016/j.rse.2022.113373, 2023.~~

~~Cao, Y., and Barros, A.P.: Indirect Estimation of Boreal Vegetation Contributions to SAR Backscatter Measurements – Toward Operational Retrievals of Snow in Forest Areas. Rem. Sensing of the Environ., in review, 2023. ESS Open Archive, August 14, 2023, https://doi:10.22541/au.169200040.06589257/v1, 2023.~~

~~Deems, J. S., Painter, T. H., and Finnegan, D. C.: Lidar measurement of snow depth: a review, J. Glaciol., 59, 467–479, https://doi.org/10.3189/2013JoG12J154, 2013.~~

~~Dobson, M., Ulaby, F., Hallikainen, M., and El-rayes, M.: Microwave Dielectric Behavior of Wet Soil-Part II: Dielectric Mixing Models, IEEE Trans. Geosci. Remote Sens., GE-23, 35–46, https://doi.org/10.1109/TGRS.1985.289498, 1985.~~

~~Dobson, M., Ulaby, F., Hallikainen, M., and El-rayes, M.: Microwave Dielectric Behavior of Wet Soil-Part II: Dielectric Mixing Models, IEEE Trans. Geosci. Remote Sens., GE-23, 35–46, https://doi.org/10.1109/TGRS.1985.289498, 1985.~~

~~Hallikainen, M., Ulaby, F., Dobson, M., El-rayes, M., and Wu, L.: Microwave Dielectric Behavior of Wet Soil-Part 1: Empirical Models and Experimental Observations, IEEE Trans. Geosci. Remote Sens., GE-23, 25–34, https://doi.org/10.1109/TGRS.1985.289497, 1985.~~

~~Huang, X. and Swain, D. L.: Climate change is increasing the risk of a California megaflood, Sci. Adv., 8, eabq0995, https://doi.org/10.1126/sciadv.abq0995, 2022.~~

~~Kang, D. H. and Barros, A. P.: Observing System Simulation of Snow Microwave Emissions Over Data Sparse Regions — Part I: Single Layer Physics, IEEE Trans. Geosci. Remote Sens., 50, 1785–1805, https://doi.org/10.1109/TGRS.2011.2169073, 2012a.~~

~~Kang, D. H. and Barros, A. P.: Observing System Simulation of Snow Microwave Emissions Over Data Sparse Regions – Part II: Multilayer Physics, IEEE Trans. Geosci. Remote Sens., 50, 1806–1820, https://doi.org/10.1109/TGRS.2011.2169074, 2012b.~~

~~Kim, E., Gatebe, C., Hall, D., Newlin, J., Misakonis, A., Elder, K., Marshall, H. P., Hiemstra, C., Brucker, L., De Marco, E., Crawford, C., Kang, D. H., and Entin, J.: NASA's snowex campaign: Observing seasonal snow in a forested environment, in: 2017 IEEE International Geoscience and Remote Sensing Symposium (IGARSS), 2017 IEEE International Geoscience and Remote Sensing Symposium (IGARSS), Fort Worth, TX, 1388–1390, https://doi.org/10.1109/IGARSS.2017.8127222, 2017.~~

~~Kim, R. S., Durand, M., Li, D., Baldo, E., Margulis, S. A., Dumont, M., and Morin, S.: Estimating alpine snow depth by combining multifrequency passive radiance observations with ensemble snowpack modeling, Remote Sens. Environ., 226, 1–15, https://doi.org/10.1016/j.rse.2019.03.016, 2019.~~

~~Kuhnert, P. M. (2017). Physical-statistical modeling. In Wiley StatsRef: Statistics Reference Online, pages 1–5. Wiley.~~

~~Li, D., Durand, M., and Margulis, S. A.: Estimating snow water equivalent in a Sierra Nevada watershed via spaceborne radiance data assimilation, Water Resour. Res., 53, 647–671, https://doi.org/10.1002/2016WR018878, 2017.~~

~~Manickam, S. and Barros, A.: Parsing Synthetic Aperture Radar Measurements of Snow in Complex Terrain: Scaling Behaviour and Sensitivity to Snow Wetness and Landcover, Remote Sens., 12, 483, https://doi.org/10.3390/rs12030483, 2020.~~

~~Martinec, J., Seidel, K., Burkart, U., and Baumann, R.: Areal modelling of snow water equivalent based on remote sensing techniques., XX General Assembly IUGG in Vienna, 1991.~~

~~Mendoza, P. A., Musselman, K. N., Revuelto, J., Deems, J. S., López-Moreno, J. I., and McPhee, J.: Interannual and Seasonal Variability of Snow Depth Scaling Behavior in a Subalpine Catchment, Water Resour. Res., 56, https://doi.org/10.1029/2020WR027343, 2020.~~

~~Metropolis, N., Rosenbluth, A.W., Rosenbluth, M,.N., Teller, A., and Teller, E.: Equation of State Calculations by Fast Computing Machines. The Journal of Chemical Physics, 21, 1087–1092, https://doi.org/10.1063/1.1699114, 1953.~~

~~Mote, T. L., Grundstein, A. J., Leathers, D. J., and Robinson, D. A.: A comparison of modeled, remotely sensed, and measured snow water equivalent in the northern Great Plains: COMPARISON OF SNOW WATER EQUIVALENT, Water Resour. Res., 39, https://doi.org/10.1029/2002WR001782, 2003.~~

~~Musselman, K. N., Addor, N., Vano, J. A., and Molotch, N. P.: Winter melt trends portend widespread declines in snow water resources, Nat. Clim. Change, 11, 418–424, https://doi.org/10.1038/s41558-021-01014-9, 2021.~~

~~National Academies of Sciences, Engineering, and Medicine: Thriving on Our Changing Planet: A Decadal Strategy for Earth Observation from Space. Washington, DC: The National Academies Press. https://doi.org/10.17226/24938, 2018.~~

~~Painter, Thomas H., Berisford, Daniel F., Boardman, Joseph W., Bormann, Kathryn J., Deems, Jeffrey S., Gehrke, Frank, Joyce, Michael, Laidlaw, Ross, Mattmann, Chris, McGurk, Bruce, Ramirez, Paul, Richardson, Megan, and Skiles, S. McKenzie: ASO L4 Lidar Snow Depth 3m UTM Grid, Version 1, https://doi.org/10.5067/KIE9QNVG7HP0, 2018.~~

~~Pan, J., Durand, M. T., Vander Jagt, B. J., and Liu, D.: Application of a Markov Chain Monte Carlo algorithm for snow water equivalent retrieval from passive microwave measurements, Remote Sens. Environ., 192, 150–165, https://doi.org/10.1016/j.rse.2017.02.006, 2017.~~

~~Pan, J., Durand, M., Lemmetyinen, J., Liu, D., & Shi, J.: Snow water equivalent retrieved from X-and dual Ku-band scatterometer measurements at Sodankylä using the Markov Chain Monte Carlo method, The Cryosphere Discussions, 2023, 1-26.~~

~~Proksch, M., Mätzler, C., Wiesmann, A., Lemmetyinen, J., Schwank, M., Löwe, H., and Schneebeli, M.: MEMLS3&a: Microwave Emission Model of Layered Snowpacks adapted to include backscattering, Geosci. Model Dev., 8, 2611–2626, https://doi.org/10.5194/gmd-8-2611-2015, 2015.~~

~~Rott, H., Cline, D. W., Duguay, C., Essery, R., Etchevers, P., Hajnsek, I., Kern, M., Macelloni, G., Malnes, E., Pulliainen, J., and Yueh, S. H.: CoReH2O, a dual frequency radar mission for snow and ice observations, in: 2012 IEEE International Geoscience and Remote Sensing Symposium, IGARSS 2012 - 2012 IEEE International Geoscience and Remote Sensing Symposium, Munich, Germany, 5550–5553, https://doi.org/10.1109/IGARSS.2012.6352348, 2012.~~

~~Sturm, M., Taras, B., Liston, G. E., Derksen, C., Jonas, T., and Lea, J.: Estimating Snow Water Equivalent Using Snow Depth Data and Climate Classes, J. Hydrometeorol., 11, 1380–1394, https://doi.org/10.1175/2010JHM1202.1, 2010.~~

~~Tsang, L., Durand, M., Derksen, C., Barros, A. P., Kang, D.-H., Lievens, H., Marshall, H.-P., Zhu, J., Johnson, J., King, J., Lemmetyinen, J., Sandells, M., Rutter, N., Siqueira, P., Nolin, A., Osmanoglu, B., Vuyovich, C., Kim, E., Taylor, D., Merkouriadi, I., Brucker, L., Navari, M., Dumont, M., Kelly, R., Kim, R. S., Liao, T.-H., Borah, F., and Xu, X.: Review article: Global monitoring of snow water equivalent using high-frequency radar remote sensing, The Cryosphere, 16, 3531–3573, https://doi.org/10.5194/tc-16-3531-2022, 2022.~~

~~Villano, M., Ustalli, N., Dell'Amore, L., Jeon, S.-Y., Krieger, G., Moreira, A., Peixoto, M. N., and Krecke, J.: NewSpace SAR: Disruptive Concepts for Cost-Effective Earth Observation Missions, in: 2020 IEEE Radar Conference (RadarConf20), 2020 IEEE Radar Conference (RadarConf20), Florence, Italy, 1–5, https://doi.org/10.1109/RadarConf2043947.2020.9266694, 2020.~~

~~Wiesmann, A. and Mätzler, C.: Microwave Emission Model of Layered Snowpacks, Remote Sens. Environ., 70, 307–316, https://doi.org/10.1016/S0034-4257(99)00046-2, 1999.~~